UNIVERSITY OF CALIFORNIA
RIVERSIDE

Enhancement of Membrane Filtration Processes via Nanomaterial Coatings for the Generation of Electrostatic Forces, Oil Barriers, and Joule Heating

A Dissertation submitted in partial satisfaction
of the requirements for the degree of

Doctor of Philosophy

in

Chemical and Environmental Engineering

by

Alexander Vladimirovich Dudchenko

December 2016

Dissertation Committee:
Dr. David Jassby, Chairperson
Dr. Sharon Walker
Dr. Jinyong Liu

The Dissertation of Alexander Vladimirovich Dudchenko is approved:

_____

_____

_____

Committee Chairperson

University of California, Riverside

ACKNOWLEDGMENTS

I would like to thank my adviser Dr. David Jassby for his mentorship and guidance, which grew me as an individual and a professional. His sage advice, patience, and passion for research have left a great imprint on my life and will continue to have lasting influence in the future. I would like to thank Dr. Sharon Walker for her guidance during the times of my successes and counsel during times of hardship. Furthermore, I would like to thank Dr. Kurt Schwabe and Dr. Jinyong Liu for their council on my projects.

I would like to especially thank Dr. Nichola Kinsinger who has mentored me throughout my time as an undergraduate and a doctorate student. Her council, mentorship, and advice have taught me how to approach research problems, develop the right questions, and inspired me to pursue work in water treatment field. I would also like to thank the undergraduate students that helped me do a lot of the hands-on work, specifically Julianne Rolf, Kyle Russell, Lucy Shi, Liana Olivas, Alexis Cardenas, Chuxiao Chen, Ryan Ward, and Hira Yoshihara-Saint.

I would like to thank IGERT: Water SENSE - Water Social, Engineering, and Natural Sciences Engagement program (Award Abstract # 1144635), ACS Petroleum Research Fund (54649-DNI9), and the Office of Naval Research (N00014-14-1-0809) for funding my work.

The research results discussed in this dissertation, in part or in full are reprints of three journal articles. The first article is reprinted from Journal of Membrane Science, volume 468, by A.V. Dudchenko, J. Rolf, K. Russle, W. Duan, and D. Jassby, “Organic Fouling Inhibition on Electrically Conducting Carbon Nanotube – Polyvinyl Alcohol

Composite Ultrafiltration Membranes", pages 1-10, Copyright © 2014, with permission from Elsevier B.V. The second article is reprinted with permission from ACS Nano, volume 9, issue 10, entitled "Coupling Underwater Superoleophobic Membranes with Magnetic Pickering Emulsions for Fouling-Free Separation of Crude Oil/Water Mixtures: An Experimental and Theoretical Study", by A.V. Dudchenko, J. Rolf, L. Shi, L. Olivas, W. Duan, and D.Jassby Copyright © 2014 American Chemical Society. The third article is under current review in Nature Nanotechnology, entitled "Frequency Dependent Stability of CNT Joule Heaters in Ionizable Environments: Implications for Desalination", by A.V. Dudchenko, C. Chen, A. Cardenas, J. Rolf, and D. Jassby, upon acceptance all rights will belong to the appropriate publisher. In these publications, co-authors Julianne Rolf, Kyle Russell, Lucy Shi, Liana Olivas, Alexis Cardenas, Chuxiao Chen, and Wenyan Duan assisted in preparation, and characterization of materials used to complete the experimental work. The co-author Dr. David Jassby directed and supervised the research in these publications, which have greatly improved their quality and depth.

DEDICATIONS

This dissertation is dedicated to my mother and my fiancé, as well as the rest of my family who supported me since childhood, and without whom I could not have pursued my dreams.

ABSTRACT OF THE DISSERTATION

Enhancement of Membrane Filtration Processes via Nanomaterial Coatings for the Generation of Electrostatic Forces, Oil Barriers, and Joule Heating

by

Alexander Vladimirovich Dudchenko

Doctor of Philosophy, Graduate Program in Chemical and Environmental Engineering
University of California, Riverside, December 2016
Dr. David Jassby, Chairperson

Water scarcity exasperated by global climate change and growing population is a growing challenge for many regions of the world. The water shortages are prompting regions to look for new water sources to supplement their dwindling water supplies ranging from wastewater reuse to saline ground water desalination. Membrane filtration is one of the few technologies that can treat these water sources but suffers from fouling, and complicated system designs. Herein we present methods to address problems faced by membrane filtration through use of nanomaterial-based thin films that actively address key problems faced by membrane filtration processes.

Organic contaminants commonly found in surface water, ground water, and wastewater rapidly foul membranes, leading to decline in their performance. We demonstrate that application of electrical potentials to electrically conductive and robust carbon nanotube (CNT) thin films deposited on UF membranes allows for generation of

strong electrostatic repulsive forces. We demonstrate that these artificially generated electrostatic forces can reduces membrane fouling during treatment of synthetic wastewaters and model organic foulants, with the results being qualitatively explained by the solution of modified Poisson-Boltzmann equation. Although our results demonstrate electrostatics forces are effective at preventing organic fouling, their efficacy suffers in saline waters such as produced, flow back, and industrial waste waters. These waters can contain oil emulsions made up of small and stable oil droplets that can rapidly foul membranes. We take advantage of the nano-magnetite properties, which cause the nano-particles to form a film at the water-oil interphase. The nano-magnetite films create a physical barrier that prevents oil droplets from interacting with the membrane surface or coalesce during filtration. The fouling prevention is explored as a function of nano-particle and membrane hydrophilicity with a developed theoretical framework qualitatively explaining our experimental results. Finally, we demonstrate that the previously prepared CNT films when deposited on hydrophobic membranes can be used to drive membrane distillation (MD) process via Joule heating effect. We explore the stability of the CNT films using electrical impedance spectroscopy (EIS) under different frequencies and salinities and demonstrate that they can be used to achieve exceptionally high single pass recoveries in MD.

Table of Contents

Table of Figures

Table of Tables

Chapter 1 Introduction

1.1 Water Scarcity

Water scarcity exacerbated by population growth, climate change, and pollution is one of the largest global challenges impacting coastal and inland regions of the world. The increase in global population is leading to increased demand for food requiring large quantities of irrigating waters. The increased water demand is in turn straining local water resources which require construction of complex and expensive water distributions systems such as the water projects in California.[1] Unfortunately, current distribution systems are designed around the water storage capacity of snow packs in the mountain ranges. The snow packs form during fall and winter, capturing precipitation and storing it until spring and summer. The increased temperatures in spring and summer lead to snow pack melting which provides a steady supply of fresh water to local regions such as California where this water is distributed throughout the state via the water projects. However, global warming is increasing temperatures leading to later snow fall in the year and reduced snowpack sizes, but also to earlier melting and runoff in the spring.[2,3] These impacts result in lower quantity of water being stored in the snowpack, with later snow formation leading to larger amount of runoff in the fall, which at the moment cannot be effectively captured without large infrastructure changes. Furthermore, the earlier start of the runoff leads to additional water losses, as the runoff is not captured leading to lower water availability during the summer month caused by earlier depletion of snowpacks. Finally, the water scarcity issues are complicated by fact that large number of waters are contaminated with nutrients (which lead to algal blooms), chemicals, and pharmaceuticals all of which are difficult to treat, especially using current water treatment technologies. These unfortunate

consequences are forcing water suppliers to look for better water treatment methods so they can access water source that have not being previously used such as seawater, saline ground water, and wastewater.

Membrane filtration has been looked as the ultimate solution to water shortages, with seawater desalination via Reverse Osmosis (RO) being looked to as a never-ending freshwater supply. Membrane filtration is one of the few processes that can potentially treat waters with high salinity while removing pollutants ranging from bacteria to dissolved solids, allowing for access to previously unused water sources. However, membrane filtration process is not a trivial or low cost solution as compared to traditional water source, such as clean ground water or pristine surface waters (i.e. lakes and rivers). Membrane processes for water treatment face many challenges, including moderate to high energetic costs due thermodynamic limit of the separation process, which are exacerbated by membrane fouling caused by buildup of contaminants on the membrane surface, and finally by complicated system designs. Regardless of these shortcomings membrane filtration has become a de-facto standard for sea water desalination, and is looking to become a standard installation in wastewater treatment plants, and potable reuse processes.

1.1.1 A Brief History of Membrane Filtration

The history of membrane filtration is a long road of painstaking research that started in early 1900s and took over 70 years to reach a point of commercialization. The first carefully documented pressure driven filtration process was not reported until 1907 by Bechold.[4] Bechold prepared a membrane with graded porosity made of a filter paper impregnated with acetic acid colloid. This was one of the first ultrafiltration (UF)

membranes reported, a classification Bechold is given credit for creating. The membrane field until end of 1930s used celluloid, collodion, cellophane and rayon to synthesis membranes, which limited the control of membrane porosity, pore size and permeability, leading to overall field stagnation that prevented its commercialization.

The membrane field did not advance until the development of modern polymer science in 1937 with synthesis of a synthetic polyamide by Carothers. [5] The creation of new polymers allowed for development of the first modern RO membranes in 1950s with synthesis of dense polymeric membranes. These membranes were prepared out of cellulose acetate and could achieve high salt rejections (<98%), but unfortunately had very poor permeability which prevented their commercialization. [6] The development of asymmetric or Loeb-Sourirajan membranes in 1962 addressed the issue of low permeability in filtration membranes.[7,8] The Loeb-Sourirajan membrane had a unique asymmetric structure even though the membrane was casted from the same starting material but was composed of two distinct regions, the dense selective skin which dictated the rejection properties of the membrane, and a highly porous support structure, which did not hinder the permeation of water. These membranes demonstrated a significant improvement in permeability, while maintaining same rejection properties as the dense membranes. Furthermore, through control of solvent conditions it was possible to have a good control over membrane pore size allowing for synthesis of membranes with rejection properties ranging from reverse osmosis to ultrafiltration. The development of these membranes was the turning point for membrane filtration processes, with two major chemical companies, DuPont and Dow

Chemical, starting the development of large-scale membrane systems for seawater desalination and beginning a promise of never ending fresh water.

1.2 Fundamentals of Membrane Filtration

Membrane filtration is a flexible physical separation process that utilizes a semi-permeable membrane that only allow constituents of choice to pass (e.g. water), while preventing everything else from passing (e.g. dissolved solids, bacteria, or organics). However, the mechanisms of separation are not simple and the membrane performance while can be well quantified in an idealized test environment can rapidly change with environmental conditions, where the interactions of membrane chemistry, operational mode, and solution composition define final membrane performance. In the following sections the fundamentals of membrane separation mechanics, synthesis and operational modes are discussed. The forces in membrane filtration and fouling mechanisms are complicated topics warranting an in-depth discussion in section 1.3 and 1.4.

1.2.1 Membrane Rejection Mechanisms

The membrane rejection properties (i.e. the ability to remove certain contaminants) are dependent on the membranes primary mechanism of separation and can be either *sieving*, *diffusion* or a mixture of the two. The *sieving* mechanism relies on physical size exclusion of contaminants from water, where the contaminant is physically too large to pass through the pores of the membrane. The second mechanism is *diffusion* and relies on the difference in diffusion rates of constituents through the membrane, where one of the constitutes (e.g. water) can readily diffuse through the membrane but the contaminant

being rejected (e.g. salt ions) diffuse at a slower rate, leading to their separation. These rejection mechanisms are readily tuned by either changing pore size of the *sieving* membranes, or the chemical composition of the membranes that utilize the *diffusion* mechanism. This has led to formation of four classes of water treatment membranes, which are based on their ability to remove contaminants of certain size from water. Microfiltration (MF) can remove contaminants larger than 100 nm, ultrafiltration (UF) can remove contaminants in size range from 10 nm to 100 nm, nanofiltration (NF) can remove contaminants from 10 nm to 1.5 nm, and reverse osmosis (RO) can remove contaminants down to 0.1 nm in size (Fig.1.1). Furthermore, two new processes have been developed and added to the overall water membrane filtration family, specifically forward osmosis (FO) and membrane distillation (MD). FO is a recently developed technology that has similar separation characteristics as RO (diffusion separation mechanism with similar salt rejection properties). MD is an emerging technology that utilizers a hydrophobic MF membrane, which allows for water vapor (and any constitutes that can vaporize) to pass through the membrane, but prevents any liquid water (and anything dissolved in it) from passing through the membrane achieving similar and in most cases better dissolved solid rejection then RO.

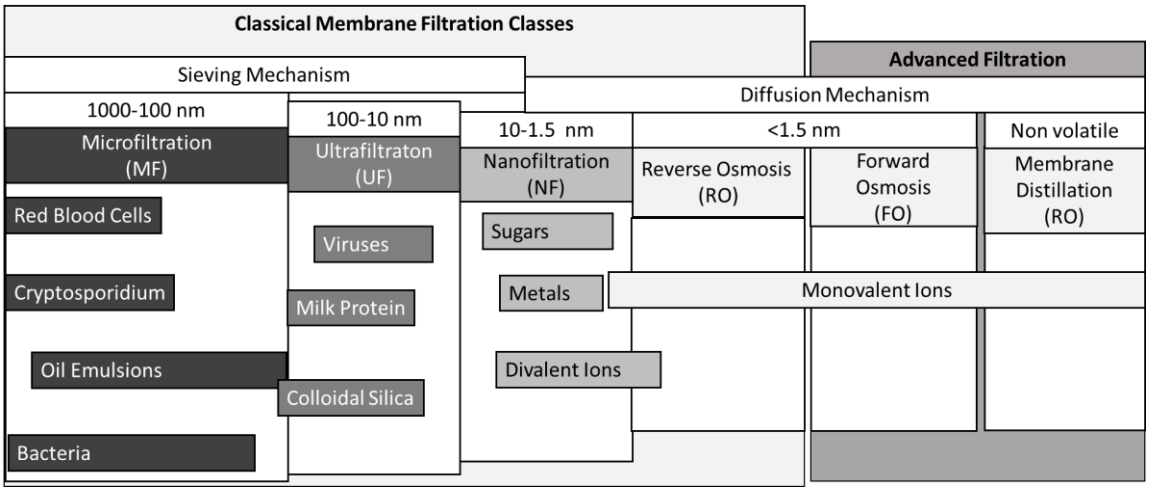

Figure 1.1: Classification of membranes based on size and type of separation mechanism, including classical and newly developed filtration processes. The list under the processes show examples of contaminates that can be removed.

1.2.2 Synthesis and Morphology of Filtration Membranes

The synthesis of the filtration membranes is probably one of the crucial aspects that defines their performance, including permeability, rejection, and fouling resistance. The goal of a successful membrane synthesis is to attain control over structural morphology, membrane pore size, and material chemistry. The structural morphology is the crucial aspect that makes modern membranes effective at water treatment, where the distinct asymmetrical structure allows these membranes to achieve high permeability. The importance of pore size control cannot be understated, as it dictates the kind of contaminants the membrane can remove, and defines the minimum expected permeability. Finally, the chemical composition of the membrane defines its surface chemistry, stability, and chemical resistance. Bellow we will briefly discuss some of the most common membrane synthesis methods.

1.2.2.1 Phase Inversion or the Loeb-Sourirajan Synthesis

The Loeb-Sourirajan membranes or more commonly known as asymmetric membranes were developed in 1962 using cellulose acetate, and form the basis for synthesis of the asymmetric membrane structures today. [8] In original Loeb-Sourirajan work a trial and error method (still used today) was used, where cellulose acetate polymers with different acetylation and polymer chain length were used to cast membranes. The polymers were dissolved in acetone making a viscous solution, which was then casted on a glass plate with a doctor blade (Fig. 1.2A). The film was then dried for short period and then immersed in ice water that contained magnesium perchlorate which acted as a pore swelling agent. The immersion of the film in water resulted in diffusion and mixing of acetone (a cellulose acetate solvent) with water (where cellulose acetate is not soluble) leading to critical concentration build up and precipitation of cellulose acetate (Fig. 1.2B). The nonhomogeneous mixing of acetone and water lead to formation of cellulose acetate rich areas (which precipitate) and cellulose acetate poor areas (which form pores). The diffusion-limited mixing of water and acetone resulted in formation of distinct concertation gradients of cellulose acetate and water across the thickness of the polymer film. The concertation gradient lead to formation of large pores at the top of the polymer film (the surface directly in contact with the water solution), with pore size decreasing with polymer depth where the polymer in contact with the glass formed a dense film, that could contain very small pores or none at all. The final polymer film was removed from the glass and either dried in air or soaked in water to remove excess solvent and ensure complete precipitation. This process typically referred to as a phase inversion synthesis can be

extended to any polymer that can be dissolved in a solvent and be brought in contact with a non-solvent and where the solvent and non-solvent solutions are miscible.

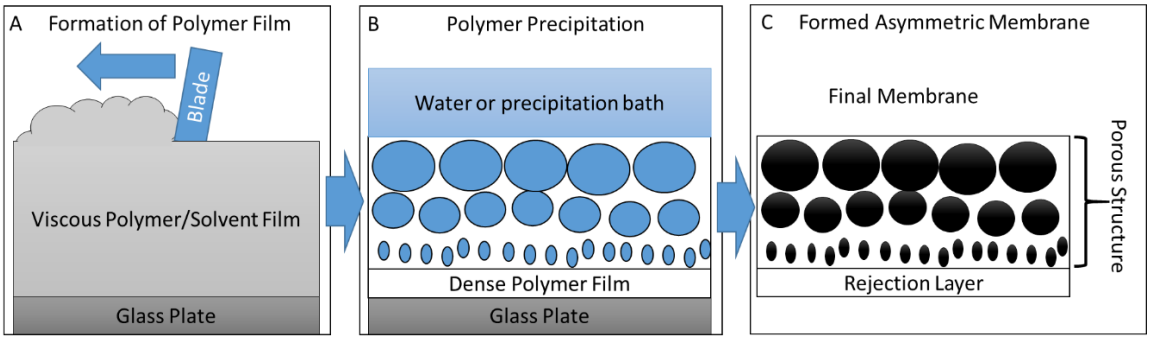

Figure 1.2: Synthesis of asymmetric polymeric membranes: (A) A uniform film is formed on glass plate surface by doctor blade method, where the doctor blade is dragged over the film removing excess polymer solution. (B) The film is immersed in precipitation bath forming porous membrane structure, where white is the polymer rich phase and the blue is water rich phase. (C) The membrane is removed from the glass plate and washed/dried forming the final asymmetric membrane.

Today the most common membranes prepared with the phase inversion method are polysulfone (PS), polyethersulfone (PES) and polyacrylonitrile (PAN) membranes. Furthermore, to improve control of pore sizes, structural integrity, and chemical composition of the membranes additives such as polyvinyl pyrrolidone (PVP) or polyethylene glycol (PEG) are added into the polymer solution before casting. The addition of these polymers can significantly improve structural stability and hydrophilicity of the final membranes even at low loadings (1-5 wt%). [9]

1.2.2.2 Interfacial Polymerization, the King of RO

The interfacial polymerization is probably one of the most crucial membrane synthesis techniques in membrane filtration today, as this synthesis alone is responsible for the growth of RO and seawater desalination. Although Loeb was able to synthesis reverse osmosis capable membranes using cellulose acetate and the phase inversion approach,

these membranes had low permeability. Furthermore, the cellulose acetate used for these membranes is bio degradable, which meant that bacteria would literally consume the membranes during desalination, which adversely affected their performance. [10] Although other polymers were used to prepare RO membranes via the phase inversion method, they were unable to achieve high permeability and salt rejection making it clear that a new approach was required to prepare commercial RO membranes.

The answer to high permeability and salt rejection came in a form of interfacial polymerization synthesis, which was developed independently by Cadotte and Riley at the same time. [11,12] The interfacial polymerization is similar to the phase inversion process, with key difference being that the precipitation solution and polymer solution are immiscible, with polymer precipitation occurring at the solution interphase due to monomer/polymer crosslinking. The most common synthesis of RO membranes grows a thin polyamide film on top of a support membrane (such as PS asymmetric membrane described above). The synthesis starts with soaking of support membrane with an aqueous solution containing m-phenylenediamine (MPD). The soaked support is immersed into a hexane solution that contains trimesoyl chloride (TMC) (Fig. 1.3A). The TMC and MPD are highly reactive and start to form a polyamide thin film at the interphase between the hexane and water layer, making the RO rejection layer (Fig. 1.3B.) The prepared polyamide thin film membranes (TFC) have shown excellent salt rejection and permeability qualities, making them the gold standard in RO, and NF processes.

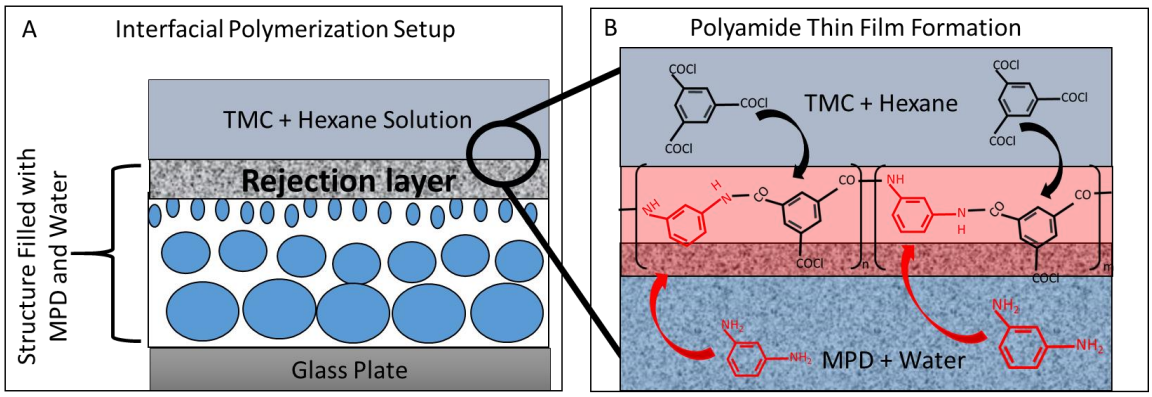

Figure 1.3: Interfacial polymerization of polyamide thin films A) Showing the bulk configuration, with an asymmetrical membrane filled with water + TMC solution, and a TMC + Hexane solution on top of the membrane rejection layer. B) The close up look of interfacial polymerization where TMC (shown in red) and MPD (shown in black) diffuse to the Hexane/Water interface and react, forming the polyamide thin film structure (shown in the red tinted area).

1.2.2.3 Stretching, the Application of Brute Force to Membrane Synthesis

Stretching is a commonly used methods to make filtration membranes, although it is not as elegant as that of Loeb-Sourirajan or the interfacial polymerization method, this method does not require the use of solvents. Furthermore, this method made it possible to prepare membranes out of polypropelyne (PP) and polytetrafluoroethylene (PTFE) which cannot be readily dissolved in solvents (PTFE is insoluble, while PP requires highly elevated temperature and harsh solvents (decalin and xylen at temperatures above 80-100˚C)), making most synthesis discussed above impractical.

The stretching technique was developed in 1970s by Celgard for production of polyethalene (PE) and PP membranes for energy storage applications, but quickly found its way into water treatment field. [13] The stretching process is simple, but requires proper understanding of polymer structure to form membranes with uniform porosity. The stretching synthesis typically starts by extrusion of a polymer film out of desired polymer

material. The film is then stretched in one direction in a cold state to nucleate (initiate pore formation) the pores, after which the polymer is heated up and stretched again in perpendicular direction to the first (cold) stretching direction, forming the final pore structure (Fig. 1.4). [14,15] The formation of pore structure is reliant on the polymers ability to form crystalline regions (i.e. where polymer chains have an ordered structure), which provide the structural strength to keeps the polymers chains together (e.g. similar to a knot), while the amorphous regions stretch forming the porous structure. Extended studies on the impact of polymer molecular weight, stretching, and temperature impacts on membrane structure and porosity have been performed using PP, polyvinylidene fluoride (PVDF), and PTFE. [14–20] In general increased polymer weights leads to improved uniformity and interconnectivity of the membrane pore structure, which has been largely attributed to improved distribution of crystalline regions. The improvement in crystalline region formation is further controlled by proper annealing (e.g. the polymers have to be heated and cooled at controlled rates in order to induce polymer crystallization) of the materials especially in the case of PP. [16] Stretching has been a very useful method of membrane synthesis, and is widely used in industry today to prepare membranes for application ranging from gas purification, to water separation.

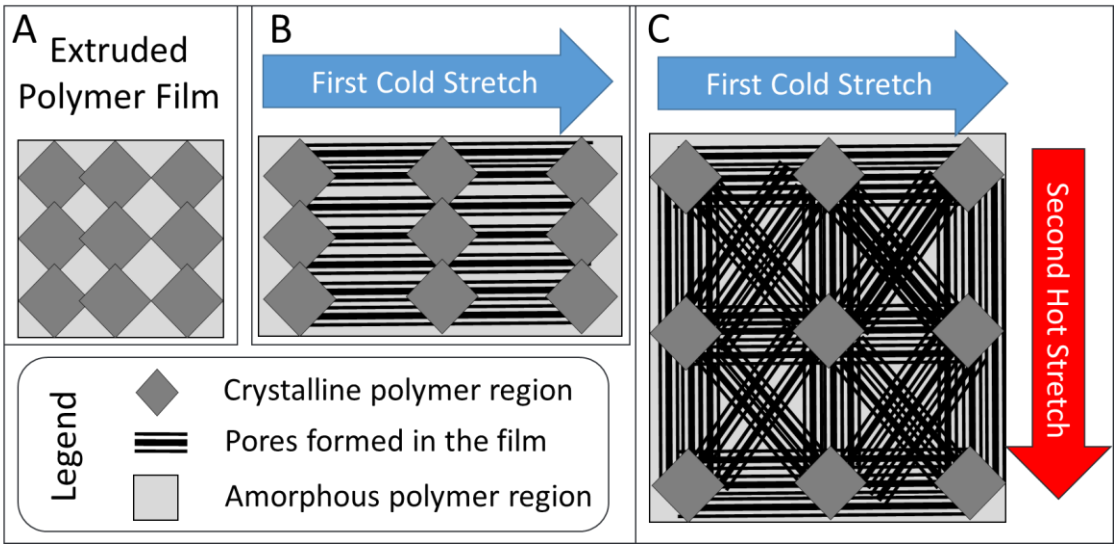

Figure 1.4: Formation of porous films using stretching. (A) A hypothetical polymer film with uniform distribution of crystalline regions (shown as diamonds) and amorphous regions (shown as gray space). (B) First cold stretch (blue arrow) is applied where pores (black lines) are nucleated. (C) Second hot stretch (red arrow) (applied perpendicular to first cold stretch) is used to form final porous structure with formation of additional pores.

1.2.2.4 Track Etching

Track etching is a commonly used technique to produce membranes with precise pore structure and density, which are important parameters for biological, or medical applications, but leads to overall high membrane cost. The strength of track etching is its precise control over pore size formation which ranges from nanometers to microns in size, and pore density which can range from a few to 10^{10} pores/m^2. The process is accomplished by irradiating a polymer film with energetic heavy ions, which are bombarded at the membrane material forming pores (Fig. 1.5 A). The control of pore size is dependent on the ion source used, if single-ion scheme is used, then precise control of pore size can be achieved through proper adjustment of aperture, where porosity is controlled by detecting ion penetration, disabling the ion source, and moving the membrane sample to the next

pore position effectively printing the pores one by one. The single ion scheme allows for precise pore structure and density control but can be very slow. Broad ion irradiation can be used to speed up the process, where the ion beam is scattered and bombards the whole membrane sample with pore size and density being controlled by irradiation time and temperature.[21,22] The track etching process is sensitive to the polymers being used, where polycarbonate (PC) and polyethylene naphthalate (PET) are the materials of choice, as they are not resistant to strong oxidizers, while material like PVDF (resistance to strong oxidizers) are rarely used due to long etching times.[22–26]

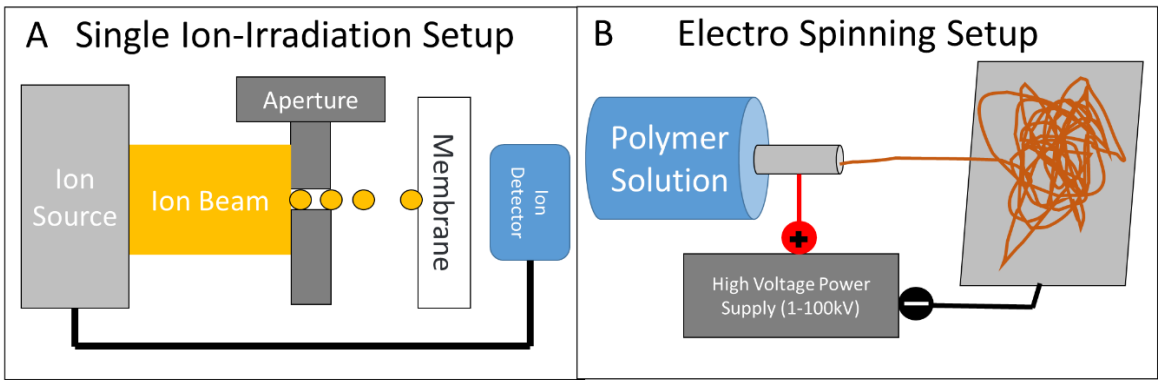

Figure 1.5: Ion-irradiation and electrospinning setup diagrams. (A) The single ion-irradiation setup used to make controlled single pores in a membrane, here an ion source generates an ion beam, where an aperture is used to reduce this beam down to individual ions, which then bombard the membrane forming the pore, once the ions fully penetrate the membrane they are detected by the ion detector and the ion source is switched off. (B) A typical electrospinning configuration, where a high potential is applied between a metal needle that's injecting polymer solution and grounded collector surface, on which the fiber mat is formed.

1.2.2.5 Electrospinning

Electrospinning is a modern technique that can be used to produce highly porous membranes.[9,27,28] The electrospinning process is simple in theory with most common configuration using a metal injection needle to deliver polymer solution to a collector

surface, where the needle is attached to a high voltage power source, and the collector is grounded (Fig. 1.5B). Application of high electrical potential between the needle and collector forms a strong electrical field, which forces the flow of the charged polymer solution out of the injection needle and onto the collector forming a polymeric fiber matt. The control of the polymeric fiber morphology (thickness, porosity, and structural integrity) is accomplished through control of the applied electrical field, injection rate of the polymer solution, solution viscosity, chamber temperature, and humidity. [29] The precise control over the fiber morphology has attracted allot of interest in applying these membranes for water filtration applications, ranging from microfiltration to membrane distillation. [28,30–34] Unfortunately, these membranes are in fact non-woven type matts, where the fiber packing density controls the pore structure of the membrane, making it difficult for synthesis of tight ultrafiltration membranes. However, these fibrous mats have been found to be ideal for use as support membranes during interfacial polymerization for preparation of TFC membranes (e.g. RO,NF and FO). [35]

1.2.3 The Driving Force in Membrane Filtration, and Operational Modes

The laws of thermodynamics govern all processes that have been developed today, including membrane filtration. The separation of contaminants and water requires a driving force that would drive the permeation of water through the membrane, while leaving behind a concentrated waste. Classical membrane filtration has utilized a pressure gradient across the membrane (i.e. trans membrane pressure) to force water permeation through it, leading to development of dead-end and cross flow filtration operation. Recent introduction of advanced water treatment processes (FO and MD) has introduced osmotic pressure and

thermal driving forces that lead to separation of water and contaminants, while introducing a new operational mode where dual crossflow channel operation is typically used.

The membrane filtration process has multiple resistances to water flow. The first and most obvious resistance is the hydrodynamic resistance to water flow through the membrane, which is due to the presence of a torturous and constricted water path through the membrane pore structure. The membrane porosity, pore size, and structure define the minimum pure water membrane permeability which dictates how much water can flow through the membrane at certain applied transmembrane pressure. The next important resistance is the osmotic pressure difference between the feed and the permeate. The osmotic pressure arises due to the presence of ions, organic molecules and/or colloids in the feed water, and in general increases exponentially with their concentration. The osmotic pressure will only impact the membrane process if the ion/molecules are being rejected by the membrane and generate a difference in osmotic pressure between the feed and permeate streams. The osmotic pressure difference then drives water flow from the permeate to the feed channel, thus to force water flow from the feed to the draw a greater pressure then the osmotic pressure difference must be applied. The osmotic pressure difference generally impacts RO and NF processes the most as they generate large salt concertation difference between the feed and the draw. The UF or MF process can be affected by osmotic pressure as well when treating high concentrations of organic molecules or colloids which can generate osmotic pressure. The osmotic pressure difference is further exacerbated by formation of concentration polarization layer which arises due to rejection of contaminants, and their limited diffusion back to the feed, in effect

increasing their concentration at the membrane surface which further increases the osmotic pressure difference. Finally, any buildup of organic and inorganic contaminants on the membrane surface creates additional hydrodynamic resistance to water flow, requiring higher operating pressures. These resistances have driven development of different operational modes aimed at reducing the overall resistance to water flow.

The first and simplest operational mode is the *dead-end* operation typically seen in MF processes, here the water or *feed* to be treated is forced through the membrane, leaving any contaminants as a cake layer on the membrane surface, while allowing the treated water or *permeate*, to permeate through the membrane entering the permeate channel (Fig 1.6A). The dead-end operation is trivial to implement in theory, but leads to significant bottle neck in operation as the buildup of contaminants on membrane surface leads to rapid decline in performance, requiring either membrane replacement or cleaning step. Thus, dead-end operation is typically used in very clean streams, with very loose membranes (MF), or where the contaminants are a desired product (e.g. food products, medicine, etc). Furthermore, dead end filtration is strongly impacted by osmotic pressure difference and formation of concentration polarization layer which further reduces its efficiency.

The second operational mode typically used in UF, NF and RO is the *cross-flow* operation. Herein, the feed is pumped across the membrane surface through the feed channel which is generally pressurized and forces water permeation through the membrane generating the permeate and leaving any rejected contaminants in the feed channel which concentrate (Fig. 1.6B). The concentrated feed is referred to as a *retentate* (as it retains any of the contaminants and untreated feed) and flows out of the feed channel to be further

treated or disposed of. The clear advantage of cross-flow operation is ability to achieve a steady state operation as contaminants do not accumulate on the membrane surface (i.e. where no cleaning or interruptions in the process will occur allowing for continuous water treatment), unlike dead-end filtration where eventually the process must be shut down due to accumulation of contaminants. Furthermore, through use of high cross-flow velocities it is possible to induce mixing of the concentration polarization layer and reduce its impact on the process.

The third operational mode is result of recent development of the FO and MD processes. Unlike the previous two mode of operation, these processes utilize two channels with cross-flow configuration. The first channel is used for the feed as done in a standard cross-flow filtration, except it is not pressurized. The second cross-flow channel is used for a *draw* solution, which carries the permeate away from the membrane and is not pressurized. The driving forces in these processes are also different from classical membrane filtration. Forward osmosis utilizes osmotic pressure gradient between the feed (low osmotic pressure) and draw (high osmotic pressure), due to the membrane being water permeable (typically a TFC polyamide membrane with RO rejection properties is used) water can diffuse through the membrane permeating from low osmotic pressure to high osmotic pressure region (i.e. from dilute solution to concentrated solution) entering the draw channel and diluting it. The dilution of the draw reduces its osmotic pressure and thus it is crucial to quickly replace the diluted draw with a concentrated draw, which is accomplished with a cross-flow. The advantage of FO is a simple process setup as no high pressure pumps are required, and the use of a proper draw solution allows for treatment of

feed with high salt content that RO is unable treat. The MD process requires a draw for similar reasons, although there it is to maintain a constant temperature gradient across the membrane and remove water vapor from the draw channel, with the details of this process discussed in section 1.8.

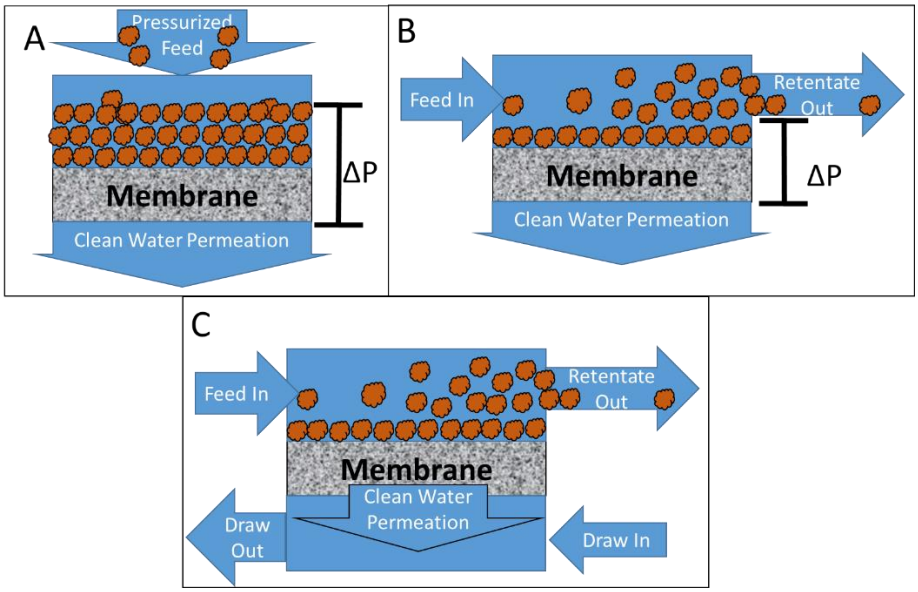

Figure 1.6: Operational modes of membrane filtration. (A) Dead end operation. (B) Cross-Flow Operation. (C) Counter-crossflow operation (typically used for FO and MD systems). The brown shaped objects represent contaminants.

1.3 Forces in Membrane Filtration, from Drag to DLVO and Beyond

The particulates, organics, and inorganic materials that are present in feed water experiences larger number of forces during filtration, and these forces dictate if the membrane will foul and at what rate. The most common forces that these fouling agent's experiences are fluid drag, electrostatic, van der Wall, and hydrophobic/hydrophilic forces.

1.3.1 Fluid Drag Forces

The fluid drag forces arise from the fluid flow in the membrane module, for the simplification of discussion we only going to consider here a cross-flow filtration unit. The basic fluid dynamics dictate that any material in a moving fluid will experience a drag force due to the material hydrodynamic radius and surface friction, where magnitude of the drag is directly proportional to the particulate or macromolecule size. The fluid drag force is ultimately a vector force, and can be split into the fluid force acting along the membrane surface, and fluid drag force acting toward the membrane surface (Fig. 1.7A). The force that is acting toward the membrane surface is responsible for membrane fouling as it controls the foulant trajectory in the channel and how the foulants will interact with the membrane surface. The particulate that is near the membrane surface is further impacted by shearing force that is generated due to non-linear velocity gradient of water at the membrane surface, which attempts to shear off and lift the particle in to the bulk flow counteracting the drag force. These forces have been derived as early as 1965 by Saffman and improved by many others throughout the years developing simple relationships for the calculation of the drag and lift forces in filtration process. [36–40] The shear force is typically very weak unless a very high cross-flow velocity is used and thus the interaction force between the membrane and a foulant are dominated by drag forces, electrostatic forces, van der Wall forces, and hydrophobic/hydrophilic interactions.

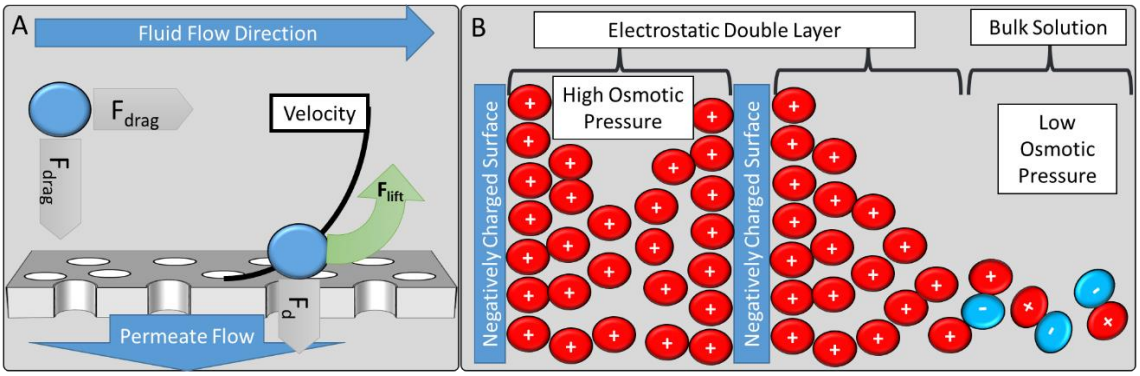

Figure 1.7: A) The fluid forces acting on particle in the filtration process, where F_{drag} is the fluid drag force, F_{lift} is the shearing lift force. B) The electrostatic double layer build up on charged surfaces, where their interaction leads to elevated ion concentration and high osmotic pressure compared to the bulk solution, which leads to repulsion.

1.3.2 The Classical DLVO

The interaction force theory that describes interaction between a colloid and a surface has been developed by Derjaguin, Landau, Verwey, and Overbeek (DLVO) in early 1940s, and has become the cornerstone for predicting particulate and organic attachment in transport processes, ranging from particulate transport in sand columns, to fouling in membrane filtration systems.[41–49] The basis of the DLVO lies in combining the electrostatic and van der Wall forces. The electrostatics in water arise from the charged functional groups (e.g. carboxylic groups which dissociate giving it a negative charge), which most organics, colloids and surfaces have. The negative charge leads to ion build up on the surface which attempts to neutralize the surface charge (following the electro-neutrality principle) resulting in local increase in ion concentration (referred to as the electrostatic double layer (EDL)) as well as leading to an electrical potential drop, which has classically been modeled with Poisson-Boltzmann equation.

The Poisson-Boltzmann (PB) equation attempts to predict the electrical potential distribution near a surface by assuming that ions behave as point chargers, which accumulate near the charged surface in an exponential manner, until the sum of all point chargers (ions) neutralizes the surface charge. The PB equation has been shown to be an adequate approximation for surfaces with low surface charges. However, it fails completely once the surface charge approaches 200 mV where the point charge approximation begins to predict that ions will occupy the same space, which is physically impossible. The size effect has been accounted for with various version of modified Poisson-Boltzmann (MPB) equation which accounts for the steric size of ions. [50–54] The solution of PB or MPB equation allows for prediction of ion concentration distribution near the charged surface which is required for calculation of the electrostatic repulsion force.

The electrostatic repulsion occurs if two similar charged surface start to approach each other, when the two surfaces are far apart and EDL layers are not interacting there is no repulsive force. However, when the two surfaces approach each other and their EDL layers interact it results in a local elevated salt concertation and osmotic pressure (Fig. 1.7B). The increase in osmotic pressure results in a force that tries to push the two surfaces apart (e.g. high osmotic pressure leads to a driving force that pushes water molecules between the surfaces leading to their repulsion). Thus, the electrostatic force is strongly affected by the ionic strength (i.e. salt concentration) of the solution, where high ion concentrations reduces the overall osmotic pressure difference leading to a reduced repulsive force. One of the most common forces that counters the electrostatic repulsive force is the van der Waals attraction force.

The J.D. van der Waals in 1873 postulated that there are residual attractive and repulsive forces that lead to interaction between atoms and molecules. The van der Waals forces arise from quantum interactions, and are typically due to presence of a permanent dipole (i.e. Keesom force), forces between a permeant dipole and an induced dipole (i.e. Debye force), and force between instantaneously induced dipoles (i.e. London dispersion force). The van der Waals forces are short length interaction forces, but are very strong at nanometer separation distances and dictate if adhesion would occur. One of the most commonly used equation for predicting van der Waals force of attraction between particles has been derived by Hamaker and is commonly used in DLVO calculations.[55] This additional force is the second force in classical DLVO theory, however it does not account for the hydration or hydrophobic forces that are unique to aqueous solution.

1.3.3 The Hydration and Hydrophobic Forces

The DLVO theory has been successful at describing interactions at long separation distances, but it fails to account for near surface interactions where separation is less then several nanometers. Furthermore, the classical DLVO theory does not account for effect of hydrophilicity and hydrophobicity, which have been shown to be important factors in membrane fouling.

The salvation (or hydration force) and hydrophobic force arise due to the surface chemistry and its interaction with the solution on molecular level. The hydration force is the most controversial force of the two, as currently no explicit mechanism has been agreed on. The basic concept of salvation force emerged when forces between neutral lipid bilayer membranes were observed, with DLVO being unable to explain these forces. [56–59] The

hydration force is assumed to occur due to formation of ordered molecular layers at a material surface made of water molecules, which must be pushed out of the way when the two surfaces come in contact. The physical mechanism however is still being disputed; some have suggested that it is due to anomalous polarization of water near the interface, leading to formation of a water layer. [60–62] However, other authors have suggested that the repulsion is due to thermally excited molecular groups that protrude from the surface, leading to steric repulsion [63,64] The hydration force however is an important part of foulant adhesion to surfaces, especially in systems where electrostatics and van der Waals forces are negligible.

The hydrophobic force is probably one of the most commonly considered forces in membrane filtration, as most membrane surfaces are quite hydrophobic which has prompted allot of work aimed at increasing their hydrophilicity. The hydrophobic force arises due to hydrophobic surfaces not having polar or ionic groups, which prevents the surface from hydrogen bonding with water. Water always tries to form hydrogen bonds in order to minimize its energetic state, however the water layer near a hydrophobic surface is unable to form hydrogen bonds with the surface. The inability of water to form hydrogen bond leads to local high free energy state of water, compared to the bulk. Thus, when two hydrophobic surfaces start to come close together the increased free energy state of water in the gap promotes the water to flow out into the bulk in order to minimize its energetic state, leading to an attractive force that "pulls" the two surfaces together. The presence of hydrophobic force has been experimentally measured with long interactions extending up to 10 nm. [65–67] Currently there is no complete theory for hydrophobic forces, but several

have been created based on overlapping solvation zones, or coalescence of vacuum gaps. [68,69]

1.3.4 The Steric Forces

Steric forces are different in nature from all the forces described previously as they arise from a physical (mechanical) interaction between molecules. Surfaces in water can be coated with molecular chains which will either be strongly adsorbed to the surface, or attempt to move away from the surface and freely "dangle" in the media, minimizing their entropy. When two surfaces coated with such dangling molecular chains start to approach each other and the chains begin to interact their movement becomes confined and increases their entropy. The increase in entropy then will lead to a consequent repulsive force as the chain will try to push the two surfaces apart. The magnitude of the repulsive forces depend on a surface coating density, type of molecular chains, and solvent interaction with the surface and polymer chains.[70] The complex relationships between these variables has made it challenging to develop comprehensive theory, although several theories for surfaces with low and high coverage of molecular chains have been considered. [70–74]

1.4 Fouling in Membrane Filtration

Fouling is one of the crucial problems that membrane filtration faces today, and has been studied since the inception of the modern membrane filtration process in 1960s. Membrane fouling is in effect an issue that cannot be solved with a single approach and requires multi-faceted solutions, where membrane chemistry, operational conditions, and feed water modifications are required to achieve good performance. However, even after

development of large number of membrane materials, modifications, and process optimizations the operation in real water conditions (e.g. industrial applications) will result in inevitable membrane fouling requiring membrane cleaning and eventual replacement. Thus, ultimately the goal of all fouling control methods is to slow down fouling rates, reduce the frequency of cleaning cycles, and increase membrane lifespan. However, before these methods are presented it is of utter importance to understand the basics of membrane fouling, which is indisputably a complicated process, however large number of careful studies have been performed extracting the primary mechanisms of membrane fouling which will be briefly covered bellow.

1.4.1 Pore Blocking and Constriction

Pore blocking and constriction are the first fouling events and the most frequent fouling modes that affect porous membranes (e.g. UF and MF). [75–77] *Pore Blocking* occurs when a fouling agent such as colloid, bacteria, or organic molecule will physically deposit on membrane surface leading to complete or partial pore closure (Fig. 1.7A). However, *pore constriction* occurs due to adsorption of fouling agent to the pore wall, leading to pore diameter reduction, where the adsorption is driven by either or combination of electrostatic, van der Waal, chemical (e.g. chemical bonding) or physical interactions (Fig. 1.7A). The pore blocking and pore constriction fouling events primarily occur on membranes that are treating fouling agents with similar size scale as the membranes pore structure. Thus, pore blocking and constriction can be prevented by utilizing membranes with pores that are much smaller than the fouling agents leading to overall lower fouling rates, although this can lead to enhanced cake layer formation and gel layer formation discussed below. It

should be further noted, that all membranes have a pseudo-porous structure, even dense TFC membranes such as RO have nano-sized pores (<1.5 nm in diameter) which can experience pore blocking with small organic molecules (as shown by poor rejection of NDMA and other non-charged organics). However, these impacts have been typically ignored as most studied organics have much larger size then the pores in RO or NF membranes. [78–80]

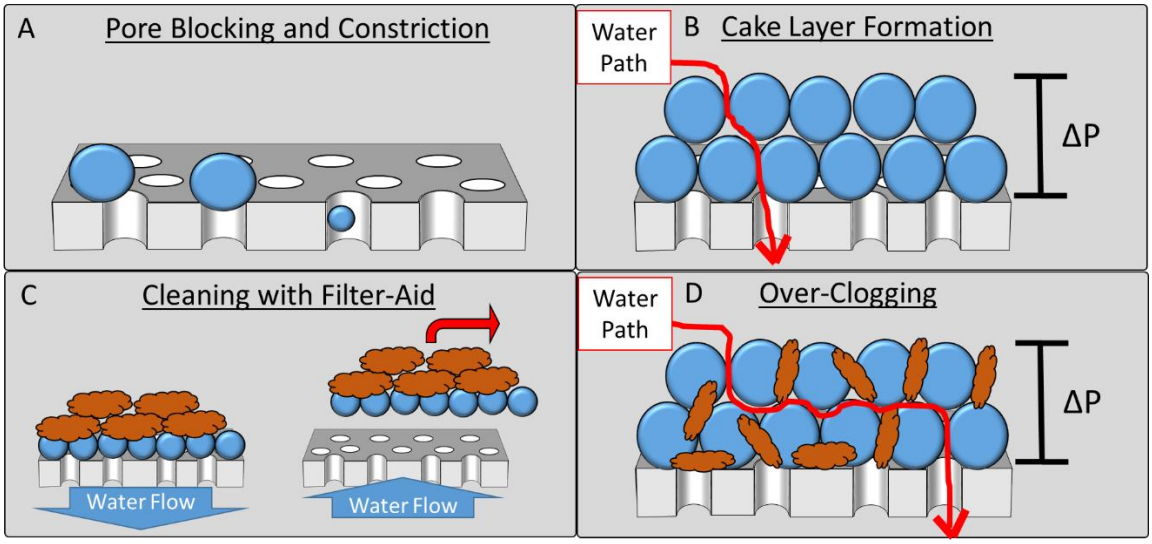

Figure 1.8: Pore blocking and cake layer formation. (A) From left to right, partial pore blocking, complete pore blocking and pore constriction. (B) Cake layer formation showing the torturous water path. (C) Filter-aid formation, where the inert foulant layer prevents active foulants from interacting with membrane surface (shown on left), making it easy to remove the cake layer with a simple back flush (shown on right). (D) Over-clogging of the cake layer which further increase tortuosity of the cake. Inert foulants are shown as blue spheres, and active foulants are shown as brown blobs.

1.4.2 Cake Layer Formation

The *cake layer* formation occurs in all membrane filtration processes where colloidal or particulate material is being removed. During filtration, particulate will build up on the membrane surface and start to accumulate forming a cake layer until an

equilibrium is reached. The equilibrium is reached when the fluid flow shearing the particles of the cake layer becomes greater than the force that pulls the particulate to the membrane surface. Regardless if the equilibrium is reached or not, the formation of the cake layer creates a resistive and torturous pathway for water flow (typically called the cake layer resistance) and results in lower permeate fluxes. The cake layer formation is further affected by the type of foulants that form it. The cake layer formation can act as a "filter-aid", where the first particulate layer that deposits on membrane surface is inactive (i.e. the foulants do not interact with or irreversibly attach to membrane surface) preventing "active" foulants (i.e. those that can irreversibly attach to membrane surface, or chemically alter it) from interacting with membrane surface, making it easy to remove the fouling layer during cleaning with high cross-flows, or back flushing (where water is forced backwards through the membrane) (Fig 1.8C). [81,82] However, the filter-aid does not always form as most real waters (e.g. surface waters, waste waters, etc) contain both active and inactive foulants randomly mixed in and thus the cake can become irreversibly attached due to deposition of active foulants first.[83,84] Furthermore, in most real waters *over-clogging* can occur, where small fouling agents can penetrate the porous structure of the cake layer, clogging the open pores and increasing the cake layer density and resistance to water flow (Fig. 1.8D). [85] The cake layer formation is one of the most prevalent fouling mechanisms in membrane filtration, regardless if its MF or RO, leading to increased operating pressures and reduced permeate fluxes.

1.4.3 Gel Layer Formation, Macromolecules and Ion Bridging

The *gel layer* formation is caused by buildup of macromolecules near a membrane surface, and impacts all membranes process that are removing macromolecules from the feed. During filtration macromolecules build up near the membrane surface forming a concertation polarization layer. [86] Once the critical concentration is reached the macromolecules can form a gel layer which has very low water permeability. The gel formation point is directly related to the permeate flux where a clear fouling event can be observed at a "critical flux point" (i.e. bellow the critical flux the system can operate with no change in permeability for extended periods of time, but once the critical flux is surpassed rapid permeability loss is observed). The gel formation can be intensified by the presence of divalent ions (Ca^{+2}) in the solution, as they can effectively crosslink the macromolecules, or lead to "bridging", where macromolecules are chemically bonded to membrane surface via the divalent ions.[87–90] The ion bridging can lead to rapid and almost irreversible membrane fouling, forming dense and cohesive gel layers. The most common macromolecules that participate in gel formation and bridging are natural organic matter (NOM), extracellular polymeric substances (EPS), sodium alginates, and humic acids which are also most common substances that are found in surface waters and wastewater sources.

1.5 Fouling Prevention of Organic Molecules Using Hydrophilicity and Surface Charge

Membrane modification is probably one of the most commonly researched methods for fouling control with primary goals being focused on increasing membrane surface hydrophilicity and surface charge. [91–95] The UF and MF membranes are commonly made from PS, PVDF, PAN and PTFE which are in general hydrophobic and due to their low surface energy water cannot strongly bind to the surface allowing for hydrophobic foulants to easily adsorb. Studies performed on a modified PS membranes with different hydrophilicities have shown that the membrane fouling increases with decreasing hydrophilicity (i.e. increase in the water contact angle with membrane surface). [96] This observation has led to a large effort to increase membrane hydrophilicity through various methods ranging from polymer modification before synthesis, blending of polymers during the membrane synthesis, or coating membrane surface with polymeric films. [91–95]

One of the most commonly practiced methods of modification on industrial scale is blending, where a hydrophilic polymer is added to the casting solution. The most commonly used polymer is PVP. The PVP is a highly hydrophilic polymer that acts as micro pore forming agent during membrane casting.[97,98] Although PVP readily solubilizes in water, a small quantity of PVP gets trapped in the polymer matrix of the membrane, increasing its hydrophilicity and improving fouling resistance. [99,100] Unfortunately, it has been found that membrane treatment with bleach or sodium hypochlorite, which are commonly used for membrane cleaning, leads to PVP oxidation and results in eventual loss

of surface hydrophilicity.[101,102] An alternative method to blending is surface coating, where a polymer film is deposited on the membrane surface.

Surface coatings are a popular method of membrane modification as it is simple to execute, readily scalable, and can be applied to most membranes post fabrication. The most commonly used hydrophilic polymer is poly (vinyl alcohol) (PVA) as it is environmentally friendly, readily coats and adsorbs to surfaces, and is highly hydrophilic. Although attempts at making pure PVA membranes have been made with some success for application ranging from MF to RO, their industrial implementation is limited by PVA swelling which results in reduced permeate fluxes and changes in rejection properties. [103] However, PVA has found wide application as an antifouling coating applied to membranes ranging from MF to RO demonstrating reduction in fouling of proteins (e.g. BSA) and natural organic matter (e.g. humic acids, or real waters). [104–108] The success of PVA coatings can be attributed to the simple modification process, where simple dip-coating of PVA can lead to adsorption of PVA film on a membrane surface. The PVA layer can be readily immobilized (as it can solubilize in water) through simple heat cycling which crystalizes the PVA (making it insoluble in room temperature water), or through chemical crosslinking with glutaraldehyde or formaldehyde leaving a robust film on the membrane surface. [103,109,110] The simplicity and success of the process has prompted PVA coating utilization in industry, primarily for RO and NF membranes. [111–113]

Fouling resistance of membranes can be further improved through control of surface charge. Most organics and colloids in waters are negatively charged due to presence of carboxylic groups which dissociate in water. The negatively charged foulants in water

can then be repulsed by a negatively charged membrane surface preventing fouling.[114–117] . These observations have prompted allot of work focused on increasing membrane surface charge, and specifically giving them a negative charge. [118–124] The typical approaches include use of charged polymers during membrane synthesis such as sulfonated PS, where the sulfonate group provide a negative charge, or modification of polymer such as PAN with a charged functional group such as styrenesulfonate before casting. [118,125] Alternatively the membranes can be dip coated with a charged polymer and then crosslinked, as has been done with PS membranes that were coated with propane sultone and propylene oxide following a crosslinking process to immobilize the charged groups. [119–121] The most commonly researched technique today is polymer grafting where a membrane surface is "activated" through irradiation with a UV light or plasma treatment allowing for a crosslinking of a negatively charged monomers to the membrane surface. [122] In all cases the increase in negative surface charge reduces membrane fouling with charged proteins, and organics typically found in water. However, the negative charge can increase fouling with positively charged compounds, a case which can occur in industrial waste waters. Fortunately the same techniques as described above can be used to give membranes a positive charge using functional group such as trimethyl ammonium. [126]

1.6 Electrokinetic Fouling Prevention

The electrokinetic fouling control method is probably one of the first active fouling control methods developed in membrane filtration. [127–130] The novelty of the electrokinetic method is application of an external force that pushes foulants away from the membrane

surface, preventing their adhesion and consequent fouling. The electrokinetic fouling control relies on electrophoresis, where an electrical field applies a force on a charged molecule or particle causing it to move in water. The electrical field is generated by placing two electrodes in parallel and on opposite sides of a membrane. Application of a DC potential across the electrodes generates an electrical field that pushes the foulants away from the membrane surface, preventing fouling (Fig 1.9).

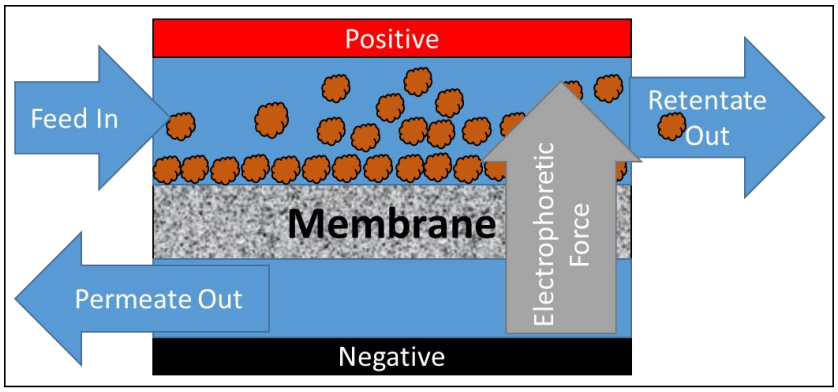

Figure 1.9: Electrokinetic fouling control configuration with positive (red plate) and negative (black plate) electrodes placed in parallel with the membrane surface, generating an electrophoretic force perpendicular to the membrane.

The electrokinetic fouling control saw great success at preventing fouling of colloids and organics such as TiO_2, juice, and bacteria. [127,131–135] However in almost all cases to reduce fouling strong electrical fields had to be applied on order of 10-200 V/cm for colloidal foulants, and on order of 100-1000 V/cm for organic foulants. [127,131,134,135] The application of such high potential fields resulted in high current demand, although generally power consumption data was not presented, earlier papers reported power consumption on order of 5-20 kW/m^2. [127,131] Furthermore, if the electrodes were not properly insulated the application of large potentials lead to formation of anodic and cathodic reactions that could lead to rapid electrode degradation. One of the outliers of

electrokinetic process was fouling prevention in bioreactors in which application of small electrical fields (<6 V/cm) improved system performance by preventing adhesion of activated sludge to the membrane surface. [132,133] The significant improvement in these systems was attributed to better electrode placement configuration, and impact of electrical field on the activated sludge behavior.

The primary challenge electrokinetic filtration faces is the configuration of electrodes and high power demand. The electrophoretic force is directly related to the magnitude of the applied electrical field which is controlled be the electrode separation distance and magnitude of the applied electrical potential. The membrane thickness and required space for water flow in the feed and permeate channel results in a minimum electrode separation of roughly 1 cm and thus to generate a 100 V/cm electrical field a 100 V potential difference between electrodes would have to be applied. The high potential results in high energetic consumption as the electrodes can participate in electrochemical reactions. The resulting complexity of the design and high energetic cost in the end have prevented implementation of the electorkinetic fouling control methods for industrial and general water treatment applications. However, the electrokinetic fouling control has shown to be effective during pilot scale studies of biopolymer and concentrated slurry separation, application where water treatment is especially challenging. [136,137]

1.7 Treatment of Oil Emulsions

Oil emulsions are probably one of the most challenging contaminants to remove from water. Although in general oil is thought of being immiscible in water it can form

small oil droplets (i.e. oil emulsions). The oil droplets are stabilized through presence of naturally occurring surfactant agents, that give the oil droplets both electrostatic charge, hydrophilic surface (i.e. surfactants), and/or provide a steric hindrance that prevents their coalescence. Crude oil emulsions that are commonly present in produced water and flow back water generated during drilling operations are stabilized through presence of asphaltenes, carboxylic acids, and napthanic acids that contain both hydrophilic charged groups and hydrophobic groups. [138,139] In general the hydrophobic groups partition into the oil phase, while the hydrophilic groups remain on the oil droplets surface preventing their coalesce or aid in attachment to hydrophilic surfaces. Furthermore, the oil droplets range in size from tens of nanometers to microns, and can remain uniformly distributed throughout the solution for extended periods. Thus, water that contains oil emulsions require extensive treatment before it can be discharged in to the environment.

The treatment of oil emulsions and their removal from water is not trivial and is typically dictated by the size of the oil droplets and water chemistry. [140,141] The large oil droplets (>150 μm in size) can be removed using classical API gravity separator, while the midsize droplets (150-10 μm) require use of advanced and energy intensive processes such as induced gas floatation (drop size >25 μm) or a hydrocyclone (drop size >10 μm). Droplets with size bellow 10 μm require use of centrifugation, mesh coalescence or media filters, and out of the three only centrifugation can remove droplets with size near 2 μm. The largest drawback of all these technologies is their inability to guarantee permeate quality, as the removal efficiency is strongly affected by the feed water quality (e.g. salinity, surfactants, temperatures) and proper unit operation (e.g. prone to operator errors).

Membrane filtration is the only technology that can guarantee removal of all oil droplets with a certain size and achieve desired permeate quality, where membrane pore size dictates the size and efficiency of oil drop removal. Unfortunately, filtration membranes experience rapid fouling during treatment of oily waters, resulting in irreversible loss of membrane permeability and requiring aggressive cleaning or entire membrane replacement.

Oil fouling in membrane filtration is an issue with no single solution, as the fouling is dependent on both the oil drop-membrane interaction and the oil drop-oil drop interactions, where the membrane properties and feed water properties dictate how the membranes fouls. The oil fouling mechanisms are further complicated by the fact that oil drops can behave as particulate foulants and transition to behaving as a liquid (e.g. similar to gel-layer fouling). Oil droplets in the initial stages of filtration and/or when they are particularly stable exhibit pore constriction, pore blocking, and cake layer fouling mechanisms.[142] These fouling mechanisms are further complicated by the fact that the oil drops are liquid, allowing them to deform, spread, and coalesce (where two oil drops combine to from a larger drop). The oil droplets that contact the membrane surface (after overcoming the repulsive forces) will naturally wet it so as to minimize the oil drops surface energy. [143,144] The wetting of the membrane surface with oil can lead to oil diffusion into the membrane polymer structure as most membranes made from PS and PAN are not chemically crosslinked. Thus, the wetting can result in irreversible change of membrane hydrophobicity, chemical structure, and lead to pore blocking. Furthermore, the stabilizing agents such as napthanic acids and ashpaltenes can act as surfactants allowing oil to interact

even with oleophobic and hydrophilic membranes leading to their wetting and irreversible loss of permeability.

The challenges of treating oil does not end with oil drop-membrane surface interaction. The filtration of oil droplets leads to a formation of a cake layer on the membrane surface, which can transform into an oil film due to coalescence. The cake layers are initially made up of individual oil droplets and behave similarly to colloid cake layers.[145] The cake layer however can go through a transition where the oil droplets coalesce.[146] Coalescence of oil is driven by the pressure drop across the cake layer, van der Waal, and hydrophobic attraction forces that push the oil droplets together, while electrostatic and steric interactions keep the oil droplets apart. Once the electrostatic and steric forces are overcome the oil droplets come in contact and coalesce to minimize their surface energy (e.g. the surface area per volume of oil will decrease with each coalescence event reducing their surface energy (due to reduction of the number of oil molecules interacting with water)). The coalescence of the oil droplets results in a formation of an oil film, which is impermeable to water flow and leads to a rapid decline in permeate flux. The formation of the oil film can further lead to complete membrane oil wetting, an event that generally requires complete membrane replacement.

Oil fouling prevention has been primarily approached via control of membrane surface properties to increase their resistance to oil wetting and adhesion. The primary approaches have been focused on increasing membrane oleophobicity and hydrophilicity using either blending or surface modification approaches. PVDF membranes have good resistance to sorption of oil and can be readily casted using the phase inversion process

allowing for their modification via blending. Large number of polymers have been used to modify membranes ranging from simple polymers such as poly(methacrylic acid) (PMMA) and sulfonated poly(carbonate) (SPC) to exotic amphiphilic copolymers. [147–149] Blending with simple polymers such as PMMA and SPC yielded membranes with good hydrophilic surface and contact angles with water on order of 40-50 degrees. However, these polymers have poor compatibility with PVDF leading to inhomogeneous polymer distribution and allowing for partial membrane fouling. The use of amphiphilic polymers attempts to solve the problem of inhomogeneity as these polymers have compatible hydrophobic groups that partition in PVDF and hydrophilic groups that partition on membrane surface, demonstrating improved fouling resistance to oil. Surface modification has also been utilized, with most approaches been focused on grafting either polymer groups with low surface energy, or zwitterionic polymers which yielded increased resistance to oil adhesion and fouling. [150,151]

The final group of membranes have been prepared from novel polymers and nanomaterials that exhibit super-oleophobic and super-hydrophilic properties. The super-oleophobicity and super-hydrophilicity are only attainable through synthesis of membranes with proper materials and micro-structured surfaces which amplify their hydrophilic and oleophobic properties.[143] There are two accepted models that describe the super hydrophilicity/oleophobicity of a surface. The Wenzel model where the microstructure is in full contact with the wetting fluid, and Cassie-Baxter model where the wetting fluid is suspended over the surface by the microstructures. The amplification of the hydrophilicity/oleophobicity is due to increased surface area of the material and inclusion

of physical “locks” that lock the fluid in place preventing it from spreading across the surface. In either cases the microstructure must be ordered and well defined to exhibit these super-oleophobic and super-hydrophilic states. Finally, it should be noted that it is significantly easier to prepare an underwater super-hydrophilic and super-oleophobic surface then in air due to the large difference in surface tensions between water and air. Regardless of these challenges many super-hydrophilic and/or super-oleophobic materials have been prepared with aim to remove oil emulsions from water.

Majority of super-oleophobic and super-hydrophilic membranes prepared to-date are large microporous meshes, which although exhibit incredible hydrophilic and oleophobic properties cannot reject real oil emulsions with droplet size bellow several microns. Such meshes were prepared by growing silicon nano-wires on meshes, oxidizing copper meshes, coating of meshes with polyacrylamide hydrogels and various other materials deposited or grown on mesh substrate.[152–156] Electrospinning has shown some promise at synthesizing membranes with sub-micron pore structures and producing true MF membranes for oil-water separation. Through electrospinning of polyvinylidene fluoride-co-hexafluoropropylene it was possible to create a super-oleophobic membrane that showed good results at removing micron sized oil droplets from water and showing limited fouling, achieving removal of up to 99% of corn oil, gasoline and motor oils. Unfortunately, this membrane was not able to effectively treat crude oil emulsions with rejection of only 90%.[157] Alternative method of preparing super-oleophobic membranes was demonstrated by forcing formation of microstructures in the polymer during the casting process. One such instance was demonstrated through addition of ammonia to

PVDF casting solution, which caused local microphase separation during the phase inversion casting process resulting in formation of PVDF spherical clusters. [158] These membranes demonstrated high fluxes and good separation of surfactant stabilized oils achieving separation of up to 99%, however even these membranes showed slow loss of permeability. Even though large number of membranes have been prepared for oil separation over the last two decades, to this date none of the membranes could solve the issue of oil fouling, which alone highlights the challenge of treating oily waters with membranes and promoted interest in use of magnetic Pickering emulsions as an alternative treatment method.

The Pickering emulsion formation has been observed as early as 1903 when it was found that fine particles would assemble at water and oil droplet interface, leading to oil drop stabilization.[159] Since then Pickering emulsions were prepared for a large number of applications using variety of nanoparticles ranging from silica to magnetite. [160–165] The Pickering emulsion formation is driven by the solvation and hydrophobic forces, where a nanoparticle that has both hydrophobic and hydrophilic groups minimizes its energy state by partitioning to the oil/water interface. [166] This driving force leads to spontaneous formation of Pickering emulsions when nanoparticles are added to oil emulsions making them simple to prepare. The simplicity of Pickering emulsion preparation and the low cost of magnetic nanoparticles has attracted allot of interest in their utilization for oil emulsion treatment. The general concept is to use magnetic nanoparticles to coat oil droplets in water and then concentrate them using a magnetic field. [163,164,166,167] Furthermore, sufficiently strong magnetic fields can separate the nanoparticles from the oil allowing for their re-use.

[166] However, magnetic Pickering emulsions for oil/water separation have seen limited industrial application due the rapid decay in magnetic field strength away from magnetic surfaces. This limitation has made it challenging to collect the Pickering emulsions from vast quantities of oily waters and thus limited their application. Furthermore, the magnetic Pickering emulsions treatment process just like the classical separation processes does not guarantee complete oil removal.

1.8 Treatment of Saline Brines with Membrane Distillation

The global climate change is reducing the availability of water in many regions, causing extended droughts. The water shortages have prompted allot of areas to consider treating non-conventional waters such as saline produced waters (e.g. produced water for Marcellus shale) and brine waste from seawater desalination. Furthermore, land locked regions are starting to look at treating saline ground water, where discharge of brines can be a challenge. Although RO is a de facto treatment technology for seawater it is unable to treat high salinity brines as the osmotic pressure rapidly increases with salt content. [168,169] This has promoted allot of interest in developing thermally drive membrane distillation process, which is not strongly affected by salt content.

1.8.1 Membrane Distillation Operation

The membrane distillation process utilizes a hydrophobic membrane as a vapor forming interface, which typically separates the hot feed and cold draw solutions, where the difference in temperature between the two solutions drives water vapor formation and transport. [170] The difference in temperature is required to maintain vapor transport through

the membrane, where the water vapor forms at the hot feed/membrane interface, diffuses through the membrane and condenses at the cold draw/membrane interface. During the operation, the hot feed cools down due to the enthalpy of vaporization of water, and due to conductive heat transfer through the membrane, while the cold draw warms up due to water condensation and conductive heat transfer. These heat transfer processes result in thermal polarization in both the direction away from membrane surface and along the membrane surface, leading to reduced vapor pressure and permeate flux. To combat these thermal losses multiple modes of operation have been developed, where simplicity is sacrificed for reduction in thermal losses and increased permeate flows.

The *direct contact membrane distillation* (DCMD) is the simplest and most commonly utilized operational mode, herein the hot feed water flows through the feed channel and is in direct contact with the membrane, while a cold water draw solution flows in counter current configuration through the draw channel and is also in direct contact with the membrane surface. The water vapor forms at the hot feed/membrane interface and diffuses through the pores where the vapor condenses at the cold water/membrane interphase and is carried away by the draw water. To maintain high performance, typically high cross flow velocities are used for both feed channel and the draw channel leading to reduced thermal polarization. Although DCMD is simple to configure its suffers from heat loss by conduction. To reduce thermal losses due to conduction *sweeping gas membrane distillation* (SGMD) configuration can be used. Herein the draw water is replaced by inert gas that sweeps the vapor away from the membrane, and the vapor is condensed outside the cell. The SGMD requires high gas flow rates to maintain low water vapor concentration

in the feed channel, which maintains high vapor diffusion rates through the membrane. However, this leads to the need for high area condensers to remove the vapor from the gas stream which can be expensive to operate.

The *air gap membrane distillation* (AGMD) is designed to reduce thermal losses due to conduction. Herein the feed operates in same manner as in DCMD and is in direct contact with the membrane. However instead of a water draw solution there is an air gap between the membrane and a cooling plate. The vapor still forms at the hot feed/membrane interface but now it diffuses through the membrane and the air gap and then condenses on the cold plate where the condensate flows out by gravity. This configuration however suffers from diffusion limitation as the vapor must diffuse through the membrane and stagnant air, leading to strong vapor concentration polarization effect and reduced permeate flows. An alternative configuration is *vacuum membrane distillation* (VMD), where the draw channel is put under vacuum, removing the water vapor from the draw channel, with the vapor being condensed outside the cell similar to SGMD. The VMD operation solves the vapor diffusion limitation present in AGMD operation, the vapor polarization in SGMD, and conductive heat transfer losses present in DCMD. However, the VMD process is highly dependent on applied vacuum pressure which can promote membrane wetting (as liquid water can be pulled through the pores of the membrane) and the cost of vacuum operation can make the overall process expensive.

1.8.2 Membrane Distillation Challenges

MD is a very promising technique for treating saline waters, however it must overcome many challenges before being used successfully on industrial scale, including fouling, membrane wetting and scale up problems.

1.8.2.1 MD Fouling and Wetting

MD faces same fouling problems that typical membrane filtration faces ranging from pore blocking to cake layer formation. Furthermore, MD membranes must be hydrophobic as to prevent water entry into the pores and thus they have very little to no electrostatic charge leading to high fouling rates when treating water with colloidal and organic foulants. The adherence of foulants to the membrane surface, pore blocking and cake layer formation leads to reduced water vapor flux due to reduced number of open pores. [171] Furthermore, the buildup of the cake layer adds additional thermal resistance, which reduces the temperature at the vapor-forming interface, leading to lower permeate fluxes. [172] One further problem MD faces during fouling is membrane wetting. Adsorption of organic molecules to MD membrane pores can lead to membrane hydrophilization, which can result in water entering the membrane pores (i.e. pore wetting). The pore wetting results in loss of rejection as dissolved salts and contaminants can pass through the membrane, as well as lead to reduced permeate fluxes.[173] Finally, the biggest challenge for MD is that the membranes cannot be modified using classical methods as the pore structure has to be hydrophobic thus fouling prevention is limited to feed pretreatment, or using materials that have such low surface energy that foulants cannot irreversibly attach.

1.8.2.2 Scale up Challenges

MD is an energetically intensive process due to high enthalpy of vaporization of water. The thermal energy in MD is delivered through pre-heating of the feed and is reliant on the heat capacity of the water to transfer the energy from the heating unit to the actual vapor forming interface inside the membrane module. The vapor formation and the conductive heat transfer through the membrane lead to rapid cooling of the feed water and loss of the thermal driving force, which results in reduced vapor formation rate. Furthermore, this leads to rapid heating of the draw, especially in DCMD and SGMD operational modes, which requires use of high cross-flow velocities to maintain the temperatures gradient across the membrane module. Due to the high cross flows in MD large quantities of thermal energy get trapped in feed and draw outflow streams, requiring use of heat exchangers to recover the heat from the warm draw and transfer it to the cool feed. Furthermore, the high cross flow velocities result in low single pass recoveries, with theoretical maximum being 6.5%, but in practice, the actual recoveries can be much lower. [174] This has led to complicated MD plant designs, which leads to high capital and operational costs.

The goal of MD process is to treat highly saline brines, and recover as much water from the saline brines as possible, thus the overall recovery rates of at least 50% should be archivable, but cannot be accomplished with a simple single pass process normally used in membrane filtration. The low single pass recoveries of MD can be overcome with a batch or psudo-batch operation. The batch MD process utilizes complete recirculation of the feed, which is recirculated until the desired recovery has been achieved, upon which the

concentrated feed is disposed of and replenished with the fresh feed. The pseudo-batch operation is performed by recirculating the feed, but allowing it to concentrate until desired recovery rate is achieved, upon which some of the feed gets bled off, and replenished with new feed in a steady-state manner allowing for continuous operation. Regardless both processes imply that all the feed modules, pipes, pumps and heat exchangers operate at final recovery salt concentration (e.g. if the desired recovery is 50% and the starting feed salt concentration is 50g/L then the final recovery salt concentration is 100 g/L). The high salt concentrations and elevated temperatures can lead to scaling, increased fouling rates and rapid corrosion of metals, requiring use of Nickle Alloys, which increase the overall process capital costs. [175] An alternative configuration that can achieve higher recovery rates is cascade configuration where the feed is passed through multiple membrane modules in series, with a heat exchanger and heater in between every module unit.[176] The advantage of cascade operation is that not all modules and heat exchangers would be operating at final recovery salt concentration, but instead salt content will increase from one unit to the next. However, since multiple heat exchangers and heating units would have to be used the construction and operation of such process will be much more complicated than the pseudo-batch type operation. The high capital and operational costs have so far limited the implementation of MD on industrial scale.

1.9 Summary of Dissertation

The dissertation presents synthesis and application of nanomaterial based thin-film coatings for enhancement of membrane filtration processes. The goal of the thin-film is to

actively address or take advantage of a mechanism that can improve the overall membrane filtration process. It is demonstrated that via careful selection of proper nanomaterials and their assembly into a thin-film it is possible to actively control the membrane fouling behavior and the driving forces in the membrane filtration processes. The performance of the nanomaterial based thin-films is explored using experimental filtration systems, where the results are explained through theoretical models that quantitively or qualitatively predict observed experimental results.

Chapter 2 presents the application of conductive carbon nanotube (CNT) thin-films for fouling prevention of charged organic molecules. The CNT films were prepared through pressure deposition of CNTs onto UF membranes, and crosslinked with PVA, forming highly conductive and stable films. It is shown that application of low electrical potentials to CNT film prevents membrane fouling when treating high concentration of sodium alginate solutions and synthetic wastewaters. The solution of modified Poisson-Boltzmann equation demonstrates that high electrostatic forces are generated at applied potentials and qualitatively explain the observed experimental results. Furthermore, the fouling was prevented with applications of low electrical potentials leading to low power consumption of $10x10^{-3}$ kWh/m^2 which is orders of magnitude lower then classical electrokinetic based approaches

Chapter 3 explores the coupling of Pickering emulsions to ultrafiltration processes and allowing treatment of high concentration crude oil emulsions. The Pickering emulsions are prepared with magnetite nanoparticles which form a thin-film on oil drop surface. The nanoparticle film prevents oil-coalescence and membrane wetting by forming a physical

barrier between oil droplet and membrane surface. Through coupling of the Pickering emulsion to CNT-PVA coated membranes, which exhibit under water super-oleophobic properties, it was possible to treat high concentration oil emulsions (10 g/L) without fouling. Furthermore, a theoretical framework is presented that predicts critical flux point at which membrane fouling would occur based on nanoparticle and membrane hydrophilicity.

Chapter 4 presents how CNT films deposited on hydrophobic membranes can be used as joule heaters generating the thermal driving force in MD process while treating highly saline brines. This is the first time that such operation is shown to be possible, where application of AC potentials at moderate frequencies is used to prevent surface charging of the CNT films and their degradation. Electrical impedance spectroscopy is used to study the relationship between applied AC frequency and CNT degradation, from which an equivalent circuit is developed to show electron flow through the immersed CNT films. Using the equivalent circuit, it is demonstrated that the AC frequency directly controls the number of electrons that can participate in CNT degradation reactions. Long term reactions confirmed that CNT joule heaters can be operated for extended periods of time at moderate frequencies between 10 kHz and 100 Hz. Finally, it is demonstrated that CNT joule heaters can be used to drive the MD process, achieving single pass recoveries that far exceed the theoretical limit of 6.5%.

Finally, chapter 5 presents the main conclusions of the presented dissertation, and their implication for membrane filtration processes. Furthermore, we present potential future work and broader impacts of the developed nanomaterial thin-films.

1.10 References

1. Tanaka, S. K. *et al.* Climate Warming and Water Management Adaptation for California. *Clim. Change* **76,** 361–387 (2006).

2. Mote, P. W., Hamlet, A. F., Clark, M. P. & Lettenmaier, D. P. DECLINING MOUNTAIN SNOWPACK IN WESTERN NORTH AMERICA*. *Bull. Am. Meteorol. Soc.* **86,** 39–49 (2005).

3. Barnett, T. *et al.* The effects of climate change on water resources in the west: introduction and overview. *Clim. Change* **62,** 1–11 (2004).

4. Bechhold, H. Kolloidstudien mit der Filtrationsmethode. *Z. Für Elektrotechnik Elektrochem.* **13,** 527–533 (1907).

5. Hermes, M. E. *Enough for one lifetime: Wallace Carothers, inventor of nylon*. (American Chemical Society and the Chemical Heritage Foundation, 1996).

6. Glater, J. The early history of reverse osmosis membrane development. *Desalination* **117,** 297–309 (1998).

7. Loeb, S. & Sourirajan, S. Sea Water Demineralization By Means of An Osmotic Membrane. *Adv. Chem. Ser* **38,** 117–132 (1962).

8. Strathmann, H. & Kock, K. The formation mechanism of phase inversion membranes. *Desalination* **21,** 241–255 (1977).

9. Lalia, B. S., Kochkodan, V., Hashaikeh, R. & Hilal, N. A review on membrane fabrication: Structure, properties and performance relationship. *Desalination* **326,** 77–95 (2013).

10. Flemming, H.-C. Reverse osmosis membrane biofouling. *Exp. Therm. Fluid Sci.* **14,** 382–391 (1997).

11. Cadotte, J. E., King, R. S., Majerle, R. J. & Petersen, R. J. Interfacial Synthesis in the Preparation of Reverse Osmosis Membranes. *J. Macromol. Sci. Part - Chem.* **15,** 727–755 (1981).

12. Riley, R. L. *et al.* Spiral-wound poly (ether/amide) thin-film composite membrane systems. *Desalination* **19,** 113–126 (1976).

13. Sarada, T., Sawyer, L. C. & Ostler, M. I. Three dimensional structure of celgard® microporous membranes. *J. Membr. Sci.* **15,** 97–113 (1983).

14. Sadeghi, F., Ajji, A. & Carreau, P. Analysis of microporous membranes obtained from polypropylene films by stretching. *J. Membr. Sci.* **292,** 62–71 (2007).

15. Zhu, W. *et al.* A Novel Polypropylene Microporous Film. *Polym. Adv. Technol.* **7,** 743–748 (1996).

16. Kim, J., Kim, S. S., Park, M. & Jang, M. Effects of precursor properties on the preparation of polyethylene hollow fiber membranes by stretching. *J. Membr. Sci.* **318,** 201–209 (2008).

17. Tabatabaei, S., Carreau, P. & Ajji, A. Microporous membranes obtained from polypropylene blend films by stretching. *J. Membr. Sci.* **325,** 772–782 (2008).

18. Kurumada, K. *et al.* Structure generation in PTFE porous membranes induced by the uniaxial and biaxial stretching operations. *J. Membr. Sci.* **149,** 51–57 (1998).

19. Sadeghi, F., Tabatabaei, S. H., Ajji, A. & Carreau, P. J. Effect of PVDF characteristics on extruded film morphology and porous membranes feasibility by stretching. *J. Polym. Sci. Part B Polym. Phys.* **47,** 1219–1229 (2009).

20. Sadeghi, F., Ajji, A. & Carreau, P. J. Microporous membranes obtained from polypropylene blends with superior permeability properties. *J. Polym. Sci. Part B Polym. Phys.* **46,** 148–157 (2008).

21. Fleischer, R. L., Price, P. B. & Walker, R. M. *Nuclear tracks in solids: principles and applications*. (University of California Press, 1975).

22. Apel, P. Track etching technique in membrane technology. *Radiat. Meas.* **34,** 559–566 (2001).

23. Komaki, Y., Ishikawa, N. & Sakurai, T. Effects of gamma rays on etching of heavy ion tracks in polyimide. *Radiat. Meas.* **24,** 193–196 (1995).

24. Starosta, W., Wawszczak, D., Sartowska, B. & Buczkowski, M. Investigations of heavy ion tracks in polyethylene naphthalate films. *Radiat. Meas.* **31,** 149–152 (1999).

25. Komaki, Y. & Tsujimura, S. Growth of fine holes in polyethylenenaphthalate film irradiated by fission fragments. *J. Appl. Phys.* **47,** 1355–1358 (1976).

26. Kim, J., Kim, S. S., Park, M. & Jang, M. Effects of precursor properties on the preparation of polyethylene hollow fiber membranes by stretching. *J. Membr. Sci.* **318,** 201–209 (2008).

27. Prince, J. A. *et al.* Preparation and characterization of highly hydrophobic poly(vinylidene fluoride) – Clay nanocomposite nanofiber membranes (PVDF–clay NNMs) for desalination using direct contact membrane distillation. *J. Membr. Sci.* **397–398,** 80–86 (2012).

28. Gopal, R. *et al.* Electrospun nanofibrous filtration membrane. *J. Membr. Sci.* **281,** 581–586 (2006).

29. Bhardwaj, N. & Kundu, S. C. Electrospinning: A fascinating fiber fabrication technique. *Biotechnol. Adv.* **28,** 325–347 (2010).

30. Feng, C. *et al.* Production of drinking water from saline water by air-gap membrane distillation using polyvinylidene fluoride nanofiber membrane. *J. Membr. Sci.* **311,** 1–6 (2008).

31. Kaur, S., Rana, D., Matsuura, T., Sundarrajan, S. & Ramakrishna, S. Preparation and characterization of surface modified electrospun membranes for higher filtration flux. *J. Membr. Sci.* **390–391,** 235–242 (2012).

32. Maab, H. *et al.* Synthesis and fabrication of nanostructured hydrophobic polyazole membranes for low-energy water recovery. *J. Membr. Sci.* **423–424,** 11–19 (2012).

33. Wang, R., Liu, Y., Li, B., Hsiao, B. S. & Chu, B. Electrospun nanofibrous membranes for high flux microfiltration. *J. Membr. Sci.* **392–393,** 167–174 (2012).

34. Zhao, Z., Zheng, J., Wang, M., Zhang, H. & Han, C. C. High performance ultrafiltration membrane based on modified chitosan coating and electrospun nanofibrous PVDF scaffolds. *J. Membr. Sci.* **394–395,** 209–217 (2012).

35. Bui, N.-N., Lind, M. L., Hoek, E. M. V. & McCutcheon, J. R. Electrospun nanofiber supported thin film composite membranes for engineered osmosis. *J. Membr. Sci.* **385–386,** 10–19 (2011).

36. Saffman, P. G. T. The lift on a small sphere in a slow shear flow. *J. Fluid Mech.* **22,** 385–400 (1965).

37. O'neill, M. E. A sphere in contact with a plane wall in a slow linear shear flow. *Chem. Eng. Sci.* **23,** 1293–1298 (1968).

38. Goren, S. L. The normal force exerted by creeping flow on a small sphere touching a plane. *J Fluid Mech* **41,** 619–625 (1970).

39. Dandy, D. S. & Dwyer, H. A. A sphere in shear flow at finite Reynolds number: effect of shear on particle lift, drag, and heat transfer. *J. Fluid Mech.* **216,** 381–410 (1990).

40. Chaoui, M. & Feuillebois, F. Creeping flow around a sphere in a shear flow close to a wall. *Q. J. Mech. Appl. Math.* **56,** 381–410 (2003).

41. Verwey, E. & Overbeek, T. *Theory of stabilty of lyophobic colloids*. (Elsievier Publishing Company, 1948).

42. Derjaguin, B. On the repulsive forces between charged colloid particles and on the theory of slow coagulation and stability of lyophobe sols. *Trans. Faraday Soc.* **35,** 203–215 (1940).

43. Bell, G. M. & Peterson, G. C. Calculation of the electric double-layer force between unlike spheres. *J. Colloid Interface Sci.* **41,** 542–566 (1972).

44. Ohshima, H. Diffuse double layer interaction between two parallel plates with constant surface charge density in an electrolyte solution. *Colloid Polym. Sci.* **252,** 257–267 (1974).

45. Carnie, S. L., Chan, D. Y. & Gunning, J. S. Electrical double layer interaction between dissimilar spherical colloidal particles and between a sphere and a plate: The linearized poisson-boltzmann theory. *Langmuir* **10,** 2993–3009 (1994).

46. Faibish, R. S., Elimelech, M. & Cohen, Y. Effect of interparticle electrostatic double layer interactions on permeate flux decline in crossflow membrane filtration of colloidal suspensions: an experimental investigation. *J. Colloid Interface Sci.* **204,** 77–86 (1998).

47. Bergendahl, J. & Grasso, D. Prediction of colloid detachment in a model porous media: hydrodynamics. *Chem. Eng. Sci.* **55,** 1523–1532 (2000).

48. Mosley, L. M., Hunter, K. A. & Ducker, W. A. Forces between Colloid Particles in Natural Waters. *Environ. Sci. Technol.* **37,** 3303–3308 (2003).

49. Liang, Y., Hilal, N., Langston, P. & Starov, V. Interaction forces between colloidal particles in liquid: Theory and experiment. *Adv. Colloid Interface Sci.* **134–135,** 151–166 (2007).

50. Boström, M., Williams, D. R. M. & Ninham, B. W. Specific Ion Effects: Why DLVO Theory Fails for Biology and Colloid Systems. *Phys. Rev. Lett.* **87,** (2001).

51. Outhwaite, C. W. & Bhuiyan, L. B. An improved modified Poisson–Boltzmann equation in electric-double-layer theory. *J. Chem. Soc. Faraday Trans. 2 Mol. Chem. Phys.* **79,** 707–718 (1983).

52. Bratko, D. & Vlachy, V. An application of the modified Poisson-Boltzmann equation in studies of osmotic properties of micellar solutions. *Colloid Polym. Sci.* **263,** 417–419 (1985).

53. Borukhov, I., Andelman, D. & Orland, H. Steric effects in electrolytes: A modified Poisson-Boltzmann equation. *Phys. Rev. Lett.* **79,** 435 (1997).

54. López-García, J. J., Horno, J. & Grosse, C. Poisson–Boltzmann Description of the Electrical Double Layer Including Ion Size Effects. *Langmuir* **27,** 13970–13974 (2011).

55. Hamaker, H. C. The London—van der Waals attraction between spherical particles. *Physica* **4,** 1058–1072 (1937).

56. Leikin, S., Parsegian, V. A., Rau, D. C. & Rand, R. P. Hydration forces. *Annu. Rev. Phys. Chem.* **44,** 369–395 (1993).

57. Parsegian, V. A., Rand, R. P. & Fuller, N. L. Direct osmotic stress measurements of hydration and electrostatic double-layer forces between bilayers of double-chained ammonium acetate surfactants. *J. Phys. Chem.* **95,** 4777–4782 (1991).

58. Rau, D., Lee, B. & Parsegian, V. A. Measurement of the repulsive force between polyelectrolyte molecules in ionic solution: hydration forces between parallel DNA double helices. *Proc. Natl. Acad. Sci.* **81,** 2621–2625 (1984).

59. Grasso*, D., Subramaniam, K., Butkus, M., Strevett, K. & Bergendahl, J. A review of non-DLVO interactions in environmental colloidal systems. *Rev. Environ. Sci. Biotechnol.* **1,** 17–38 (2002).

60. Ruckenstein, E. & Manciu, M. The Coupling between the Hydration and Double Layer Interactions. *Langmuir* **18,** 7584–7593 (2002).

61. Leikin, S. & Kornyshev, A. A. Theory of hydration forces. Nonlocal electrostatic interaction of neutral surfaces. *J. Chem. Phys.* **92,** 6890 (1990).

62. Israelachvili, J. & Wennerström, H. Role of hydration and water structure in biological and colloidal interactions. *Nature* **379,** 219–225 (1996).

63. Leckband, D. & Israelachvili, J. Intermolecular forces in biology. *Q. Rev. Biophys.* **34,** 105 (2001).

64. Israelachvili, J. N. & Wennerstroem, H. Hydration or steric forces between amphiphilic surfaces? *Langmuir* **6,** 873–876 (1990).

65. Claesson, P. M. & Christenson, H. K. Very long range attractive forces between uncharged hydrocarbon and fluorocarbon surfaces in water. *J. Phys. Chem.* **92,** 1650–1655 (1988).

66. Israelachvili, J. & Pashley, R. The hydrophobic interaction is long range, decaying exponentially with distance. *Nature* **300,** 341–342 (1982).

67. Rabinovich, Y. I. & Derjaguin, B. V. Interaction of hydrophobized filaments in aqueous electrolyte solutions. *Colloids Surf.* **30,** 243–251 (1988).

68. Eriksson, J. C., Ljunggren, S. & Claesson, P. M. A phenomenological theory of long-range hydrophobic attraction forces based on a square-gradient variational approach. *J. Chem. Soc. Faraday Trans. 2 Mol. Chem. Phys.* **85,** 163–176 (1989).

69. Ruckenstein, E. & Churaev, N. A possible hydrodynamic origin of the forces of hydrophobic attraction. *J. Colloid Interface Sci.* **147,** 535–538 (1991).

70. Milner, S. T., Witten, T. A. & Cates, M. E. Theory of the grafted polymer brush. *Macromolecules* **21,** 2610–2619 (1988).

71. Ingersent, K., Klein, J. & Pincus, P. Interactions between surfaces with adsorbed polymers: poor solvent. 2. Calculations and comparison with experiment. *Macromolecules* **19,** 1374–1381 (1986).

72. Ingersent, K., Klein, J. & Pincus, P. Forces between surfaces with adsorbed polymers. 3. Θ solvent. Calculations and comparison with experiment. *Macromolecules* **23,** 548–560 (1990).

73. Israelachvili, J. N., Tirrell, M., Klein, J. & Almog, Y. 'acov. Forces between two layers of adsorbed polystyrene immersed in cyclohexane below and above the $þeta$ temperature. *Macromolecules* **17,** 204–209 (1984).

74. Rossi, G. & Pincus, P. A. Interactions between unsaturated-polymer adsorbed surfaces. *EPL Europhys. Lett.* **5,** 641 (1988).

75. HERMIA, J. CONSTANT PRESSURE BLOCKING FILTRATION LAWS - APPLICATION TOPOWER-LAW NON-NEWTONIAN FLUIDS. *TRANS INST CHEM ENG* **60,** 183–187 (1982).

76. Field, R. W. & Wu, J. J. Modelling of permeability loss in membrane filtration: Re-examination of fundamental fouling equations and their link to critical flux. *Desalination* **283,** 68–74 (2011).

77. Wang, F. & Tarabara, V. V. Pore blocking mechanisms during early stages of membrane fouling by colloids. *J. Colloid Interface Sci.* **328,** 464–469 (2008).

78. Ang, W. & Elimelech, M. Protein (BSA) fouling of reverse osmosis membranes: Implications for wastewater reclamation. *J. Membr. Sci.* **296,** 83–92 (2007).

79. Plumlee, M. H., López-Mesas, M., Heidlberger, A., Ishida, K. P. & Reinhard, M. N-nitrosodimethylamine (NDMA) removal by reverse osmosis and UV treatment and analysis via LC–MS/MS. *Water Res.* **42,** 347–355 (2008).

80. Wang, Y.-N. & Tang, C. Y. Protein fouling of nanofiltration, reverse osmosis, and ultrafiltration membranes—The role of hydrodynamic conditions, solution chemistry, and membrane properties. *J. Membr. Sci.* **376,** 275–282 (2011).

81. Güell, C., Czekaj, P. & Davis, R. H. Microfiltration of protein mixtures and the effects of yeast on membrane fouling. *J. Membr. Sci.* **155,** 113–122 (1999).

82. Hughes, D. & Field, R. W. Crossflow filtration of washed and unwashed yeast suspensions at constant shear under nominally sub-critical conditions. *J. Membr. Sci.* **280,** 89–98 (2006).

83. Jermann, D., Pronk, W., Kägi, R., Halbeisen, M. & Boller, M. Influence of interactions between NOM and particles on UF fouling mechanisms. *Water Res.* **42,** 3870–3878 (2008).

84. Jermann, D., Pronk, W. & Boller, M. Mutual Influences between Natural Organic Matter and Inorganic Particles and Their Combined Effect on Ultrafiltration Membrane Fouling. *Environ. Sci. Technol.* **42,** 9129–9136 (2008).

85. Li, Q. & Elimelech, M. Synergistic effects in combined fouling of a loose nanofiltration membrane by colloidal materials and natural organic matter. *J. Membr. Sci.* **278,** 72–82 (2006).

86. Porter, M. C. Concentration polarization with membrane ultrafiltration. *Ind. Eng. Chem. Prod. Res. Dev.* **11,** 234–248 (1972).

87. Jermann, D., Pronk, W., Meylan, S. & Boller, M. Interplay of different NOM fouling mechanisms during ultrafiltration for drinking water production. *Water Res.* **41,** 1713–1722 (2007).

88. Ahn, W.-Y., Kalinichev, A. G. & Clark, M. M. Effects of background cations on the fouling of polyethersulfone membranes by natural organic matter: Experimental and molecular modeling study. *J. Membr. Sci.* **309,** 128–140 (2008).

89. Schäfer, A. I., Schwicker, U., Fischer, M. M., Fane, A. G. & Waite, T. D. Microfiltration of colloids and natural organic matter. *J. Membr. Sci.* **171,** 151–172 (2000).

90. Li, Q. & Elimelech, M. Organic Fouling and Chemical Cleaning of Nanofiltration Membranes: Measurements and Mechanisms. *Environ. Sci. Technol.* **38,** 4683–4693 (2004).

91. Ahmad, A. L., Abdulkarim, A. A., Ooi, B. S. & Ismail, S. Recent development in additives modifications of polyethersulfone membrane for flux enhancement. *Chem. Eng. J.* **223,** 246–267 (2013).

92. Nady, N. *et al.* Modification methods for poly(arylsulfone) membranes: A mini-review focusing on surface modification. *Desalination* **275,** 1–9 (2011).

93. Rana, D. & Matsuura, T. Surface Modifications for Antifouling Membranes. *Chem. Rev.* **110,** 2448–2471 (2010).

94. Hilal, N., Ogunbiyi, O. O., Miles, N. J. & Nigmatullin, R. Methods Employed for Control of Fouling in MF and UF Membranes: A Comprehensive Review. *Sep. Sci. Technol.* **40,** 1957–2005 (2005).

95. Zhao, C., Xue, J., Ran, F. & Sun, S. Modification of polyethersulfone membranes – A review of methods. *Prog. Mater. Sci.* **58,** 76–150 (2013).

96. Nabe, A. Surface modification of polysulfone ultrafiltration membranes and fouling by BSA solutions. *J. Membr. Sci.* **133,** 57–72 (1997).

97. Wienk, I. M. *et al.* Recent advances in the formation of phase inversion membranes made from amorphous or semi-crystalline polymers. *J. Membr. Sci.* **113,** 361–371 (1996).

98. Jung, B., Yoon, J. K., Kim, B. & Rhee, H.-W. Effect of molecular weight of polymeric additives on formation, permeation properties and hypochlorite treatment of asymmetric polyacrylonitrile membranes. *J. Membr. Sci.* **243,** 45–57 (2004).

99. Jung, B. Preparation of hydrophilic polyacrylonitrile blend membranes for ultrafiltration. *J. Membr. Sci.* **229,** 129–136 (2004).

100. Marchese, J. *et al.* Fouling behaviour of polyethersulfone UF membranes made with different PVP. *J. Membr. Sci.* **211,** 1–11 (2003).

101. Qin, J.-J. & Wong, F.-S. Hypochlorite treatment of hydrophilic hollow fiber ultrafiltration membranes for high fluxes. *Desalination* **146,** 307–309 (2002).

102. Wienk, I. M., Meuleman, E. E. B., Borneman, Z., Van Den Boomgaard, T. & Smolders, C. A. Chemical treatment of membranes of a polymer blend: mechanism of the reaction of hypochlorite with poly (vinyl pyrrolidone). *J. Polym. Sci. Part Polym. Chem.* **33,** 49–54 (1995).

103. Bolto, B., Tran, T., Hoang, M. & Xie, Z. Crosslinked poly(vinyl alcohol) membranes. *Prog. Polym. Sci.* **34,** 969–981 (2009).

104. Ma, X., Su, Y., Sun, Q., Wang, Y. & Jiang, Z. Enhancing the antifouling property of polyethersulfone ultrafiltration membranes through surface adsorption-crosslinking of poly(vinyl alcohol). *J. Membr. Sci.* **300,** 71–78 (2007).

105. Li, R. H. & Barbari, T. A. Performance of poly(vinyl alcohol) thin-gel composite ultrafiltration membranes. *J. Membr. Sci.* **105,** 71–78 (1995).

106. Mueller, J. Protein fouling of surface-modified polymeric microfiltration membranes. *J. Membr. Sci.* **116,** 47–60 (1996).

107. Du, J. R., Peldszus, S., Huck, P. M. & Feng, X. Modification of poly(vinylidene fluoride) ultrafiltration membranes with poly(vinyl alcohol) for fouling control in drinking water treatment. *Water Res.* **43,** 4559–4568 (2009).

108. Wang, X., Fang, D., Yoon, K., Hsiao, B. S. & Chu, B. High performance ultrafiltration composite membranes based on poly(vinyl alcohol) hydrogel coating on crosslinked nanofibrous poly(vinyl alcohol) scaffold. *J. Membr. Sci.* **278,** 261–268 (2006).

109. Zhang, Y., Li, H., Li, H., Li, R. & Xiao, C. Preparation and characterization of modified polyvinyl alcohol ultrafiltration membranes. *Desalination* **192,** 214–223 (2006).

110. Zhang, Y., Zhu, P. C. & Edgren, D. Crosslinking reaction of poly(vinyl alcohol) with glyoxal. *J. Polym. Res.* **17,** 725–730 (2010).

111. Tang, C. Y., Kwon, Y.-N. & Leckie, J. O. Effect of membrane chemistry and coating layer on physiochemical properties of thin film composite polyamide RO and NF membranes: I. FTIR and XPS characterization of polyamide and coating layer chemistry. *Desalination* **242,** 149–167 (2009).

112. Tang, C. Y., Kwon, Y.-N. & Leckie, J. O. Effect of membrane chemistry and coating layer on physiochemical properties of thin film composite polyamide RO and NF membranes: II. Membrane physiochemical properties and their dependence on polyamide and coating layers. *Desalination* **242,** 168–182 (2009).

113. Tang, C., Kwon, Y. & Leckie, J. Probing the nano- and micro-scales of reverse osmosis membranes—A comprehensive characterization of physiochemical properties of uncoated and coated membranes by XPS, TEM, ATR-FTIR, and streaming potential measurements. *J. Membr. Sci.* **287,** 146–156 (2007).

114. Beckett, R. & Le, N. P. The role or organic matter and ionic composition in determining the surface charge of suspended particles in natural waters. *Colloids Surf.* **44,** 35–49 (1990).

115. Hong, S. & Elimelech, M. Chemical and physical aspects of natural organic matter (NOM) fouling of nanofiltration membranes. *J. Membr. Sci.* **132,** 159–181 (1997).

116. Susanto, H., Arafat, H., Janssen, E. M. L. & Ulbricht, M. Ultrafiltration of polysaccharide–protein mixtures: Elucidation of fouling mechanisms and fouling control by membrane surface modification. *Sep. Purif. Technol.* **63,** 558–565 (2008).

117. Park, J.-S. *et al.* Fouling mitigation of anion exchange membrane by zeta potential control. *J. Colloid Interface Sci.* **259,** 293–300 (2003).

118. Nakao, S., Osada, H., Kurata, H., Tsuru, T. & Kimura, S. Separation of proteins by charged ultrafiltration membranes. *Desalination* **70,** 191–205 (1988).

119. Higuchi, A., Iwata, N., Tsubaki, M. & Nakagawa, T. Surface-modified polysulfone hollow fibers. *J. Appl. Polym. Sci.* **36,** 1753–1767 (1988).

120. Higuchi, A., Iwata, N. & Nakagawa, T. Surface-modified polysulfone hollow fibers. II. Fibers having CH2CH2CH2SO3- segments and immersed in HCI solution. *J. Appl. Polym. Sci.* **40,** 709–717 (1990).

121. Higuchi, A. & Nakagawa, T. Surface modified polysulfone hollow fibers. III. Fibers having a hydroxide group. *J. Appl. Polym. Sci.* **41,** 1973–1979 (1990).

122. Ulbricht, M., Richau, K. & Kamusewitz, H. Chemically and morphologically defined ultrafiltration membrane surfaces prepared by heterogeneous photo-initiated graft polymerization. *Colloids Surf. Physicochem. Eng. Asp.* **138,** 353–366 (1998).

123. Knoell, T. *et al.* Biofouling potentials of microporous polysulfone membranes containing a sulfonated polyether-ethersulfone/polyethersulfone block copolymer: correlation of membrane surface properties with bacterial attachment. *J. Membr. Sci.* **157,** 117–138 (1999).

124. Lin, S. W. & Espinoza-Gomez, H. Development of energy-saving spinning membrane systemand negatively charged ultrafiltration membranes for recovering oil from waste machine cutting fluid. *Desalination* **174,** 109–123 (2005).

125. Kobayashi, T., Miyamoto, T., Nagai, T. & Fujii, N. Polyacrylonitrile ultrafiltration membranes containing negatively charged groups for permeation and separation of dextran and dextransulfate. *J. Appl. Polym. Sci.* **52,** 1519–1528 (1994).

126. Tang, B., Xu, T., Gong, M. & Yang, W. A novel positively charged asymmetry membranes from poly(2,6-dimethyl-1,4-phenylene oxide) by benzyl bromination and in situ amination: membrane preparation and characterization. *J. Membr. Sci.* **248,** 119–125 (2005).

127. Wakeman, R. J. & Tarleton, E. S. Membrane fouling prevention in crossflow microfiltration by the use of electric fields. *Chem. Eng. Sci.* **42,** 829–842 (1987).

128. Jagannadh, S. N. & Muralidhara, H. S. Electrokinetics methods to control membrane fouling. *Ind. Eng. Chem. Res.* **35,** 1133–1140 (1996).

129. Moulik, S. P. Physical aspects of electrofiltration. *Environ. Sci. Technol.* **5,** 771–776 (1971).

130. Henry, J. D., Lawler, L. F. & Kuo, C. H. A solid/liquid separation process based on cross flow and electrofiltration. *AIChE J.* **23,** 851–859 (1977).

131. Tarleton, E. S. & Wakeman, R. J. Prevention of flux decline in electrical microfiltration. *Dry. Technol.* **6,** 547–570 (1988).

132. Akamatsu, K., Lu, W., Sugawara, T. & Nakao, S. Development of a novel fouling suppression system in membrane bioreactors using an intermittent electric field. *Water Res.* **44,** 825–830 (2010).

133. Liu, L., Liu, J., Gao, B. & Yang, F. Minute electric field reduced membrane fouling and improved performance of membrane bioreactor. *Sep. Purif. Technol.* **86,** 106–112 (2012).

134. Sarkar, B., De, S. & DasGupta, S. Pulsed electric field enhanced ultrafiltration of synthetic and fruit juice. *Sep. Purif. Technol.* **63,** 582–591 (2008).

135. Sarkar, B., DasGupta, S. & De, S. Effect of electric field during gel-layer controlled ultrafiltration of synthetic and fruit juice. *J. Membr. Sci.* **307,** 268–276 (2008).

136. Hofmann, R., Käppler, T. & Posten, C. Pilot-scale press electrofiltration of biopolymers. *Sep. Purif. Technol.* **51,** 303–309 (2006).

137. Weigert, T., Altmann, J. & Ripperger, S. Crossflow electrofiltration in pilot scale. *J. Membr. Sci.* **159,** 253–262 (1999).

138. Kilpatrick, P. K. Water-in-Crude Oil Emulsion Stabilization: Review and Unanswered Questions. *Energy Fuels* **26,** 4017–4026 (2012).

139. Ushikubo, F. Y. & Cunha, R. L. Stability mechanisms of liquid water-in-oil emulsions. *Food Hydrocoll.* **34,** 145–153 (2014).

140. *Produced Water*. (Springer New York, 2011).

141. Fakhru'l-Razi, A. *et al.* Review of technologies for oil and gas produced water treatment. *J. Hazard. Mater.* **170,** 530–551 (2009).

142. Ghaffour, N. Modeling of fouling phenomena in cross-flow ultrafiltration of suspensions containing suspended solids and oil droplets. *Desalination* **167,** 281–291 (2004).

143. Jung, Y. C. & Bhushan, B. Wetting Behavior of Water and Oil Droplets in Three-Phase Interfaces for Hydrophobicity/philicity and Oleophobicity/philicity †. *Langmuir* **25,** 14165–14173 (2009).

144. Kalin, M. & Polajnar, M. The correlation between the surface energy, the contact angle and the spreading parameter, and their relevance for the wetting behaviour of DLC with lubricating oils. *Tribol. Int.* **66,** 225–233 (2013).

145. Lipp, P., Lee, C. H., Fane, A. G. & Fell, C. J. D. A fundamental study of the ultrafiltration of oil-water emulsions. *J. Membr. Sci.* **36,** 161–177 (1988).

146. Tummons, E. N., Tarabara, V. V., Chew, J. W. & Fane, A. G. Behavior of oil droplets at the membrane surface during crossflow microfiltration of oil–water emulsions. *J. Membr. Sci.* **500,** 211–224 (2016).

147. Ochoa, N. Effect of hydrophilicity on fouling of an emulsified oil wastewater with PVDF/PMMA membranes. *J. Membr. Sci.* **226,** 203–211 (2003).

148. Masuelli, M., Marchese, J. & Ochoa, N. A. SPC/PVDF membranes for emulsified oily wastewater treatment. *J. Membr. Sci.* **326,** 688–693 (2009).

149. Chen, W. *et al.* Engineering a Robust, Versatile Amphiphilic Membrane Surface Through Forced Surface Segregation for Ultralow Flux-Decline. *Adv. Funct. Mater.* **21,** 191–198 (2011).

150. Zhao, X., Su, Y., Chen, W., Peng, J. & Jiang, Z. Grafting perfluoroalkyl groups onto polyacrylonitrile membrane surface for improved fouling release property. *J. Membr. Sci.* **415–416,** 824–834 (2012).

151. Zhu, Y. *et al.* A novel zwitterionic polyelectrolyte grafted PVDF membrane for thoroughly separating oil from water with ultrahigh efficiency. *J. Mater. Chem. A* **1,** 5758 (2013).

152. Zhang, J. & Seeger, S. Polyester Materials with Superwetting Silicone Nanofilaments for Oil/Water Separation and Selective Oil Absorption. *Adv. Funct. Mater.* **21,** 4699–4704 (2011).

153. Liu, N. *et al.* Straightforward Oxidation of a Copper Substrate Produces an Underwater Superoleophobic Mesh for Oil/Water Separation. *ChemPhysChem* **14,** 3489–3494 (2013).

154. Xue, Z. *et al.* A Novel Superhydrophilic and Underwater Superoleophobic Hydrogel-Coated Mesh for Oil/Water Separation. *Adv. Mater.* **23,** 4270–4273 (2011).

155. Zhang, F. *et al.* Nanowire-Haired Inorganic Membranes with Superhydrophilicity and Underwater Ultralow Adhesive Superoleophobicity for High-Efficiency Oil/Water Separation. *Adv. Mater.* **25,** 4192–4198 (2013).

156. Zhang, L., Zhong, Y., Cha, D. & Wang, P. A self-cleaning underwater superoleophobic mesh for oil-water separation. *Sci. Rep.* **3,** (2013).

157. Ejaz Ahmed, F., Lalia, B. S., Hilal, N. & Hashaikeh, R. Underwater superoleophobic cellulose/electrospun PVDF–HFP membranes for efficient oil/water separation. *Desalination* **344,** 48–54 (2014).

158. Zhang, W. *et al.* Superhydrophobic and Superoleophilic PVDF Membranes for Effective Separation of Water-in-Oil Emulsions with High Flux. *Adv. Mater.* **25,** 2071–2076 (2013).

159. Levine, S., Bowen, B. D. & Partridge, S. J. Stabilization of emulsions by fine particles I. Partitioning of particles between continuous phase and oil/water interface. *Colloids Surf.* **38,** 325–343 (1989).

160. Saleh, N. *et al.* Oil-in-water emulsions stabilized by highly charged polyelectrolyte-grafted silica nanoparticles. *Langmuir* **21,** 9873–9878 (2005).

161. Saleh, N. *et al.* Adsorbed Triblock Copolymers Deliver Reactive Iron Nanoparticles to the Oil/Water Interface. *Nano Lett.* **5,** 2489–2494 (2005).

162. Zhou, J. *et al.* Magnetic Pickering Emulsions Stabilized by Fe_3O_4 Nanoparticles. *Langmuir* **27,** 3308–3316 (2011).

163. Kaiser, A., Liu, T., Richtering, W. & Schmidt, A. M. Magnetic Capsules and Pickering Emulsions Stabilized by Core−Shell Particles. *Langmuir* **25,** 7335–7341 (2009).

164. Sacanna, S., Kegel, W. K. & Philipse, A. P. Thermodynamically Stable Pickering Emulsions. *Phys. Rev. Lett.* **98,** (2007).

165. San-Miguel, A. & Behrens, S. H. Influence of Nanoscale Particle Roughness on the Stability of Pickering Emulsions. *Langmuir* **28,** 12038–12043 (2012).

166. Melle, S., Lask, M. & Fuller, G. G. Pickering Emulsions with Controllable Stability. *Langmuir* **21,** 2158–2162 (2005).

167. Wang, H. *et al.* Removal of oil droplets from contaminated water using magnetic carbon nanotubes. *Water Res.* **47,** 4198–4205 (2013).

168. Elimelech, M. & Phillip, W. A. The future of seawater desalination: energy, technology, and the environment. *science* **333,** 712–717 (2011).

169. Fritzmann, C., Löwenberg, J., Wintgens, T. & Melin, T. State-of-the-art of reverse osmosis desalination. *Desalination* **216,** 1–76 (2007).

170. Alkhudhiri, A., Darwish, N. & Hilal, N. Membrane distillation: A comprehensive review. *Desalination* **287,** 2–18 (2012).

171. Kullab, A. & Martin, A. Membrane distillation and applications for water purification in thermal cogeneration plants. *Sep. Purif. Technol.* **76,** 231–237 (2011).

172. Gryta, M. Fouling in direct contact membrane distillation process. *J. Membr. Sci.* **325,** 383–394 (2008).

173. Gryta, M. Long-term performance of membrane distillation process. *J. Membr. Sci.* **265,** 153–159 (2005).

174. Lin, S., Yip, N. Y. & Elimelech, M. Direct contact membrane distillation with heat recovery: Thermodynamic insights from module scale modeling. *J. Membr. Sci.* **453,** 498–515 (2014).

175. Mundhenk, N., Huttenloch, P., Kohl, T., Steger, H. & Zorn, R. Metal corrosion in geothermal brine environments of the Upper Rhine graben – Laboratory and on-site studies. *Geothermics* **46,** 14–21 (2013).

176. He, F., Gilron, J. & Sirkar, K. K. High water recovery in direct contact membrane distillation using a series of cascades. *Desalination* **323,** 48–54 (2013).

177. Liu, H., Vajpayee, A. & Vecitis, C. D. Bismuth-Doped Tin Oxide-Coated Carbon Nanotube Network: Improved Anode Stability and Efficiency for Flow-Through Organic Electrooxidation. *ACS Appl. Mater. Interfaces* **5,** 10054–10066 (2013).

178. Duan, W., Ronen, A., Walker, S. & Jassby, D. Polyaniline-Coated Carbon Nanotube Ultrafiltration Membranes: Enhanced Anodic Stability for *In Situ* Cleaning and Electro-Oxidation Processes. *ACS Appl. Mater. Interfaces* (2016). doi:10.1021/acsami.6b07196

Chapter 2 Organic Fouling Inhibition on Electrically Conducting Carbon Nanotube – Polyvinyl Alcohol Composite Ultrafiltration Membranes

2.1 Summary

Robust and electrically conductive thin films (2500 S/m) made of cross-linked poly(vinyl alcohol) and carboxylated multi-walled carbon nanotubes (PVA-CNT-COOH) were synthesized via a sequential deposition and cross-linking method. The PVA-CNT-COOH modified membranes were then used in an electrofiltration cell in which the effects of applied potentials on fouling of high concentrations (3-5 g/L) of alginic acid (AA) were studied. It was demonstrated that after 100 minutes of operation while applying -3 V and -5 V, the change in operating pressure was reduced by 33% and 51%, respectively, compared to application of no voltage. Increase in ionic strength resulted in overall higher fouling rates, where the application of -5 V resulted in a pressure change reduction of 43% compared to no application of potential. A modified Poisson-Boltzmann equation used in a DLVO-type theory demonstrated that at the applied potentials, electrostatic interactions produced significant repulsive forces between the membrane surface and the charged organic foulant. Calculations at experimental conditions demonstrated the pure AA aggregates would be strongly repulsed away from membrane surface. In synthetic wastewater the repulsion force is greatly reduced, resulting in overall reduced fouling inhibition.

2.2 Introduction

Ultrafiltration (UF) membrane technologies are commonly used in water treatment and reclamation due to their high permeate flux at low transmembrane pressures, tunable rejection properties and compact size. [1,2] However, UF membranes suffer from fouling,

where organic and inorganic materials deposit on the membrane surface, blocking the passage of water. UF fouling is a complex process that occurs by three distinct processes. [3,4] In *pore constriction*, fouling agents that can pass through the membrane adsorb onto the pore walls, reducing their inner diameter and increasing hydraulic resistance to flow; in *pore blocking*, pores get physically blocked at the membrane surface; in *cake layer formation* a fouling layer made up of macromolecules and colloids forms a dense viscous gel layer on the surface of the membrane, drastically increasing hydraulic resistance. Many studies have investigated how solution conditions, membrane properties and flow conditions affect the different mechanisms of membrane fouling.[5–11] Typically, membranes with rough surfaces, high hydrophobicity and large pore sizes suffer from high permeate loss and a high degree of irreversible fouling during water treatment processes.[4,12,13] To mitigate fouling in UF systems, high cross flow velocities, air scouring across the membrane surface, and membrane surface modifications, such as polymer and nanoparticle grafting, have been used to combat fouling. However these strategies suffer from several disadvantages, including high energy demands and low durability [12,14–18]

Fouling agents such as polysaccharides, commonly found in water, have a negative charge, making them susceptible to electrostatic repulsion by a negatively charged membrane surface; increased electrostatic repulsion between the membrane and the fouling agent can reduce both pore blocking and surface gel formation. [19–23] Modification of UF membrane surfaces through polymer grafting has been used to adjust their surface charge and hydrophobicity with observed reduction in fouling rates. [24,25] An alternative method to enhance the surface charge of the membrane is the use of an applied electrical field, a

process called electrofiltration. Previous attempts at electrofiltration used an electrical field applied perpendicularly to the membrane surface by placing electrodes on the permeate and retentate sides of the membrane, imparting an electrophoretic force on charged molecules and colloids. (Figure 2.1A) [26] The application of large direct current (DC) fields has been shown to effectively reduce fouling rates and increase permeate flux rates in both cross-flow filtration and dead end filtration systems. [26–33] However, these electrofiltration systems suffer from high inefficiencies due to the placement of the electrodes on opposite sides of the membrane, which acts as an insulator that drastically reduces the effect of the electric field; this leads to high energy demands and undesirable Faradaic reactions as the required electrical potential needed to impact fouling rates is greatly increased, with potentials ranging from several volts to several hundred volts. [29,33,34] A recent excellent study demonstrated the application of a poorly conducting carbon nanotube (CNT) – polyvinylidene fluoride mesh, which was placed over a UF membrane and operated as a cathode, in fouling mitigation from low concentrations of organic molecules; the study demonstrates that electrostatic forces are primarily responsible for the reduction in fouling when the mesh was electrically charged.[34]

An electrically conducting membrane could substantially increase the efficiency of electrofiltration, producing a tunable charged membrane surface, which could repulse charged particles and enhance fouling resistance. (Figure 2.1B) Conductive polymers have been used to prepare and coat UF membranes, but require exotic reaction designs, suffer from brittleness, low flux, roughness and poor separation performance. [35–39] Conductive inorganic membranes have also been explored for electrofiltration of oily waters, organic

molecules, yeast and titanium dioxide with promising results. However, these membrane materials are expensive, difficult to produce, and impossible to package into the high surface area modules necessary in membrane filtration. [40–43] Thus, to develop an effective electrofiltration membrane for water treatment, a cheap, flexible and scalable technology is necessary.

Recent developments have drastically reduced the cost of carbon nanotubes (CNTs), making it possible to develop affordable, permeable conductive thin films out of functionalized multiwall CNTs, and poly(vinyl alcohol) (PVA).[44] Herein, we demonstrate how to prepare robust conductive CNT-PVA UF membranes and demonstrate their usefulness in fouling inhibition of extremely high concentrations of alginic acid (AA) when charged with different electric potentials. AA is used as a negatively charged model fouling agent in this study, as it was determined that polysaccharides are the primary fouling agent in natural waters; polyethylene oxide (PEO) is used as a neutrally charged fouling agent. [5,23,45] We demonstrate that at moderate applied cell potentials (3-5 V) and fields (9-15 V/cm), UF membrane fouling by AA can be greatly reduced, as well as demonstrate through a theoretical model that at those potentials, high electrostatic forces are imparted onto AA particles, explaining the observed fouling inhibition.

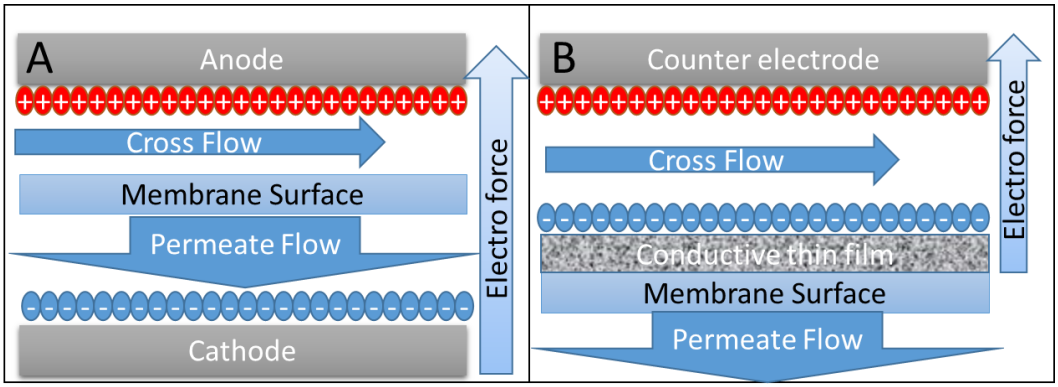

Figure 2.1: A) Classical electrofiltration cell setup. B) Electrofiltration with conducive membrane/thin film set up.

2.3 Experimental

2.3.1 Materials

50wt% Glutaraldehyde solution was purchased from Fisher Scientific and used as received. 146,000-186,000 MW Poly(vinyl alcohol), Dodecylbenzenesulfonic acid (DDBS), 120-190kDA Sodium Alginate, 200kDa poly(ethylene) oxide, sodium citrate, ammonium chloride, Sodium Perchlorate, KH_2PO_4, $CaCl_2 \cdot 2H_2O$, $NaHCO_3$, NaCl, and $MgSO_4 \cdot 7H_2O$ were purchased from Sigma Aldrich and used as received. PS-35 Polysulfone Ultrafiltration membranes were purchased from Sepro (Sepro Membranes Inc., Oceanside, CA). Multi-Wall Carbon Nanotubes functionalized with Carboxylic groups via Plasma treatment (CNT-COOH) were purchased from CheapTubes (Cheaptubes Inc., Brattleboro, VT), and had reported outer diameter of 13-18nm, length of 3-30 μm and purity of >99 wt%, with a functional group content of 7.0%.

2.3.2 Synthesis

CNT-COOH powder was suspended in deionized (DI) water at 0.01 wt% concentration with 1:10 ratio of CNT-COOH:DDBS, by sonication with a horn sonicator (Branson; Danbury, CT). 1 wt% PVA in DI water was dissolved at 95-100 °C with stirring for 1 hr. A 3:1 ratio of PVA-CNT-COOH (w/w) solution was pressure deposited (Millipore; Billerica, MA) onto a PS-35 membrane support with CNT-COOH concentration of 0.57 g/m^2. The prepared membranes were then immersed into a crosslinking solution consisting of 1 g/L of glutaraldehyde (cross linker) and 0.37 g/L of hydrochloric acid (catalyst) and heated at 80 °C for 4 hrs. Membranes were removed from the heated bath and dried at 80 °C for 5 min, after which they were cooled to room temperature, and used without further modification.

2.3.3 Thinfilm Characterization

Membrane surfaces were imaged using scanning electron microscopy (SEM; FEI XL30 SEM-FEG; Hillsboro,OR) with no further modifications. Cross sectional samples were frozen in water at -80 °C and fractured, after which they were affixed onto SEM stubs with copper tape, sputter coated with Pd/Pt, before being imaged with SEM. Contact angle measurements were performed with a goniometer (Attension; Linthicum Heights, MD) using deionized water. Attenuated total reflectance Fourier transform infrared spectroscopy (ATR-FTIR; Thermo Scientific; Waltham,MA) was performed on membranes without modification on non-reacted PVA-CNT-COOH membranes, CNT-COOH only coated membranes, and CNT-COOH reacted with GA membranes. Membrane conductivity was

measured with a four-point conductivity probe (Veeco; Plainview, NY) in sheet resistance mode, with the membrane soaked for 24 hours in DI water before measurement.

2.3.4 Fouling System Design

A fully automated cross flow filtration system was developed for studying the effect of electrofiltration on membrane fouling. The system was operated at a constant flux of 20±2 L/m^2 hr (LMH), with fluxes maintained using a PID cascade loop, which adjusted transmembrane pressure to correct for membrane fouling. The system is capable of performing membrane cleaning cycles, maintain bulk solution volume to ±100ml, measure current draw, check membrane resistance using a digital volt meter (BK5491B; BK Precision; Yorba Linda, CA), collect samples from the permeate tank and change the electrical conditions applied to the membrane surface using an arbitrary waveform generator (DG1022;Rigol; Oakwood Village, OH). (Figure 4) A custom flow cell was made of acetal with channel dimensions of 3.25 mm high, 40 mm wide, and 100 mm long; a 316 stainless steel sheet was used as the counter electrode. A gear pump (Coleparmer; Vernon Hills, IL) was used to provide flow and transmembrane pressure, and a peristaltic pump was used for membrane cleaning (Coleparmer; Vernon Hills, IL).

2.3.5 Fouling Experiment Procedure

Transmembrane pressure was used as the fouling indicator, and all experiments were performed at 0.1 m/s cross flow velocity, which corresponds to a Reynolds number of 620. All membranes were compressed at 100 PSI for 17-20 hrs at -3 V for the first 10 hours, and completed at -5 V, with 5 minute back flushes performed every 1 hour to ensure membrane was fully compressed (back flush pressure maintained at 5 PSI). Fouling

experiments were performed in cycles, each cycle consisting of four runs, where each run terminated after two hours, with a 10 minute back flush cleaning performed between each run. Backflusing was performed with membrane permeate, with no additional cleaning agents. During all voltage cycles, power was switched on at start of run, and would be turned off during back flushing. To ensure that membranes were not permanently altered during voltage experiment, a 0 V (no application of voltage) cycle would run in between each voltage, unless noted. At the end of the third and fourth run in each cycle, a 15 ml sample was collected from the permeate tank to measure rejection using a total organic carbon analyzer (TOC; OI Analytical, College Station, TX). In all figures, a moving average of pressure measurements (over 180 seconds) is plotted with standard deviations, unless noted.

2.3.6 Fouling Experiment Solutions

Three fouling solutions were studied: 5 g/L AA in DIW, synthetic wastewater with 3 g/L alginic acid (SW-AA) and 250 mg/L 200 kDa PEO in DIW. Synthetic wastewater was prepared by mixing 1.16 mM sodium citrate, 0.94 mM ammonium chloride, 0.45 mM KH_2PO_4, 0.5 mM $CaCl_2 \cdot 2H_2O$, 0.5 mM $NaHCO_3$, 2.0 mM NaCl, and 0.6 mM $MgSO_4 \cdot 7H_2O$.[46] In all experiments, 4 L of bulk solution were used, to minimize bulk concentration variation. Zeta potential of the solutions was measured using ZetaPALS (Brookhaven Instruments; Holtsville, NY) on as prepared solutions. The pH of all solutions was measured with a digital pH meter (Thermo Scientific; Waltham,MA) and remained at pH of 6.7±0.3 throughout all fouling experiments. The average hydrodynamic diameter of the fouling agents was measured using dynamic light scattering (DLS; Brookhaven

Instruments; Holtsville, NY); bulk solutions were diluted to 10-100 ppm concentration, with each sample measured five times, at a 90° scattering angle. Electrochemical properties of solution and membrane were quantified with CH Instruments (Austin, TX) potentiostat.

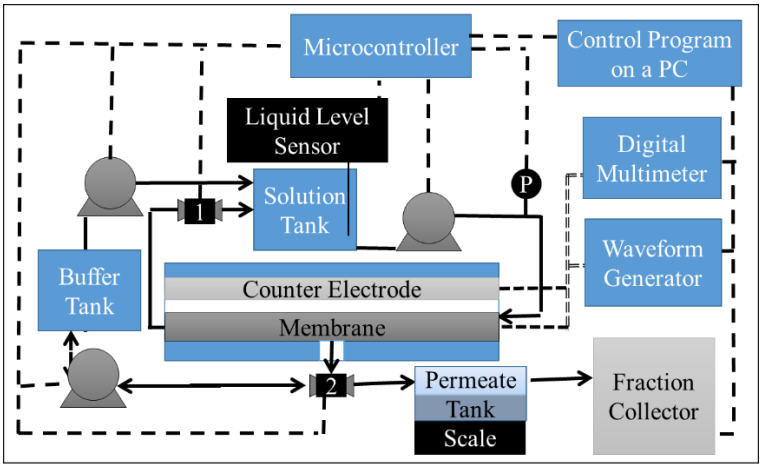

Figure 2.2: Experimental cross flow filtration system flow diagram, solid lines represent piping, dashed lines represent digital or power lines.

2.4 Results and Discussion

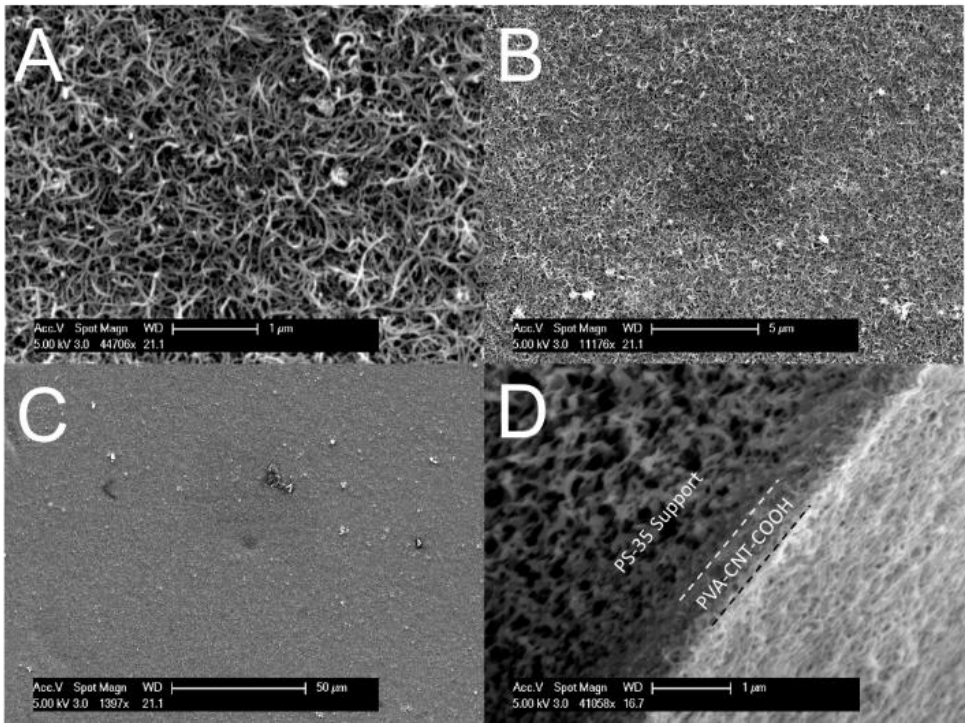

Figure 2.3: A-C) Top view of thin films. D) Cross sectional views of PVA-CNT thin film. (Scale bars 1 μm, 5 μm, 50 μm and 1 μm respectively)

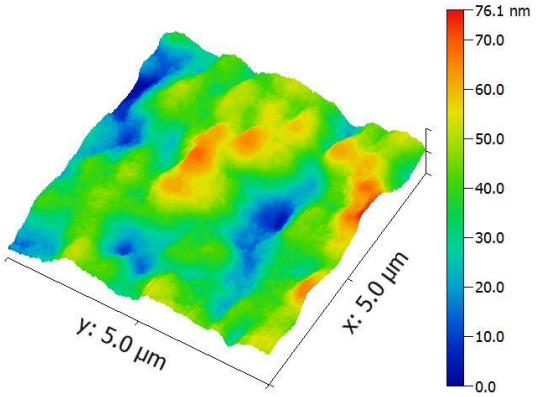

Figure 2.4: Surface of PVA-CNT thin film (Scan area 5.0 μm by 5.0 μm)

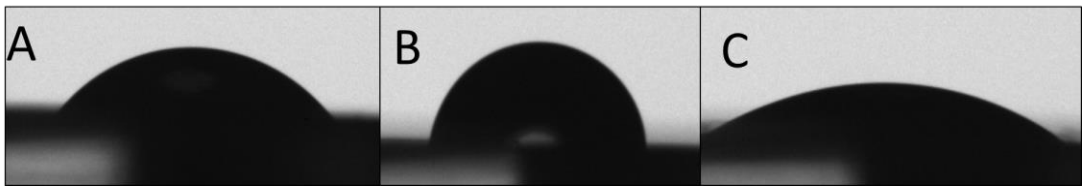

Figure 2.5: Contact Angle images: A) PS-35 with contact angle of 49.2±0.9°, B) PS-35 coated with CNT-COOH with contact angle of 81.6±3.2°, C) PS-35 coated with PVA-CNT-COOH with contact angle of 32.0.±2.8°

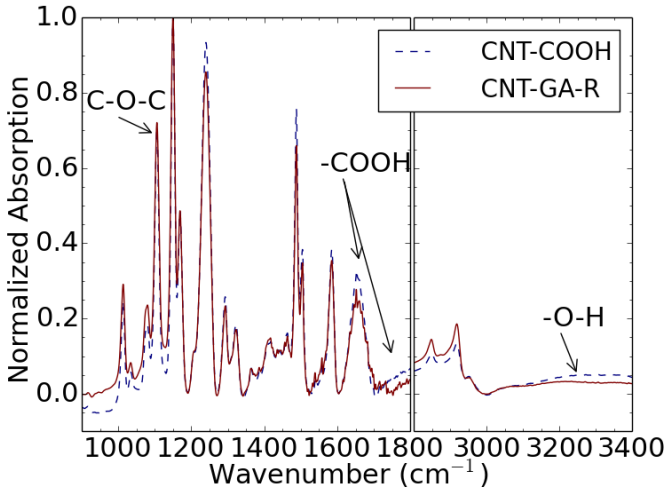

Figure 2.6 ATR-FTIR for CNT-COOH thinfilm and CNT-COOH thinfilm reacted with GA. (CNT-GA-R)

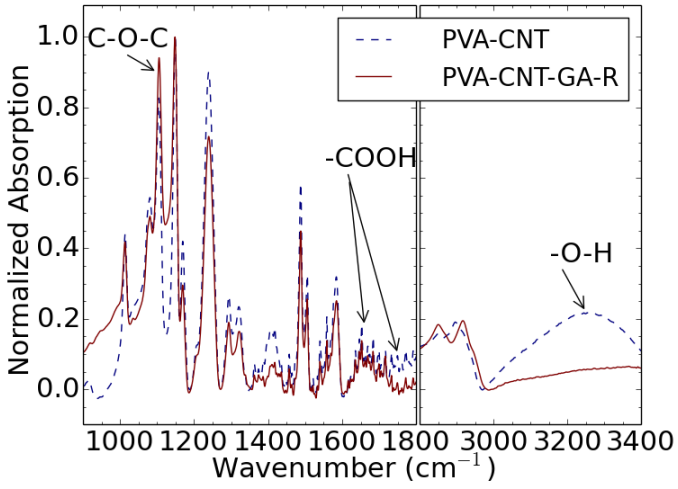

Figure 2.7:ATR-FTIR for non reacted PVA CNT-COOH thinfilm and PVA CNT-COOH thinfilm reacted with GA (PVA-CNT-GA-R)

2.4.1 PVA-CNT-COOH UF Membrane Characterization.

Conductive thin films made of PVA and CNT-COOH produced very smooth and robust surfaces, with a highly porous percolating network of CNT-COOH (Figure 2.3 A-C). The roughness of the PVA-CNT network was analyzed using AFM, with an overall mean squared roughness, based on four 2.5 μm by 2.5 μm segments, being 12.25±2.27 nm (Figure 2.4), which is in agreement with reported roughness values of CNT based thin films.[47–49] The PVA provides a matrix that links the CNTs, holding them together through the covalent bonding of hydroxyl groups on PVA molecules and carboxyl groups on the CNT-COOH, created by the cross-linker GA. To verify the reaction of the cross-linking agent GA, membrane surfaces were analyzed using ATR-FTIR. When GA reacts with hydroxyl or carboxyl groups, a C-O-C bond is formed, which manifests as a decrease in the absorption wavenumbers associated with O-H groups.[50] This decrease was observed when analyzing the cross-linked PVA-COOH membrane (a decrease in absorption at 3200-3400 cm^{-1}) (Figure 2.7) Additionally, the formation of C-O-C bonds in the crosslinked CNT network was observed as an increase in at 1085-1150 cm^{-1} (Figures 2.6-2.7). [51–53] To verify that GA forms links with CNT functional groups, the ATR-FTIR absorption spectrum was measured for a CNT-COOH network that was cross-linked with only GA (no PVA). The peaks at 1660 cm^{-1} and 1750 cm^{-1} are associated with carboxylic groups, and the reduction of absorption at these peaks is associated with the cross-linking of GA with carboxylic groups present on CNT-COOH, indicating the GA is forming ester bonds with the CNT-COOH; in addition, a slight decrease in the absorption associated with O-H groups indicates that some hydroxyls were consumed, which further indicates cross-linking

(Figure 2.6-2.7). [54–56] The crosslinking of the CNT-COOH and PVA results in a covalently bound, robust percolating network, preventing the CNTs from desorbing and entering the retentate or permeate streams. Furthermore, the small pore size of the UF support prevents the passage of the CNTs into the permeate, negating any possibility of CNTs entering the permeate even if the covalent bonding fails.

The overall thickness of the PVA-CNT-COOH layer was determined to be approximately 400 nm as shown in Figure 2D. The PVA-CNT-COOH layer exhibited an electrical conductivity of 2412±97 S/m, attributed to the percolating network of CNT-COOH, and is in-line with previous reports of PVA-CNT-COOH membrane conductivities. [44] However, soaking the membranes in water reduced conductivity to 1693±184 S/m; this reduction in conductivity is most likely due to the presence of PVA, which is known to swell in water. [52] The swelling would cause disruption in the percolating CNT-COOH network, reducing the overall conductivity of the film.

The PVA-CNT-COOH films exhibited a contact angle which was 34% lower compared to the PS-35 support. (32.0.±2.8° vs. 49.2±0.9° respectively, Figure 2.5). This low contact angle is due to the high content of –OH groups on PVA, which makes it highly hydrophilic, even after the GA cross-linking. This decrease in contact angle is unlikely to be due to high porosity of the PVA-CNT-COOH network, as films composed solely of CNT-COOH resulted in 65.6% higher contact angle compared to PS-35 (81.6±3.2° vs. 49.2±0.9° respectively, Figure 2.5). Rejection experiments performed in a stirred dead end cell demonstrated no significant change in rejection of either 35 kDa and 200 kDa PEO, or 50 kDa and 150 kDa PVA with either PS-35 or PVA-CNT membranes. (Figure 2.8) This

is expected, as the amount of PVA in the PVA-CNT-COOH film is very small and is not expected to reduce the overall CNT-COOH network porosity. Furthermore, SEM images indicate that the PVA-CNT-COOH network is riddled with large pores ranging in diameters between 10-100 nm; these pore sizes are significantly larger than the pore sizes in the UF support. Thus, the overall rejection properties of the composite membrane is still governed by the PS-35 support.

For the accurate modeling predictions of AA and SW-AA system, membrane surface potential in each respective solution were measured at applied cell potentials of -3 V and -5 V vs. the Ag/AgCl reference electrode, with the actual surface potential being found to be -1.519 V and -3.412 V, respectively. Cyclic voltammetry was used to determine whether redox reactions were occurring on the surface of the membrane or stainless steel counter electrode using 0.1 g/l AA in 50mM sodium perchlorate supporting electrolyte solution. The cyclic voltammetry was run from 0 to -3.6 V (maximum achieved potential) with membrane used as working electrode, and from 0 to 1.6 V with stainless steel electrode, vs. the Ag/AgCl reference. (Figure 2.9A-B) No peaks that could be associated with AA redox reactions were observed. The increase in current draw from -0.7V to -3.5V and from 1.2V to 1.6V is due to water splitting reactions that are occurring on the membrane and stainless steel electrodes, respectively.

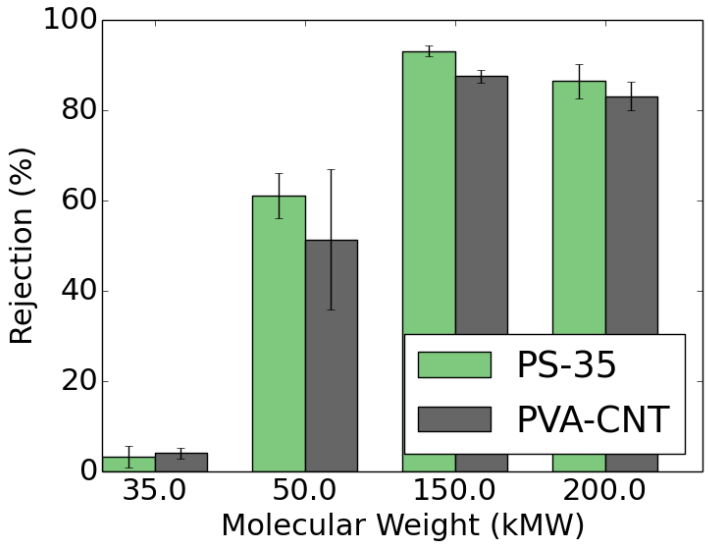

Figure 2.8: Rejection of PVA and PEO for PVA-CNT and PS-35 Membranes.

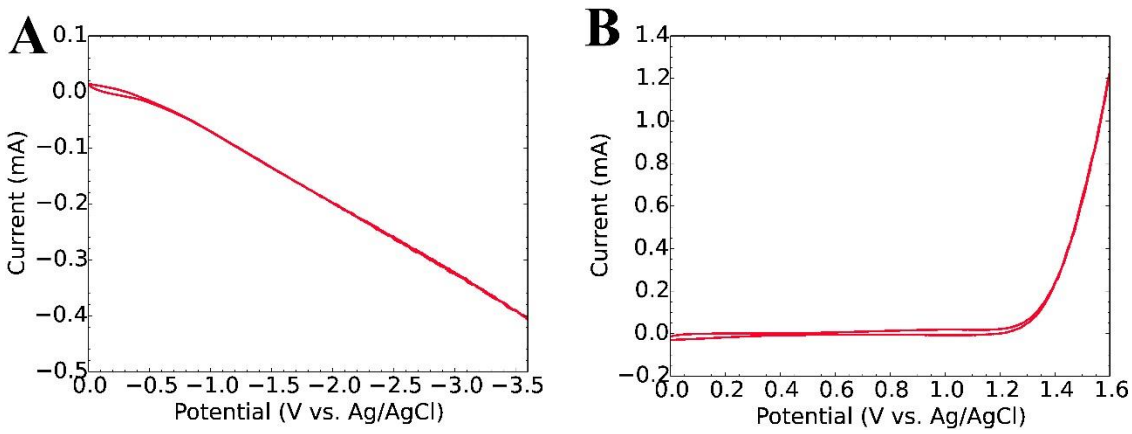

Figure 2.9: Cyclic voltammetry of (A) membrane surface from 0.0 V to -3.5 V vs. the Ag/AgCl reference electrode and (B) stainless steel electrode from 0 V to 1.6 V vs. the Ag/AgCl reference electrode.

2.4.2 Modeling of Electrostatic Forces Acting on a Particle in Electrofiltration

An electrostatic repulsive force arises from the surface potential present on particles and the membrane surface. The standard Poisson-Boltzmann (PB) equation, which is typically used to calculate potential distributions away from a charged surface, and which

forms the basis for the interaction energy calculations employed in the DLVO model, is only valid at low ionic strengths and low surface potentials, and is not appropriate in the current experimental conditions. [57–60] Thus, for the experimental conditions explored in this study, the calculation of potential profiles was performed by employing a Modified Poisson-Boltzmann (MPB) equation (Equation 2.1-2.2).[61] This equation takes into account the finite volume of hydrated ions, as opposed to the standard PB equation that assumes point charges. The MPB equation was solved numerically, where e is the elementary charge, ε is permittivity of solution, N_A is Avogadro's number, k is Boltzmann constant, T is absolute temperature, z_i is valance, and c_i^{∞} is bulk concentration, ρ is ion packing density, R_i is hydrated ionic radius, ψ is potential, and x is distance away from surface. Once the potential distributions away from the surfaces are known, Equation 3 can be used to calculate individual ion concentration after potential profiles are obtained. [59]

$$\frac{d^2\psi}{dx^2} = -\frac{1}{\epsilon}\frac{eN_a\sum_i z_i c_i^{\infty}\exp\left(-\frac{z_i e\psi}{k_b T}\right)}{1+\sum_i \frac{c_i^{\infty}}{c_i^{max}}\left[\exp\left(-\frac{z_i e\psi}{k_b T}\right)-1\right]} \qquad (2.1)$$

$$c_i^{max} = \frac{\rho}{\frac{4}{3}\pi R_i^3 N_a} \qquad (2.2)$$

$$c_i(x) = \frac{c_i^{\infty}\exp\left(-\frac{z_i e\psi(x)}{k_b T}\right)}{1+\sum_i \frac{c_i^{\infty}}{c_i^{max}}\left[\exp\left(-\frac{z_i e\psi(x)}{k_b T}\right)-1\right]} \qquad (2.3)$$

In an attempt to maintain electroneutrality, counter-ions accumulate along the electrically charged surfaces, requiring a certain amount of free energy to move from the bulk solution to the concentrated layer. As two objects are brought together into close

vicinity, the ions between the objects have to be moved out due to spatial constraints. The removal of the counter-ions requires the same amount of free energy it took to accumulate those counter-ions. It is this free energy that is responsible for the increase in electrostatic forces between like-charged particles. In oppositely charged particles, the process is different. The opposite surface potentials will cancel each other out as they are brought closely together, and the counter-ions leave the area between the particles. The loss of the counter-ions, leads to reduced local free energy (same as osmotic pressure) compared to free energy formed by the double layer on the outside of particles, which pushes the particles together. This process also occurs in similar charged particles. If two particles are brought very closely together the concentration of ions between the particles drops below the concentration of ions on the outside of the particles, resulting in lower free energy between particles than on the outside, and the particles will be pushed together.

Modeling of the free energy between two charged objects (such as a particle and plane) begins with the calculation of individual potential profiles away from the plate and particle (Equation 2.1). The profiles are then superimposed, producing a potential profile between two plates. Once the potential profiles are known, ion concentrations as a function of distance from the membrane surface can be calculated using Equations 2.2 and 2.3. Next, the free energy (F) between two parallel plates is calculated through the Gibbs adsorption isotherm. [62] This approach uses a coupling constant integration, where the ion concentration between the parallel plates is brought from zero to the excess ion concentration created by surface potentials (Equation 2.4) where *L* is plate-plate separation. The final free energy is calculated by subtracting the free energy at an infinite plate

separation, from the free energy present between the plates at selected separations (Equation 2.5).[63,64]

$$F(c) = \int_0^c -k_b T N_a \int_0^L \left(\frac{\sum c_i(x)}{c^\infty} - 1\right) dx dc \qquad (2.4)$$

$$F = F(c) - F(c_\infty) \qquad (2.5)$$

The electrostatic force F_{es} acting on a particle can finally be found through the use of the surface elementary integration method (equation 2.6), where $\delta F^e/\delta x$ is the derivative of the Free energy function at a separation distance x, where a is a constant partial radius, and r is the variable radius, over which integration is performed . [65] This method allows for the conversion of the parallel plate assumption to the desired particle-plate interaction. The electrostatic force model presented here produces results for interaction forces that lie within the range of values previously reported in the literature for theoretical calculations, as well as experimental measurements performed by AFM. [63,66–69]

$$F_{es} = 2\pi \int_0^r \left[-\frac{\delta F^e}{\delta x}\left(x + a - a\sqrt{1 - \left(\frac{r}{a}\right)^2}\right)\right. \\ \left. + \frac{\delta F^e}{\delta x}\left(x + a + a\sqrt{1 - \left(\frac{r}{a}\right)^2}\right) r dr \qquad (2.6)$$

The Van der Waals force for a particle plate geometry can be used to calculate the attraction force of a particle toward a surface (Equation 2.7), where A is the Hamaker constant, r is particle diameter, and z is ratio of separation distance to particle diameter

(x/d). [70] The overall electrostatic force balance can then be performed on the particle by summing all the forces together, with repulsive forces giving a positive force, while the attractive forces produce a negative force (Equation 2.8).

$$F_{vdw} = -\frac{A}{12r}\left(\frac{2}{z} - \frac{1}{z^2} - \frac{2}{z+1} - \frac{1}{(z+1)^2}\right) \quad (2.7)$$

$$F_{total} = F_{es} + F_{vdw} \quad (2.8)$$

The electrophoretic force acting on a particle of a given size can be calculated using Equation 2.9, where d is particle diameter, η is dynamic viscosity, λ is a correction factor, μ is electrophoretic mobility and E is the electrical field.

$F_{ep} = 3\pi d\eta\lambda\mu E$ (2.9)

2.5 Fouling Experiments and Model Results

2.5.1 Experimental Results

Fouling experiments were performed on both the PS-35 support (no CNT layer) and PVA-CNT-COOH films cast on PS-35, with the system operating in a constant flux mode (20 LMH), and pressure increase indicating fouling. Fouling tests with 250 mg/L of PEO, a neutral fouling molecule, demonstrated that PS-35 fouled at a faster rate than the PVA-CNT-COOH membranes, with a final operating pressure of 25±1 psi vs. 17±2 psi, respectively, after 100 minutes of operation (Figure 2.10). The fouling inhibition of PVA-CNT-COOH films is due to their higher hydrophilicity, which has been previously demonstrated to improve UF membrane fouling resistance.[71–74] Furthermore, the application of an electrical potential to the PVA-CNT-COOH membranes had no

significant impact on PEO fouling, due to the near neutral charge of PEO (ξ = -7.5 mV). This charge is not significant, and it is not surprising that electrostatics had little to no involvement in PEO-membrane interaction. Fouling tests using AA, a highly negatively charged molecule (ξ = -68.1 mV), at a concentration of 5g/L demonstrated higher fouling rates of PS-35 compared to the uncharged PVA-CNT-COOH cast on PS-35, again due to the increased hydrophilic nature of the PVA-CNT-COOH membrane (16±1 psi vs. 21±1 psi after 100 minutes; Figure 2.11). The application of -3 V and -5 V to the membrane surface resulted in significantly lower pressures needed to maintain a flux of 20 LMH with final pressures change after 100 minutes of operation being 7.8 psi, 5.2 psi and 3.8 psi for the 0 V, -3 V, and -5 V, respectively representing a reduction 33.7%, and 51.1% vs. no potential condition (Figure 2.11).

The Effect of salts typically present in wastewater were tested with a SW-AA solution with AA concentration of 3g/L. Fouling of PS-35 was not significantly worse than that of PVA-CNT-COOH films cast on PS-35 (Figure 2.12). The low impact of hydrophilicity on fouling of SW-AA was likely due to the different fouling nature of the solution. The synthetic wastewater contains Ca^{+2} ions, which are known to cause complexation of AA, forming aggregates that induce colloidal, cake-like, fouling behavior and can form bridging elements between the foulant and membrane charged groups such as carboxylic acid groups. [3,75,76] This would result in a lower effect of hydrophilicity on fouling, as aggregates of AA would deposit on the surface, in addition to pore blocking and the formation of a gel layer, resulting in high fouling rates when compared to highly concentrated AA solution. When a potential of -3 V was applied to the membrane surface

no improvement in fouling inhibition was observed. A moderate fouling inhibition was observed at the application of a -5 V potential, with a reduction of 43% in the operating pressure change was observed, compared to the 0 V condition (11.5psi vs. 6.5psi respectively; Figure 2.12).

Experiments with applied positive potentials were performed to verify the impact of membrane potentials on fouling rates. Due to the negative charge of the AA molecule, it was expected that the membrane would experience increased fouling rates. Positive potentials of 1 V and 1.5 V DC were applied to a membrane that was treating a solution of 0.5 g/L AA, with the flux held constant at 40 LMH; the experiments were done in triplicates, and lasted 60 minutes each. The system pressure increased from 5.9±0.15 PSI at 0 V to 6.3±0.1 PSI at 1 V and 6.6±0.1 PSI 1.5 V. (Figure 2.13) It was further observed that the application of a positive potential resulted in irreversible membrane fouling. Higher anodic potentials (> 1.5 V) were not attempted as CNT networks experience degradation at those levels. [77,78] However, low potential experiments yielded expected results that agree with electrostatic fouling mechanisms.

2.5.2 Modeling Discussion

During the ultrafiltration experiments the hydrodynamic conditions arising from membrane roughness, surface groups, fluid flow, and flow channel dimensions were constant throughout all the fouling experiments. The only parameter that was changed during electrofiltration experiments was the magnitude of the electrical potential applied to the membrane surface. Therefore, qualitative analysis of the electrostatic forces should provide evidence for an electrostatic fouling inhibition mechanism. Importantly, the model

used here is not meant to capture the full range of forces that AA or a fouling molecule would experience. The electrophoretic force was also found to be significantly smaller then the electrostatic forces, with values 2.32e-6 nN and 3.86e-6 nN, at the application of -3 and -5 volts, respectively, for AA in DIW, and 2.7e-4 and 4.5e-4nN for SW-AA solution. These forces suggest that electrophoretic forces are insignificantly small in our system, and can be neglected in estimating the overall impact of electrical charge on the membrane surface.

The electrostatic force calculations employed the MPB equations, which take into account hydrated ion size, valance, and overall packing density. Based on the electric potential profiles produced by the MPB equations, the calculation of the free energy between the membrane surface and an alginate particle was made possible. Elevated counter-ion concentrations near an electrically charged surface are needed to maintain electroneutrality. However, due to the finite volume of a hydrated ion, only a finite number of hydrated ions can be packed into a given volume (a fact not captured by the standard PB equation). These elevated ion concentrations between the electrically charged membrane surface and charged particle create an osmotic force that must be overcome for the particle to approach the surface and deposit.[64] In effect, this suggests that the electrostatic force is present due to osmotic pressure, and its strength would be largely affected by ion size, valance and concentration vs. bulk ion concentrations. Thus, at similar surface charges, the overall force would be higher when only small monovalent ions are present due to their higher packing density and lower ability to satisfy electro-neutrality, compared to larger divalent ions. Alternatively, large divalent ions would satisfy electro-neutrality at lower concentration, resulting in lower ion excess, which leads to lower osmotic forces and

hence, lower repulsive forces. This would result in faster particle aggregation and deposition, which has been observed by a multitude of studies. [79–82]

Experimental results are qualitatively consistent with model calculations, and demonstrate that electrostatic repulsive forces have a significant impact on AA fouling. A surface potential of -0.1 V was used to model the case when no potential was applied to the membranes surface. Numerous publications have demonstrated that membrane surfaces containing carboxyl and hydroxyl groups placed in near-neutral pH water assume a negative surface charge due to the dissociation of a proton from the carboxylic acid group. [83,84] The AA in DI water was modeled with a particulate size of 5.0 nm (literature value, DLS measurement were unreliable) and surface potential of -68.1 mV, with solution conditions shown in Table 2.1.[85] The ionic strength of the 5 g/L AA solution in DIW was estimated based on the molar concentration of AA and assuming one charged group per AA monomer with a sodium ion to balance the charge; here, we assumed an AA ion activity of one, packing of 0.64 and Hamaker constant of 18.6 kT.[86]

Modeling results demonstrate that a strong electrostatic force is present when membrane surface potentials of -1.519 V and -3.412 V vs. the Ag/AgCl references (Application of -3 V and -5 V to the system, respectively) are applied. When only AA is added to DI water, a maximum repulsive force of 1.12 nN is attained at -1.519 V and only the position of the force maxima changes with increasing surface potential. (Figure 2.14) The force maxima is a result of the finite volume of hydrated ions that can accumulate at the charged surface; this leads to a maximum number of ions that can fit into a given volume, effectively capping the ion concentration and consequently, capping the maximum

repulsive force. However, increasing surface potentials will extend the maximum repulsive force away from the membrane surface, into the bulk fluid. The electrostatic force effectively acts as a fouling inhibitor, extending from the lower bound of surface roughness, making those areas impermeable to fouling agents. At -1.519 V, the maximum force would cover 36% of surface roughness and be located at 4.37 nm above surface, preventing some of the fouling. (Table 2.2) At a surface potential to -3.5 V, nearly 48% of the surface roughness would be covered by maximum repulsive forces, resulting in significant fouling inhibition, as experimentally observed.

Modeling of AA in synthetic wastewater demonstrated a highly reduced electrostatic repulsive force. (Figure 2.15) The ionic strength of the solution was calculated by adding the ionic strength of the synthetic wastewater with the ionic strength associated with 3.0 g/L of AA; the lower ionic strength of the SW-AA solution vs. the AA solution stems from the fact that there is much less AA in the SW-AA solution (3.0 g/L vs. 5 g/L), hence fewer ions. However, the presence of divalent ions, and in particular Ca^{+2} ions, is associated with enhanced aggregation and deposition of AA, as well as decreased electrostatic forces. The repulsive force maximum was reduced to 33 nN located 4.16 nm above the membrane surface. This large force compared to AA only max force is a result of the larger particle size of 292.8±53.4nm as measured by DLS, which allows for stronger interaction of the particle with the electrostatic field. The larger particle size (stemming from aggregation of AA molecules in the presence of divalent ions) would also mean that convective forces will now dominate its transport, and thus the maximum electrostatic forces should not be directly compared here. However, in the presence of synthetic

wastewater, the electrostatic forces do not extend as far into the solution; this is due to the presence of divalent ions (as mentioned above). The overall force maxima at -1.519 V is located at 3.14 nm above the surface resulting in only 25.96% of surface roughness coverage, which, based on our experimental results, appears to be insufficient to prevent fouling. At -3.5 V, nearly 34.4% of the surface roughness is covered by the maximum force, which results in partial membrane surface protection, and the observable fouling inhibition. The overall reduction in fouling inhibition is mostly due to reduction in distance over which the force is felt away from the membrane surface. Thus, the model calculations qualitatively explain the observed experimental fouling results.

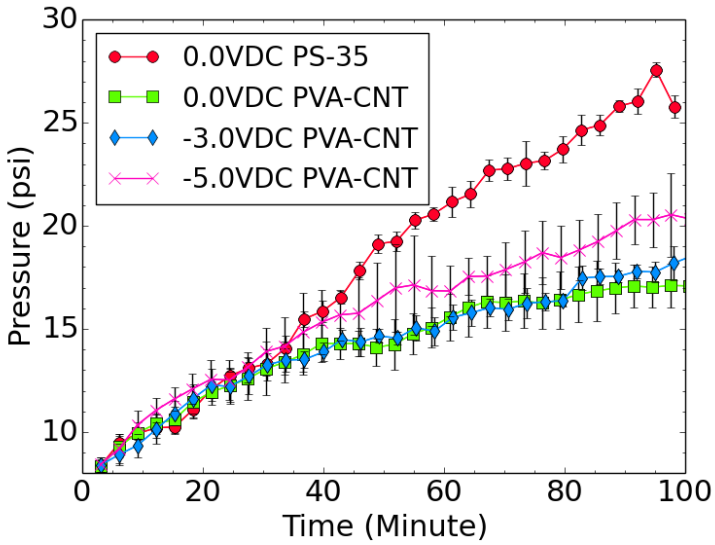

Figure 2.10: Fouling of 250 mg/L PEO on PS35 (duplicate data) and PVA-CNT Membranes

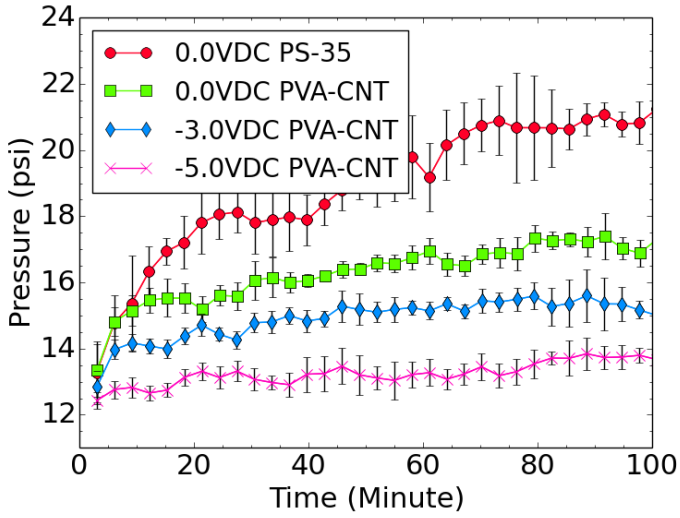

Figure 2.11: Fouling of 5g/L AA on PS-35 and PVA-CNT membranes

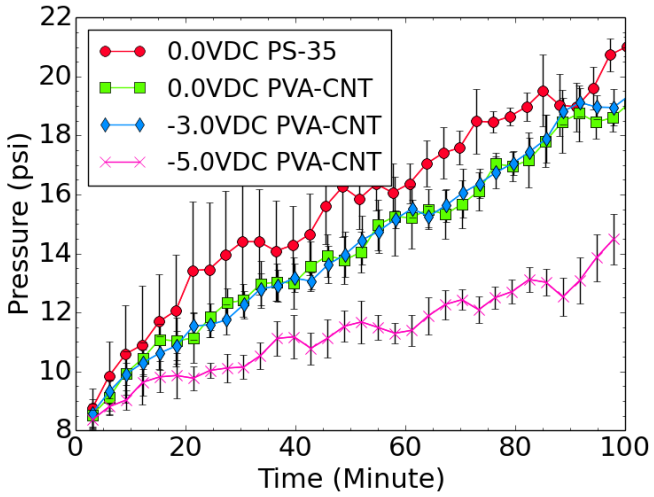

Figure 2.12: Fouling of 2.5 g/L of SW-AA on PS-35 and 3 g/L of SW-AA PVA-CNT

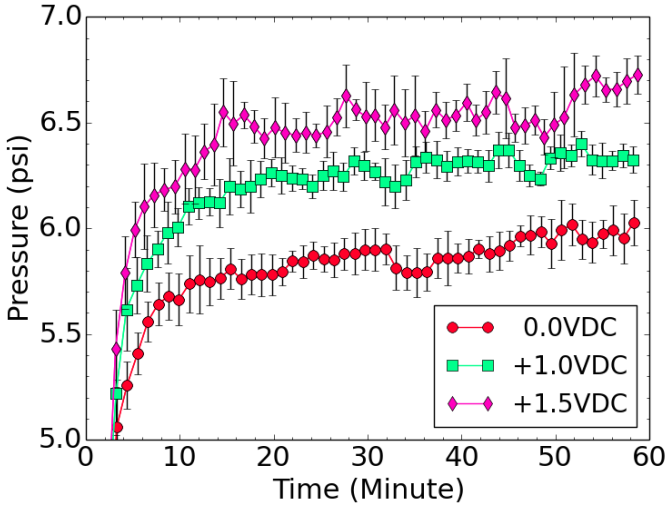

Figure 2.13: Fouling of 0.5g/L of AA solution under positive potentials on PVA-CNT membrane, at permeate flux of 40LMH.

Table 2.1: Modeling Parameters for AA in DI water and Synthetic Wastewater. Ion sizes are found from following references. [87]

Alginic Acid in DI Water			
Ion	C (mMol)	Valance	Radii (nm)
Alginate	25.36	-1	5.0
Na	25.36	1	0.45

Alginic Acid in Synthetic Wastewater			
Ion	C (mMol)	Valance	Radii (nm)
Sodium Citrate	1.03	-1	0.45
Na	16.61224	1	0.45
NH4	0.317	1	0.306
Cl	1.7389	-1	0.33
PO4H2	0.32	-1	0.375
K	0.129	1	0.53
Ca	0.263	2	0.46
Mg	0.121	2	0.421
SO4	0.4788	-1	0.37
HCO3	0.363	-1	0.45
Alginate	15.22	-1	5.0

Table 2.2: Maximum repulsive force positions, and percentage of surface roughness that is affected by the maxima force. (NA-no experimental run at given potential)

Solution	Experimental potential (V)	Surface Potential (V)	Force Peak Position	Percentage of roughness coverage (%)
SW-AA	NA	-0.1	1.497	12.37
	-3	-1.519	3.14	25.96
	-5	-3.412	4.16	34.39
AA	NA	-0.1	1.841	15.21
	-3	-1.519	4.37	36.07
	-5	-3.412	5.82	48.07

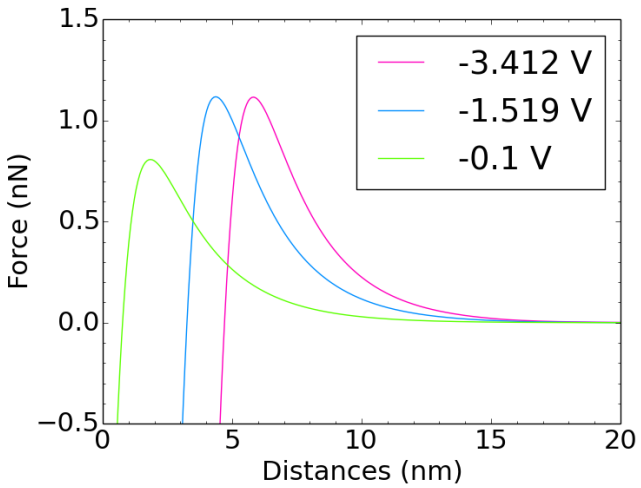

Figure 2.14: Overall force acting on an AA particle in a DIW solution containing 5 g/L AA at various distances from the surface and applied potentials at ionic strength of 25.36 mM.

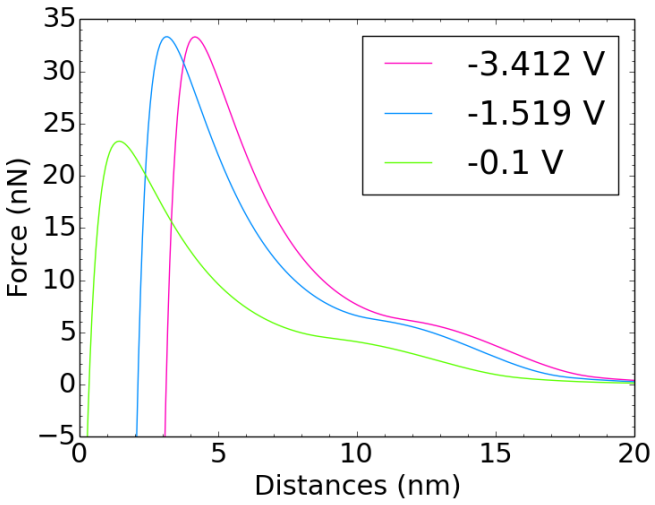

Figure 2.15: Forces acting on an AA particle in a synthetic wastewater solution containing 3.0 g/L AA at various distances from the surface and applied potentials at ionic strength of 18.87 mM.

2.6 Conclusion

Electrically conductive, robust and permeable PVA-CNT thin films have been coated onto ultrafiltration supports, and have been demonstrated to be cross-linked with GA. Coated membranes demonstrated lower fouling rates compared to standard PS-35 supports in high concentrations of AA solutions as well as AA solution in synthetic wastewater. When no electrical potential was applied to the membrane surface, fouling inhibition was attributed to the higher hydrophilicity of the coated membranes, which was primarily due to presence of PVA, rather than CNT-COOH. Under all solution conditions, the application of increasing voltages led to significant fouling inhibition. This fouling inhibition was demonstrated to be due to electrostatic repulsion through the use of the MPB equation. According to the model, an electrostatic repulsive force could provide partial surface roughness coverage, preventing alginate from interacting with the surface, resulting

in reduced fouling rates. The model predictions are in qualitative agreement with our experimental results. The power consumption during these experiments was low, at only 1.65 Watts/m^2 at -3 V, and 10 Watts/m^2 at -5 V (or, $1.65x10^{-3}$ kWh/m^2 and $10x10^{-3}$ kWh/m^2, respectively), for both AA and SW-AA solutions. As of December of 2013, the price of 1 kWh of electricity for industrial applications in CA was $0.099. Thus, the additional operating cost of applying -3 V or -5 V to a UF system would be $\$16.3x10^{-5}/m^2$ and $\$99x10^{-5}/m^2$, respectively. These membranes have the potential of significantly reducing the fouling of UF treatment processes, which would lead to simpler operational conditions and lower operating costs.

2.7 References

1. Fakhru'l-Razi, A. *et al.* Review of technologies for oil and gas produced water treatment. *J. Hazard. Mater.* **170,** 530–551 (2009).

2. Van der Bruggen, B., Vandecasteele, C., Van Gestel, T., Doyen, W. & Leysen, R. A review of pressure-driven membrane processes in wastewater treatment and drinking water production. *Environ. Prog.* **22,** 46–56 (2003).

3. Katsoufidou, K., Yiantsios, S. G. & Karabelas, A. J. Experimental study of ultrafiltration membrane fouling by sodium alginate and flux recovery by backwashing. *J. Membr. Sci.* **300,** 137–146 (2007).

4. Jönsson, A.-S. & Trägårdh, G. Fundamental principles of ultrafiltration. *Chem. Eng. Process. Process Intensif.* **27,** 67–81 (1990).

5. Ye, Y., Le Clech, P., Chen, V., Fane, A. G. & Jefferson, B. Fouling mechanisms of alginate solutions as model extracellular polymeric substances. *Desalination* **175,** 7–20 (2005).

6. Ye, Y., Clech, P. L., Chen, V. & Fane, A. G. Evolution of fouling during crossflow filtration of model EPS solutions. *J. Membr. Sci.* **264,** 190–199 (2005).

7. Ye, Y., Chen, V. & Fane, A. G. Modeling long-term subcritical filtration of model EPS solutions. *Desalination* **191,** 318–327 (2006).

8. García-Molina, V., Lyko, S., Esplugas, S., Wintgens, T. & Melin, T. Ultrafiltration of aqueous solutions containing organic polymers. *Desalination* **189,** 110–118 (2006).

9. García-Molina, V., Esplugas, S., Wintgens, T. & Melin, T. Ultrafiltration of aqueous solutions containing dextran. *Desalination* **188,** 217–227 (2006).

10. Susanto, H. & Ulbricht, M. Influence of ultrafiltration membrane characteristics on adsorptive fouling with dextrans. *J. Membr. Sci.* **266,** 132–142 (2005).

11. Broeckmann, A., Wintgens, T. & Schäfer, A. I. Removal and fouling mechanisms in nanofiltration of polysaccharide solutions. *Desalination* **178,** 149–159 (2005).

12. Hilal, N., Ogunbiyi, O. O., Miles, N. J. & Nigmatullin, R. Methods Employed for Control of Fouling in MF and UF Membranes: A Comprehensive Review. *Sep. Sci. Technol.* **40,** 1957–2005 (2005).

13. Lee, N., Amy, G., Croué, J.-P. & Buisson, H. Identification and understanding of fouling in low-pressure membrane (MF/UF) filtration by natural organic matter (NOM). *Water Res.* **38,** 4511–4523 (2004).

14. Ozaki, N. & Yamamoto, K. Hydraulic effects on sludge accumulation on membrane surface in crossflow filtration. *Water Res.* **35,** 3137–3146 (2001).

15. Ducom, G., Puech, F. P. & Cabassud, C. Air sparging with flat sheet nanofiltration: a link between wall shear stresses and flux enhancement. *Desalination* **145,** 97–102 (2002).

16. Cui, Z. ., Chang, S. & Fane, A. . The use of gas bubbling to enhance membrane processes. *J. Membr. Sci.* **221,** 1–35 (2003).

17. Zhang, K., Cui, Z. & Field, R. W. Effect of bubble size and frequency on mass transfer in flat sheet MBR. *J. Membr. Sci.* **332,** 30–37 (2009).

18. Cabassud, C., Laborie, S., Durand-Bourlier, L. & Laine, J. M. Air sparging in ultrafiltration hollow fibers: relationship between flux enhancement, cake characteristics and hydrodynamic parameters. *J. Membr. Sci.* **181,** 57–69 (2001).

19. Beckett, R. & Le, N. P. The role or organic matter and ionic composition in determining the surface charge of suspended particles in natural waters. *Colloids Surf.* **44,** 35–49 (1990).

20. Hong, S. & Elimelech, M. Chemical and physical aspects of natural organic matter (NOM) fouling of nanofiltration membranes. *J. Membr. Sci.* **132,** 159–181 (1997).

21. Susanto, H., Arafat, H., Janssen, E. M. L. & Ulbricht, M. Ultrafiltration of polysaccharide–protein mixtures: Elucidation of fouling mechanisms and fouling control by membrane surface modification. *Sep. Purif. Technol.* **63,** 558–565 (2008).

22. Park, J.-S. *et al.* Fouling mitigation of anion exchange membrane by zeta potential control. *J. Colloid Interface Sci.* **259,** 293–300 (2003).

23. Harnsilawat, T., Pongsawatmanit, R. & Mcclements, D. Characterization of β-lactoglobulin–sodium alginate interactions in aqueous solutions: A calorimetry, light scattering, electrophoretic mobility and solubility study. *Food Hydrocoll.* **20,** 577–585 (2006).

24. Kim, K. S., Lee, K. H., Cho, K. & Park, C. E. Surface modification of polysulfone ultrafiltration membrane by oxygen plasma treatment. *J. Membr. Sci.* **199,** 135–145 (2002).

25. Nabe, A. Surface modification of polysulfone ultrafiltration membranes and fouling by BSA solutions. *J. Membr. Sci.* **133,** 57–72 (1997).

26. Moulik, S. P. Physical aspects of electrofiltration. *Environ. Sci. Technol.* **5,** 771–776 (1971).

27. Huotari, H. M., Trägårdh, G. & Huisman, I. H. Crossflow Membrane Filtration Enhanced by an External DC Electric Field: A Review. *Chem. Eng. Res. Des.* **77,** 461–468 (1999).

28. Weber, K. & Stahl, W. Improvement of filtration kinetics by pressure electrofiltration. *Sep. Purif. Technol.* **26,** 69–80 (2002).

29. Weigert, T., Altmann, J. & Ripperger, S. Crossflow electrofiltration in pilot scale. *J. Membr. Sci.* **159,** 253–262 (1999).

30. Hofmann, R. & Posten, C. Improvement of dead-end filtration of biopolymers with pressure electrofiltration. *Chem. Eng. Sci.* **58,** 3847–3858 (2003).

31. Yang, G. & Li, C. Electrofiltration of silica nanoparticle-containing wastewater using tubular ceramic membranes. *Sep. Purif. Technol.* **58,** 159–165 (2007).

32. Yang, G. C., Yang, T.-Y. & Tsai, S.-H. Crossflow electro-microfiltration of oxide-CMP wastewater. *Water Res.* **37,** 785–792 (2003).

33. Guillen, G. R. & Hoek, E. M. *Development and Testing of 'Smart' Nanofiltration Membranes*. (NWRI Final Project Report. Los Angeles, CA: Department of Civil & Environmental Engineering, University of California, 2010).

34. Enevoldsen, A. D., Hansen, E. B. & Jonsson, G. Electro-ultrafiltration of industrial enzyme solutions. *J. Membr. Sci.* **299,** 28–37 (2007).

35. Mansouri, J. & Burford, R. P. Novel membranes from conducting polymers. *J. Membr. Sci.* **87,** 23–34 (1994).

36. Price, W. E., Too, C. O., Wallace, G. G. & Zhou, D. Development of membrane systems based on conducting polymers. *Synth. Met.* **102,** 1338–1341 (1999).

37. McCullough, R. D. The Chemistry of Conducting Polythiophenes. *Adv. Mater.* **10,** 93–116 (1998).

38. Loh, I.-H., Moody, R. A. & Huang, J. C. Electrically conductive membranes: Synthesis and applications. *J. Membr. Sci.* **50,** 31–49 (1990).

39. Liu, L., Liu, J., Gao, B., Yang, F. & Chellam, S. Fouling reductions in a membrane bioreactor using an intermittent electric field and cathodic membrane modified by vapor phase polymerized pyrrole. *J. Membr. Sci.* **394–395,** 202–208 (2012).

40. Huotari, H. M., Huisman, I. H. & Trägårdh, G. Electrically enhanced crossflow membrane filtration of oily waste water using the membrane as a cathode. *J. Membr. Sci.* **156,** 49–60 (1999).

41. Faibish, R. S. & Cohen, Y. Fouling-resistant ceramic-supported polymer membranes for ultrafiltration of oil-in-water microemulsions. *J. Membr. Sci.* **185,** 129–143 (2001).

42. Bowen, W. R., Kingdon, R. S. & Sabuni, H. A. M. Electrically enhanced separation processes: the basis of in situ intermittent electrolytic membrane cleaning (IIEMC) and in situ electrolytic membrane restoration (IEMR). *J. Membr. Sci.* **40,** 219–229 (1989).

43. Zaky, A. M. & Chaplin, B. P. Porous Substoichiometric TiO $_2$ Anodes as Reactive Electrochemical Membranes for Water Treatment. *Environ. Sci. Technol.* 130605131639002 (2013). doi:10.1021/es401287e

44. de Lannoy, C., Jassby, D., Davis, D. D. & Wiesner, M. R. A highly electrically conductive polymer–multiwalled carbon nanotube nanocomposite membrane. *J. Membr. Sci.* **415–416,** 718–724 (2012).

45. Benjamine, M., Liu, J. & Malczewska, B. New studies of hybrid adsorption/membrane treatment systems: Mechanisms of fouling mitigation. (2013).

46. Herzberg, M. & Elimelech, M. Biofouling of reverse osmosis membranes: Role of biofilm-enhanced osmotic pressure. *J. Membr. Sci.* **295,** 11–20 (2007).

47. Lee, S. W., Kim, B.-S., Chen, S., Shao-Horn, Y. & Hammond, P. T. Layer-by-Layer Assembly of All Carbon Nanotube Ultrathin Films for Electrochemical Applications. *J. Am. Chem. Soc.* **131,** 671–679 (2009).

48. Tsai, C.-C. & Teng, H. Chromium-doped titanium dioxide thin-film photoanodes in visible-light-induced water cleavage. *Appl. Surf. Sci.* **254,** 4912–4918 (2008).

49. Geng, H.-Z. *et al.* Effect of acid treatment on carbon nanotube-based flexible transparent conducting films. *J. Am. Chem. Soc.* **129,** 7758–7759 (2007).

50. Djennad, M., Benachour, D., Berger, H. & Schomäcker, R. Poly(vinyl alcohol) Ultrafiltration Membranes: Synthesis, Characterization, the Use for Enzyme Immobilization. *Eng. Life Sci.* **3,** 446–452 (2003).

51. Mansur, H. S., Sadahira, C. M., Souza, A. N. & Mansur, A. A. P. FTIR spectroscopy characterization of poly (vinyl alcohol) hydrogel with different hydrolysis degree and chemically crosslinked with glutaraldehyde. *Mater. Sci. Eng. C* **28,** 539–548 (2008).

52. Bolto, B., Tran, T., Hoang, M. & Xie, Z. Crosslinked poly(vinyl alcohol) membranes. *Prog. Polym. Sci.* **34,** 969–981 (2009).

53. Kim, K.-J., Lee, S.-B. & Han, N.-W. Kinetics of crosslinking reaction of PVA membrane with glutaraldehyde. *Korean J. Chem. Eng.* **11,** 41–47 (1994).

54. Ramanathan, T., Fisher, F. T., Ruoff, R. S. & Brinson, L. C. Amino-Functionalized Carbon Nanotubes for Binding to Polymers and Biological Systems. *Chem. Mater.* **17,** 1290–1295 (2005).

55. Salzmann, C. G. *et al.* The Role of Carboxylated Carbonaceous Fragments in the Functionalization and Spectroscopy of a Single-Walled Carbon-Nanotube Material. *Adv. Mater.* **19,** 883–887 (2007).

56. Buzaneva, E. *et al.* DNA nanotechnology of carbon nanotube cells: physico-chemical models of self-organization and properties. *Mater. Sci. Eng. C* **19,** 41–45 (2002).

57. Kilic, M. S., Bazant, M. Z. & Ajdari, A. Steric effects in the dynamics of electrolytes at large applied voltages. I. Double-layer charging. *Phys. Rev. E* **75,** (2007).

58. Borukhov, I., Andelman, D. & Orland, H. Steric effects in electrolytes: A modified Poisson-Boltzmann equation. *Phys. Rev. Lett.* **79,** 435 (1997).

59. Ben-Yaakov, D., Andelman, D., Podgornik, R. & Harries, D. Ion-specific hydration effects: Extending the Poisson-Boltzmann theory. *Curr. Opin. Colloid Interface Sci.* **16,** 542–550 (2011).

60. Ben-Yaakov, D., Andelman, D., Harries, D. & Podgornik, R. Beyond standard Poisson–Boltzmann theory: ion-specific interactions in aqueous solutions. *J. Phys. Condens. Matter* **21,** 424106 (2009).

61. López-García, J. J., Horno, J. & Grosse, C. Poisson–Boltzmann Description of the Electrical Double Layer Including Ion Size Effects. *Langmuir* **27,** 13970–13974 (2011).

62. Boström, M., Williams, D. & Ninham, B. Specific Ion Effects: Why DLVO Theory Fails for Biology and Colloid Systems. *Phys. Rev. Lett.* **87,** 168103 (2001).

63. Boström, M., Williams, D. R. M. & Ninham, B. W. Specific Ion Effects: Why DLVO Theory Fails for Biology and Colloid Systems. *Phys. Rev. Lett.* **87,** (2001).

64. Verwey, E. & Overbeek, T. *Theory of stabilty of lyophobic colloids*. (Elsievier Publishing Company, 1948).

65. Bhattacharjee, S. & Elimelech, M. Surface Element Integration: A Novel Technique for Evaluation of DLVO Interaction between a Particle and a Flat Plate. *J. Colloid Interface Sci.* **193,** 273–285 (1997).

66. Butt, H.-J. Measuring electrostatic, van der Waals, and hydration forces in electrolyte solutions with an atomic force microscope. *Biophys. J.* **60,** 1438 (1991).

67. Boström, M., Deniz, V., Franks, G. V. & Ninham, B. W. Extended DLVO theory: Electrostatic and non-electrostatic forces in oxide suspensions. *Adv. Colloid Interface Sci.* **123–126,** 5–15 (2006).

68. Rotsch, C. & Radmacher, M. Mapping Local Electrostatic Forces with the Atomic Force Microscope. *Langmuir* **13,** 2825–2832 (1997).

69. Israelachvili, J. Solvation forces and liquid structure, as probed by direct force measurements. *Acc. Chem. Res.* **20,** 415–421 (1987).

70. Hamaker, H. C. The London—van der Waals attraction between spherical particles. *Physica* **4,** 1058–1072 (1937).

71. Du, J. R., Peldszus, S., Huck, P. M. & Feng, X. Modification of poly(vinylidene fluoride) ultrafiltration membranes with poly(vinyl alcohol) for fouling control in drinking water treatment. *Water Res.* **43,** 4559–4568 (2009).

72. Zhang, Y., Li, H., Li, H., Li, R. & Xiao, C. Preparation and characterization of modified polyvinyl alcohol ultrafiltration membranes. *Desalination* **192,** 214–223 (2006).

73. Na, L., Zhongzhou, L. & Shuguang, X. Dynamically formed poly (vinyl alcohol) ultrafiltration membranes with good anti-fouling characteristics. *J. Membr. Sci.* **169,** 17–28 (2000).

74. Ma, X., Su, Y., Sun, Q., Wang, Y. & Jiang, Z. Enhancing the antifouling property of polyethersulfone ultrafiltration membranes through surface adsorption-crosslinking of poly(vinyl alcohol). *J. Membr. Sci.* **300,** 71–78 (2007).

75. Jermann, D., Pronk, W., Meylan, S. & Boller, M. Interplay of different NOM fouling mechanisms during ultrafiltration for drinking water production. *Water Res.* **41,** 1713–1722 (2007).

76. van den Brink, P., Zwijnenburg, A., Smith, G., Temmink, H. & van Loosdrecht, M. Effect of free calcium concentration and ionic strength on alginate fouling in cross-flow membrane filtration. *J. Membr. Sci.* **345,** 207–216 (2009).

77. Ohmori, S. & Saito, T. Electrochemical durability of single-wall carbon nanotube electrode against anodic oxidation in water. *Carbon* **50,** 4932–4938 (2012).

78. Liu, H., Vajpayee, A. & Vecitis, C. D. Bismuth-Doped Tin Oxide-Coated Carbon Nanotube Network: Improved Anode Stability and Efficiency for Flow-Through Organic Electrooxidation. *ACS Appl. Mater. Interfaces* **5,** 10054–10066 (2013).

79. Overbeek, J. T. G. The Rule of Schulze and Hardy. *Pure Appl. Chem.* **52,** (1980).

80. Hsu, J.-P. & Kuo, Y.-C. An Extension of the Schulze-Hardy Rule to Asymmetric Electrolytes. *J. Colloid Interface Sci.* **171,** 254–255 (1995).

81. Nowicki, W. & Nowicka, G. Verification of the Schulze-Hardy rule: a colloid chemistry experiment. *J. Chem. Educ.* **71,** 624 (1994).

82. Metcalfe, I. M. & Healy, T. W. Charge-regulation modelling of the Schulze–Hardy rule and related coagulation effects. *Faraday Discuss Chem Soc* **90,** 335–344 (1990).

83. Elimelech, M., Chen, W. H. & Waypa, J. J. Measuring the zeta (electrokinetic) potential of reverse osmosis membranes by a streaming potential analyzer. *Desalination* **95,** 269–286 (1994).

84. Bellona, C., Drewes, J. E., Xu, P. & Amy, G. Factors affecting the rejection of organic solutes during NF/RO treatment—a literature review. *Water Res.* **38,** 2795–2809 (2004).

85. Wu, J., Contreras, A. E. & Li, Q. Studying the impact of RO membrane surface functional groups on alginate fouling in seawater desalination. *J. Membr. Sci.* **458,** 120–127 (2014).

86. Rijnaarts, H. H. M., Norde, W., Bouwer, E. J., Lyklema, J. & Zehnder, A. J. B. Reversibility and mechanism of bacterial adhesion. *Colloids Surf. B Biointerfaces* **4,** 5–22 (1995).

87. Ohtaki, H. & Radnai, T. Structure and dynamics of hydrated ions. *Chem. Rev.* **93,** 1157–1204 (1993).

Chapter 3 Coupling Underwater Superoleophobic Membranes with Magnetic Pickering Emulsions for Fouling-Free Separation of Crude Oil/Water Mixtures: An Experimental and Theoretical Study

3.1 Summary

Oil/water separations have become an area of great interest, as growing oil extraction activities are increasing the generation of oily wastewaters as well as increasing the risk of oil spills. Here, we demonstrate a membrane-based and fouling-free oil/water separation method that couples carbon nanotube - poly(vinyl alcohol) underwater superoleophobic ultrafiltration membranes with magnetic Pickering emulsions. We demonstrate that this process is insensitive to low water temperatures, high ionic strength, or crude oil loading, while allowing operation at high permeate fluxes and producing high quality permeate. Furthermore, we develop a theoretical framework that analyzes the stability of Pickering emulsions under filtration mechanics, relating membrane surface properties and hydrodynamic conditions in the Pickering emulsion cake layer to membrane performance. Finally, we demonstrate the recovery and recyclability of the nano-magnetite used to form the Pickering emulsions through a magnetic separation step, resulting in an environmentally friendly, continuous process for oil/water separation.

3.2 Introduction

Over the last 30 years the demand for fossil fuels has dramatically increased, with growing demand projected to increase well into the future. [1,2] The extraction of crude oil leads to a potential for large oil spills, such as seen during the Deepwater Horizon disaster. [3] Furthermore, modern extraction processes generate large volumes of complex oily wastewater, known as produced water, which contain oil (free and emulsified), surfactants, and minerals. [4] The free oil and oil emulsions that are present in produced water, as well

as generated during oil spills, pose a significant hazard to the environment. [5,6] This hazard has created a pressing need to develop an effective method of treatment, with the majority of recent work exploring novel materials that exhibit superhydrophobicity/superoleophilicity or superhydrophilicity/underwater superoleophobicity. [7–19]

Superhydrophilic/underwater superoleophobic membranes and meshes have been developed to physically separate oil from water, with the goal of minimizing membrane fouling and increasing oil rejection. [7–13] Membrane fouling from oil, where oil clogs membrane pores, is a common problem in membrane separation of oil emulsions. [20,21] Although some filtration techniques have demonstrated excellent oil removal, the majority of studies do not present fouling data or demonstrate whether the membranes suffer from fouling. [10,11] Superhydrophobic/superolephilic foams and meshes have been synthesized for chemical and physical sorption of oil from water, showing good separation and sorption performance, but they still have to overcome scale-up challenges, use of costly materials, and complicated fabrication procedures. [14–19] Magnetic Pickering emulsions have also been proposed for oil/water separation. Here, oil emulsions are stabilized with magnetic nanoparticles (NPs), which are removed from the water through the application of a magnetic field. [22–25] However, the use of magnetic fields poses a big challenge for scalability, as the magnetic field strength drops with an inverse cubed law, thus requiring a large magnetic surface area to effectively treat the vast volumes of fluids collected during oil spills.

Herein we describe a novel method of oil/water separation by coupling carbon nanotube - poly(vinyl alcohol) (CNT-PVA) underwater superoleophobic ultrafiltration (UF) membranes to magnetic Pickering emulsions. In this approach, the Pickering emulsions are used to prevent oil coalescence in the cake layer that forms on the membrane surface during filtration, while underwater superoleophobicity prevents membrane wetting and consequent fouling. We demonstrate how water contaminated with large amounts of crude oil (up to 10% by volume) can be effectively treated with UF membranes without the extreme fouling typically observed in this process while producing a permeate stream with less than 15 ppm of total organic carbon (TOC) (regardless of the oil concentration in the feed). We further develop a theoretical framework that describes the interaction of NP-stabilized oil (i.e. a Pickering emulsion) with a porous surface (i.e. a UF membrane) under filtration mechanics. The framework considers the interaction energy between the oil/NPs and oil/surface as a function of pressure gradients typical in membrane separation processes. Furthermore, we demonstrate how the NPs can be magnetically recovered from the concentrated Pickering emulsions, allowing for their reuse in another round of oil/water separation. The robust and sustainable water treatment process described here is insensitive to crude oil concentrations (tested with concentrations up to 10% v/v oil/water), temperature, ionic strength and species, and can be used for the separation and recovery of oil from wastewater and during oil-spill remediation activities.

3.3 Results and Discussion

3.3.1 Characterization of Oil and Pickering Emulsions

We have developed a novel method of oil/water separation using Pickering emulsions coupled to underwater superoleophobic ultrafiltration membranes. Crude oil emulsions were prepared by using a simple blending process, which formed polydisperse oil droplets with a majority of droplets having a diameter bellow 6 μm (Figure 3.1 a, c). The small, emulsified crude oil droplets are potent foulants; during filtration they can coalesce to form oil films on the membrane surface and/or deform and penetrate into the membrane pores, which results in irreversible membrane fouling and rapid performance decline. [21,26,27] Oil coalescence can be prevented via Pickering emulsions, which have been of great interest as they are capable of stabilizing large concentrations of oil in water. [24,28–32] Pickering emulsions were prepared with Fe_3O_4 nanopowder (FeNPs) and polyvinylpyrrolidone-coated Fe_3O_4 nanopowder (FePVP) that had a water contact angle of 40°±3 and 6.8°±1, respectively (Figure A3.1). FeNP and FePVP both had a primary particle size of 20-40 nm. However, due to their ferromagnetic qualities, these particles form aggregates with a diameter of 608±7 nm and 727±40 nm, respectively, as determined by dynamic light scattering (DLS). The Pickering emulsions were prepared via a simple mixing process where 10 g/L of FeNPs or FePVPs were added to 10 ml/L of emulsified crude oil and mixed with a paddle mixer for 1 and 3 hours, respectively (Figure 3.1b, c). The longer mixing time was needed for FePVP due to their very hydrophilic nature (water contact angle of 6.8°±1) that leads to a small energy well for entering the water/oil interface (165 kT) compared to FeNPs that had a contact angle of 40°±3 and an energy well of

~1.8x10^5 kT (calculated for surface tension 0.05 Nm^{-1} and an oil drop with a radius of 3.3 μm) (Figure A3.1, A3.2). [33]

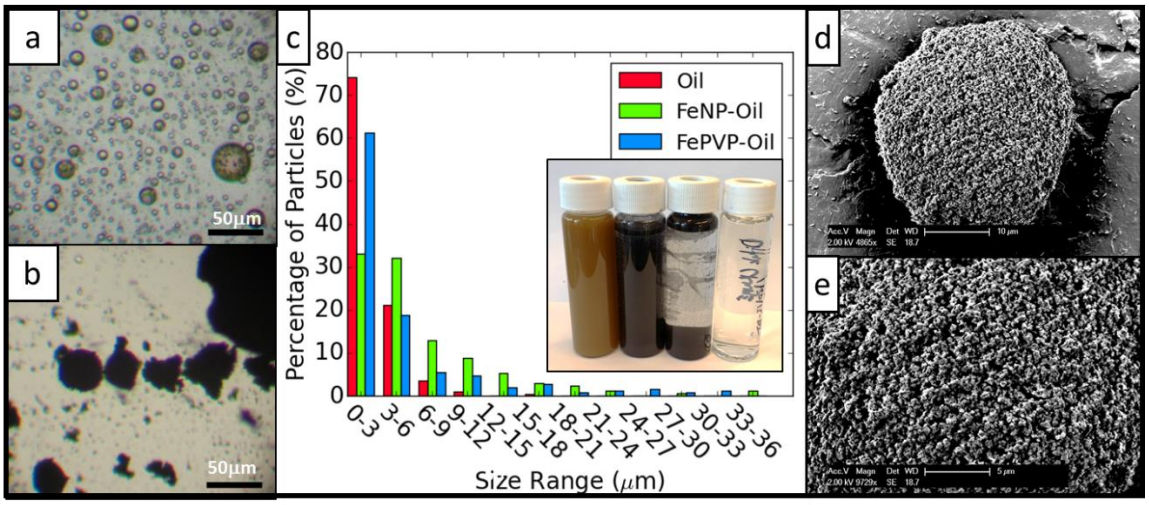

Figure 3.1: Images of oil and Pickering emulsions. (a) Image of a typical (non-stabilized) crude oil emulsion. (b) Image of FeNP Pickering emulsions. (c) Size (diameter) distribution of oil and Pickering emulsions; (Inset) vial contents are from left to right: 10 ml/L crude oil emulsion, 10 ml/L Pickering emulsion, gravity separated 10 ml/L Pickering emulsion, and UF permeate with <15 ppm TOC. (d) SEM image of NP-stabilized oil drop. (e) Higher resolution image of magnetic NPs on the surface of the oil drop.

The FeNP and FePVP– stabilized oil droplets had a similar size distribution compared to the unstabilized crude oil emulsion, the FePVP-stabilized oil is slightly smaller, with nearly 60 % of droplets having a diameter bellow 3 μm (Figure 3.1b, c). The formation of larger droplets that are not observed in the pure crude oil emulsions is attributed to the ferromagnetic properties of NPs, which aggregate smaller droplets. Scanning electron microscopy (SEM) image analysis further confirms the presence of a dense FeNP coating on the surface of the oil droplets, which form a protective layer at the oil/water interface (Figure 3.1d, e). The Pickering emulsions were extremely stable, and did not phase-separate into oil, water and NP phases even after several months of storage

at room temperature. After prolonged periods, a large fraction of the NP – stabilized oil settles out, with a smaller fraction remaining suspended at the top of the aqueous phase, likely due to creaming (Figure 3.1c inset); the aqueous phase had no visible oil, with a TOC of 13±7 PPM (as measured with a TOC analyzer), which further demonstrates that all of the oil was trapped in a Pickering emulsion.

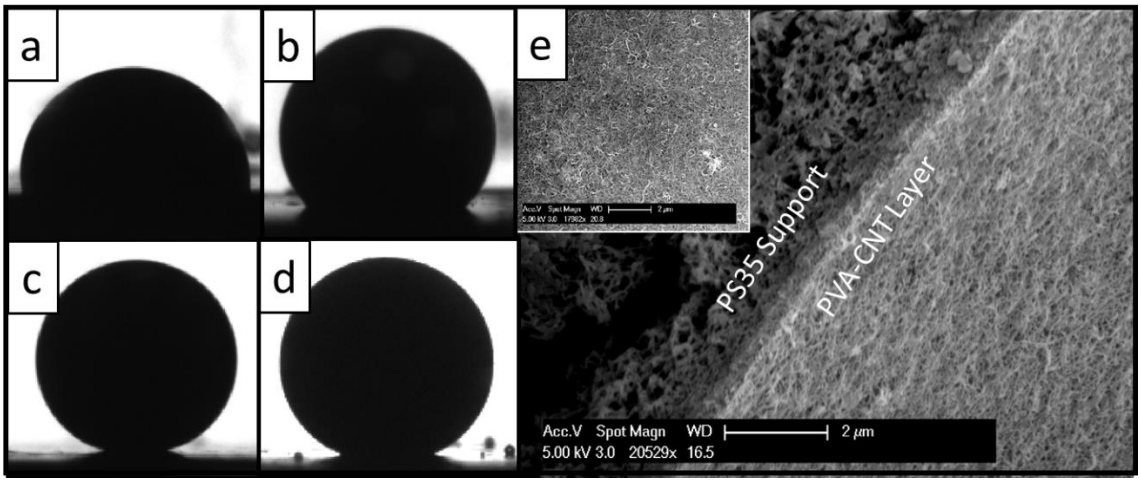

Figure 3.2: Underwater contact angles of crude oil drops with the membrane surface after 20 minutes on (a) PS35 with contact angle of 100±2°, (b) PAN with contact angle of 130±2°, (c) PVA-CNT with contact angle of 168±2°, and (d) PS35 with FeNP-stabilized crude oil drop and contact angle of 155±2°. (e) Cross sectional SEM image of PVA-CNT membrane on PS35 support. (Inset) Top surface of the PVA-CNT layer showing the overall smoothness of the membrane.

3.3.2 Oil/Water Separation

The fouling propensity of the NP – stabilized oil drops was investigated on a range of membrane materials that had different hydrophilic surface properties. The membrane materials included two commercially available UF membranes made of polysulfone (PS35) and polyacrylonitrile (PAN), and two modified UF membranes with poly(vinyl alcohol) carbon nanotube coating (PVA-CNT) on PS35 (PS35-CNT) and PAN (PAN-CNT). The PVA-CNT coating deposited on the PS35 or PAN support governs the membrane surface

properties, including hydrophilicity, but does not influence their rejection properties or permeability, as demonstrated by Dudchenko et al. (2014) (Figure 3.2e). [34] The tendency of the membranes to become wetted by oil was measured by allowing a crude oil drop to contact the membrane in a water-filled inverse cell, and measuring the contact angle over a 20 minute period. After 20 minutes, the contact angles were 100°±2, 130°±2, and 168°±3, for the PSF, PAN, and PVA-CNT membranes, respectively, with smaller angles corresponding to a more hydrophobic surface that is more readily wetted by the oil (Figure 3.2a, b, c and Figure A3.3). The high contact angle of the PVA-CNT membranes with oil demonstrates their underwater superoleophobic properties; however, their contact angle with oil in air was below 30°. When an FeNP coated oil drop was allowed to come in contact with the hydrophobic PS35 membrane, the contact angle increased from 100°±2 (the bare oil drop on the PS35 membrane) to 155°±2 (Figure 3.2d and Figure A3.3), which clearly demonstrates that a coating of FeNPs greatly reduces the ability of an oil drop to wet a surface by preventing physical contact between the crude oil and the membrane surface.

Although PVA-CNT membranes demonstrate excellent underwater superoleophobicity, they are still prone to a high degree of fouling when filtering pure oil emulsions (0.5 ml/L of crude oil in deionized water (DIW)) (Figure A3.4). Under these conditions, flux step experiments [35–37] demonstrate that when the membranes operate at fluxes below 30 l/m^2 hr (LMH) the membranes experienced fouling rates of 2-5 psi/hr; when operated at higher fluxes, the membranes rapidly fouled with flux declines exceeding 10 psi/hr (Figure A3.4). These fouling results indicate that even at low permeate fluxes and

oil concentrations, the membrane rapidly fouls, demonstrating that underwater superoleophobicity is not sufficient to treat water contaminated by emulsified crude oil. This finding demonstrates the complexity of treating water contaminated with crude oil, and indicates that underwater superoleophobic membranes alone are not capable of preventing membrane fouling.

To overcome the limitations imposed by the extreme fouling observed during the filtration of pure crude oil emulsions we use Pickering emulsions to improve system performance. We performed fouling experiments at a constant permeate flux of 50 LMH and 100 LMH with a cross flow velocity (CFV) of 15 cm/s, using FeNP and FePVP stabilized Pickering emulsions. In the first set of experiments, crude oil in DIW (10 ml/L) was stabilized with 10 g/L of NPs. At a constant permeate flux of 50 LMH, FeNPs – stabilized oil emulsions formed in DIW demonstrated no fouling, regardless of the membrane used (Figure 3.3a). In contrast, the use of FePVPs – stabilized oil in DIW resulted in rapid fouling (Figure 3.3a). At a constant permeate flux of 100 LMH, the FeNPs – stabilized emulsions in DIW were able to foul the PS35 and PAN membranes. However the PVA-CNT coated membranes continued to demonstrate excellent performance, with limited observable fouling over a period of 48 hours (Figure 3.3b). Not surprisingly, the FePVP – stabilized oil in DIW rapidly fouled the membranes at a flux of 100 LMH (Figure 3.3b). In all cases, the TOC content in the membrane permeate was below 15 ppm, indicating an oil removal efficiency exceeding >99.7 %.

The stability of the Pickering emulsions (10 ml/L of crude oil stabilized with 10 g/L of FeNPs) and the fouling resistance of PVA-CNT membranes was further challenged

with high ionic strength conditions, using a synthetic produced water (SPW) with an ionic strength of 2.24 M. [4] This water contained the most common ions present in produced waters, including a high loading of the divalent cations Ca^{+2} and Mg^{+2}, with a molar concentration of 0.171 M and 0.169 M, respectively. It was hypothesized that these divalent ions would lead to the complete collapse of any repulsive electrostatic forces between the NPs and oil drops, and possibly allow for bridging between the membrane surface and the Pickering emulsions, leading to rapid fouling. However, even after continuous operation for 48 hours at a permeate flux of 50 LMH and 180 hours at permeate flux of 100 LMH, no fouling was observed (Figure 3.3a, b). The lack of membrane fouling even under these harsh conditions indicates that electrostatic forces do not play a significant role in the stability of this system, and that divalent ionic bridging does not occur.

Since oil becomes more viscous at lower temperatures, and considering the increased probability of arctic oil drilling (and hence the increased probability of an arctic oil spill), the effect of temperature on system performance was also explored. Experiments were performed in synthetic seawater (SSW) at a temperature of 2°C. Long-term experiments were performed with a crude oil loading of 10 ml/L and 100 ml/L on a PS35-PVA-CNT membrane (CFV 25 cm/s). The reduced temperature had no impact on membrane performance, with no membrane fouling observed even at the high oil loading of 100 ml/L over a period of 80 hours (Figure 3.3c). Finally, concentration experiments were used to determine the maximum water recovery possible, where a Pickering emulsion with a concentration of 10 ml/L of crude oil was concentrated to 100ml/L of crude oil using PS35-PVA-CNT membrane (Figure 3.3d, CFV 10 cm/s). In this experiment, membrane

permeate was not returned to the feed tank, and the concentration of crude oil in the feed was allowed to increase. The PVA-CNT membranes again demonstrated excellent performance, and no fouling was observed at 90% recovery, with the observed pressure increase correlating nearly perfectly to the increase in crude oil concentration. These fouling experiments demonstrate that Pickering emulsions coupled to a UF treatment system provide a highly effective method for the treatment of oily waters. Excellent performance was observed regardless of the ionic strength, ionic species, temperature, or oil concentrations (within the limits of our testing), demonstrating the robustness of the treatment method even under highly challenging conditions, with excellent oil removal rates (>99.7 % and >99.9 % rejection at 10 ml/L and 100 ml/L crude oil loading, respectively).

The impact of the FeNPs on the structural properties of the oil and Pickering emulsion droplets was explored through force probing using an atomic force microscope (AFM). The results indicate that the stiffness of the crude oil drops does not change significantly with the addition of FeNPs, as implied by the near identical slopes of the force line generated during the retraction of the AFM probe (Appendix Section 3.6.2). [38] The AFM study did reveal the presence of a layer of FeNP at the oil/water interface, and it was further found that the FeNPs seem to rearrange as the tip is used to repeatedly probe the surface of the drop, indicating a mobile NP layer (Appendix Section A1, Figure A3.7a, b). These results suggest that under pressure the NP-stabilized oil drops will deform similarly to uncoated oil drops, and that the stiffness of the NP-stabilized oil drop does not impact membrane fouling, as demonstrated by the fouling experiments.

The deposition and attachment of NPs to the membrane surface can also lead to fouling. [39–41] The lack of fouling during the filtration of FeNP stabilized oil (with DI or SPW waters) indicates that the FeNPs do not deposit or sorb to the membrane surface. However, the FePVP stabilized oil did foul the membrane, which could be attributed to the FePVP particles themselves adsorbing to, and blocking, the membrane surface. Particles coated with PVP have been previously shown to preferentially attach to non-PVP coated surfaces under moderate ionic strength conditions. [42] However, membranes used during the FePVP stabilized oil separation experiments were made of PAN, which has PVP added to it during their manufacturing process. [43,44] Thus, the presence of PVP coating on PAN membranes and the low ionic strength during the FePVP experiments (DIW) would prevent preferential sorption of FePVPs to the membrane surface, and mitigate attachment of the FePVP particles to the membrane surface. Since fouling still occurred during these conditions, it can likely be attributed to oil coalescence. This information indicates that under the current experimental conditions, membrane performance when filtering FeNP/FePVP - stabilized oil is controlled by permeate flux, membrane oleophobicity, and NP contact angle, and not by specific interactions between the NPs and the membrane surface.

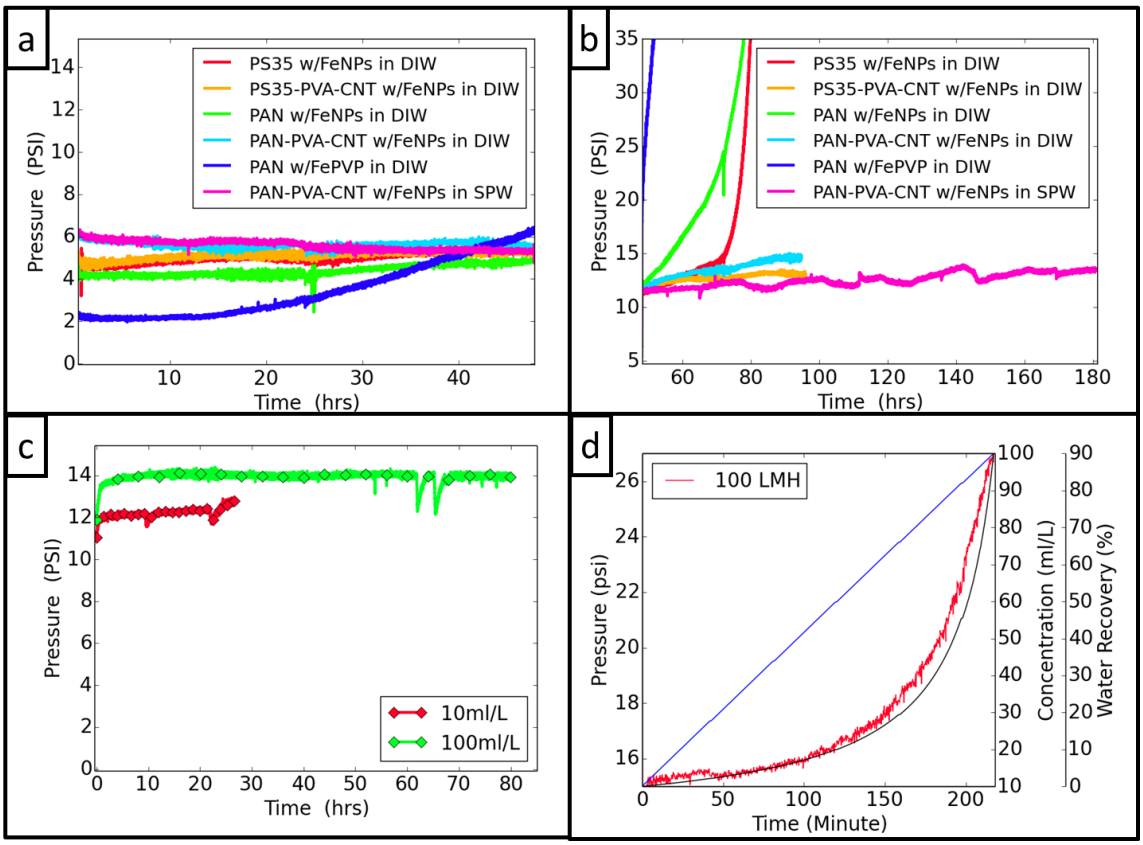

Figure 3.3: Membrane performance while treating NP-stabilized crude oil. (a) Membrane performance at 50 LMH with a cross-flow velocity of 15 cm/s. (b) Membrane performance at 100 LMH with a cross-flow velocity of 15 cm/s. (c) Fouling of PS35-PVA-CNT membrane in SSW at 2°C with a cross flow velocity of 25 cm/s with two crude oil concentrations (10 and 100 ml/L). (d) Concentration experiment on PS35-PVA-CNT membrane at 100 LMH in SSW at 2°C with a cross flow of 10 cm/s; the blue line is water recovery (%), the black line is crude oil concentration in (ml/L), and the red line is the system pressure.

3.3.3 Theoretical Analysis of Experimental Results

Our experimental results demonstrate that oil droplets stabilized with FeNPs will not foul the membranes under our reported experimental conditions. The NPs prevent direct oil-oil interaction between adjacent oil drops as well as oil-membrane interactions, which prevents drop coalescence as well as membrane wetting by the oil. [22–25] The theoretical framework we developed connects the force that holds the NPs at the oil/water

interface to forces resulting from the crossflow filtration of the emulsion (detailed explanation in Appendix Section 3.6.3). The force that holds the NPs at the oil/water interface of a Pickering emulsion is a result of surface energy minimization (*i.e.* interfacial energy) (Equation A3.1). [45,46] The interfacial energy can be used to calculate the force that holds the particles in place (Figure 3.4a) (Appendix Section 3.6.3.2, Equations A3.2-3). This allows us to perform a force balance, which determines if the particle will remain at the interface under various forces acting on the system during filtration (*e.g.* pushing, pulling or rolling force) (Figure 3.4b).

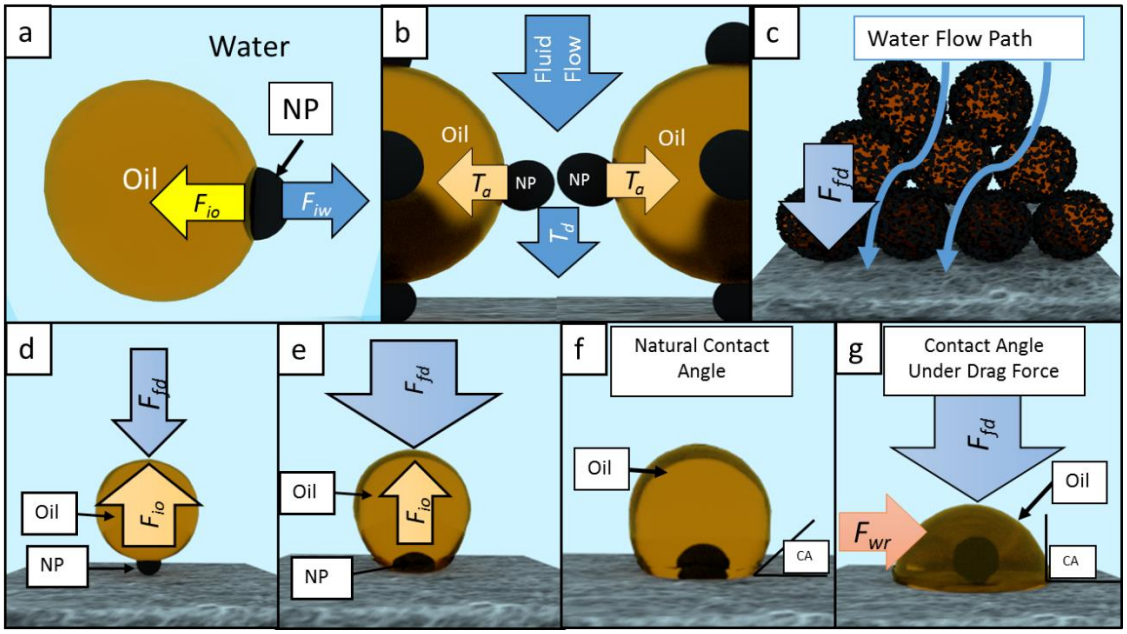

Figure 3.4: (a) The model uses a single NP at the oil/water interface to calculate the force required to either pull the NP out of the drop (F_{iw}) (blue arrow) or push the NP into the oil drop (F_{io}) (yellow arrow). (b) The shearing forces acting on the NPs in the cake layer are shown; the fluid flow through the cake layer generates a rolling torque that acts on the particles (T_d), with an adhesive torque (T_a) (holding the particle in place) preventing the particle from rolling off the oil surface. (c) The flow through the cake layer results in a non-linear flow path, which exerts a drag force (F_{fd}) on the surface of the Pickering emulsion drops. The drag force transfers from the top layer to the bottom layer, leading to a force (F_{fd}) that has to be supported by the lowest Pickering emulsion drops in the cake layer. (d) The drag force (F_{fd}) pushes the oil drop into the NP, and the interfacial force (F_{io}) acts against it, preventing oil from coming in contact with the membrane. (e) When the drag force (F_{fd}) is stronger than interfacial force (F_{io}), the NP enters the oil phase, allowing oil to come in contact with membrane. (f) When oil comes in contact with membrane it wets the surface to the oil's natural contact angle with the membrane surface. (g) The oil spreads due to the drag force (F_{fd}), leading to a higher contact angle than the natural contact angle, which leads to further membrane wetting and fouling.

The model first considers the stability of the Pickering emulsion in a cake layer that formed on the membrane surface during cross-flow filtration. The cake layer is a complicated structure that generates a large number of forces that act on the Pickering emulsion and membrane surface. We first consider the forces that prevent oil coalescence,

as coalescence would lead to membrane fouling. The force profiles acquired from the AFM study demonstrate that the NP layer on the oil drop surface is mobile, and moves under the application of an external force (Supplemental Section S1). Thus, forces resulting from fluid flow through the cake layer could potentially cause NP movement along the oil drop surface, which can lead to oil from neighboring drops to coalesce and lead to fouling. The model then assumes the presence of two NPs that are placed between two oil drops, preventing the oil in adjacent drops from interacting (Figure 4b). The fluid drag through the cake layer would result in a rolling torque (T_d) that would try to roll the particle off the oil surface (Equations A3.4, A3.8-A3.10). [47–51] An interfacial force (F_{iw}) that holds the NP at the oil/water interface generates an adhesive torque (T_a) that prevents the particle from rolling off the surface (Equations A3.5-A3.7). [45,47,49] If the particles were to roll off the oil drop surface, the oil in neighboring drops would be exposed, which would lead to coalescence and fouling. Thus, a simple torque balance allows us to determine if coalescence would occur. In our model, if a coalescence event occurs then we assume the membrane will foul. A detailed procedure for the calculation of the torque balance is presented in Appendix Section 3.6.3.3.

The fluid flow through the porous structure of a cake layer leads to a drag force (F_{fd}), which has to be supported by the Pickering emulsion structure, and in particular, by the bottom layer of the Pickering emulsion that is in contact with the membrane (Figure 3.4c). The fouling here is mitigated by a layer of NPs that prevent oil from coming in contact with the membrane surface. A force balance is then performed around a single NP that separates the oil drop from the membrane surface (Figure 3.4d). The interfacial force

(F_{io}) that holds the particle at the oil/water interface has to resist the drag force acting on the cake layer, preventing the particle from entering the oil phase (Equations A3.3b, A3.11). If the drag force through the cake layer is lower than the interfacial force holding the particle at the oil/water interface, then the membrane will not foul. Otherwise, the oil can come into contact with the membrane, and we must consider the susceptibility of the membrane material to wetting (Figure 3.4e). A detailed procedure for calculating the forces acting on a particle separating the oil from the membrane is presented in Appendix Section 3.6.3.4.

The drag force acting on the cake layer can force the oil drops to be exposed to the membrane surface and come directly in contact with it. The oil can then wet the membrane surface to its natural energetic minimum (*i.e.* its measured contact angle); further membrane wetting requires an external force to be applied to the drop (Figure 3.4f, g). In the cake layer, a drag force (F_{fd}) provides this external force, which acts against the membrane natural resistance to wetting (F_{wr}); if $F_{fd} > F_{wr}$ then the oil is forced to spread further across the membrane surface (Figure 3.4g) (Equations A3.11-A3.14). [52] We assume that to completely wet the membrane, a contact angle of 90° is required, since at this angle oil from adjacent drops would come in contact at the edges, which would then lead to coalescence and fouling. A detailed procedure for calculating the force balance and determining oil spreading is presented in Appendix Section A3.6.3.5.

The overall model can then be solved in several steps (Figure 3.5a) if the following information is known: the contact angle of the NPs with oil and water; the contact angle of the membrane with oil; the permeate flux and pressure drop across the cake layer (Figure

3.5a). The first step in the model is to determine if coalescence in the cake layer would take place. If coalescence does occur then the membrane will foul under the specified conditions. If coalescence does not occur, then it is determined if the drag force through the cake layer is sufficient to push the NPs into the oil drop, which leads to the oil coming in contact with the membrane surface. If the oil does not come in contact with the membrane surface then no fouling occurs. If the oil comes in contact with the membrane surface, then it has to be determined if the membrane will be wetted with oil, which would lead to membrane fouling. This simple theoretical framework allows for the determination of the important operational conditions under which the membrane could foul. A detailed description of this process is presented in Appendix Section A3.6.3.6.

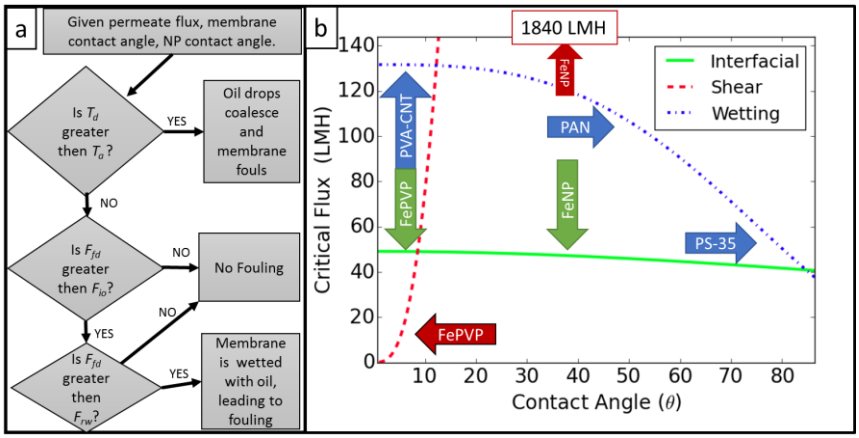

Figure 3.5: (a) Theoretical framework flow chart. (b) Model results demonstrating the relationship between the critical permeate flux (y axis) and membrane and NP contact angle (x axis): the interfacial (green) line shows the solution to the force balance for the fluid drag force (F_{fd}) and the interfacial force (F_{io}), while the shear (red) line represents the torque balance between the fluid drag torque (T_d) and the torque of adhesion (T_a). Both lines are showing a solution for the critical flux vs. NP contact angle. The wetting (blue) line shows the force balance between the fluid drag force (F_{fd}) and the membrane wetting resistance (F_{wr}), solved for the critical flux vs. membrane contact angle. The PVA-CNT, PAN and PS-35 arrows point to the membrane contact angles, and the FePVP and FeNP arrows point to the NP contact angles.

3.3.4 Model Results

The theoretical framework developed for this work successfully captured the relationship between Pickering emulsion stability, membrane oleophobicity, and permeate flux. Experimental results demonstrate the significant difference between the FeNP and FePVP-stabilized oil drops under filtration conditions (Figure 3.3a, b), which prompted the investigation of the stability of the NPs at the oil/water interface. Thus, the first step is to understand the relationship between NP contact angle and Pickering emulsion stability when exposed to the shear forces found in the cake layer accumulated on the membrane surface, with the goal of finding the flux point where membrane fouling would occur (*i.e.* the critical flux). Model results (generated using Equations A3.1-A3.10) indicate that NPs with water contact angles <10° readily shear off the oil/water interface, leading to oil drop coalescence and membrane fouling, at fluxes above 40 LMH. Thus, the FePVP particles (with a contact angle of 6.8°) shear off at fluxes exceeding 26 LMH (critical flux of 26 LMH) (Figure 3.5b). In contrast, the FeNP particles, having a water contact angle of 40°, are very resistant to shear forces, requiring a flux of 1840 LMH to be sheared away from the oil/water interface. (Figure 3.5b) To verify the framework results additional experiments were performed using γ-Fe_2O_3 (γ-FeNP) and polystyrene sulfonate modified γ-FeNP (FePSS) nanoparticles with contact angles of 10±2° (critical flux of 76 LMH) and <5° (critical flux of 12 LMH), respectively. (Figure A3.1, and A3.5) The experiments revealed that FePSS stabilized oil fouled in a very short time when operating at 50 LMH, while the γ-FeNP stabilized oil began fouling at operating flux of 80 LMH, demonstrating the reliability of the proposed theoretical framework. Thus, during filtration experiments it

is likely that the shear forces in the cake layer stripped the FePVP from the oil drops, allowing the membrane to foul (Figure 3.3a). However, these forces were insufficient to remove the FeNPs from the oil/water interface, which leads to the conclusion that another mechanism is responsible for the observed fouling at 100 LMH on the relatively oleophilic PS35 and PAN membranes (Figure 3.3b).

Using Equations A3.1-A3.3 and A3.11, it was found that the pressure drop across the cake layer in our system would cause the FeNPs separating the oil from the membrane to be "pushed" into the oil drop itself, and allow the oil to come into contact with the membrane, when fluxes exceeded 48 and 46 LMH for the FePVP and FeNP, respectively (Figure 3.5b). The slightly higher critical flux for FePVP is due to their higher hydrophilicity, which increases the energy barrier preventing the FePVP particle from partitioning into the oil drop. The relatively small change in the critical flux is due the fact that the total difference between the energy barriers is relatively small compared to the overall energy barrier (1.346e7 kT vs 1.365e7 kT for FeNP and FePVP respectively, Figure A3.1). This higher energy for partitioning into the oil also leads to a smaller energy barrier existing for the particle to be pulled out of the oil drop. However, this difference is very significant with the energy barrier being 165 kT for FePVP and 1.83e5 kT for FeNP (Figure A3.1). Equations A3.11-A3.14 were used to determine whether the membrane material, once in contact with the crude oil (if the NPs at the oil/membrane interface are pushed into the oil drop itself), would wet. To do so, F_{wr} was compared to the force experienced by the bottom-most oil drop in the cake layer (derived from the pressure drop across the cake layer – F_{fd}). The results of the model demonstrate that the critical flux for the PVA-CNT

membranes is 131 LMH, which would lead to no fouling at fluxes of 50 and 100 LMH, as was experimentally observed (Figure 3.5b). The critical flux for PAN and PS35 was found to be 105, and 50 LMH respectively, with experimental results demonstrating fouling at 100 LMH for both membranes (Figure 3.3a, b).

Finally, the results of the various model components can be compared to our experimental results using the theoretical framework described in Figure 5a, for the purpose of understanding the mechanisms responsible for the observed fouling phenomena. Since the PAN membrane fouled when treating the FePVP-stabilized oil at 50 LMH but not when treating the FeNP-stabilized oil, it is likely that the fouling mechanism involved the shearing of the FePVP particles from the oil/water interface, as predicted by the model (Figure 3.3a, b). At higher fluxes (100 LMH), the PS35 and PAN membranes both rapidly fouled, in contrast to the PVA-CNT membranes, which are significantly more oleophobic, that did not foul, (Figure 3.2, 3.5b). The model predicts that the relatively hydrophobic PS35 and PAN membranes will become wetted by the crude oil if the oil comes into contact with the membrane surface at fluxes of ~100 LMH. Furthermore, the model predicts that at a flux of 100 LMH, the force acting on the cake layer is sufficient to push the NPs into the crude oil drop, thus allowing contact between the oil and membrane surface. Therefore, the mechanism responsible for the fouling of the PS35 and PAN membranes at 100 LMH is wetting by the oil. Additionally, the mechanism responsible for the fouling of the PVA-CNT membranes when filtering the bare oil emulsions (no NPs; Figure A3.4) is the lateral coalescence of oil drops in the cake layer, since there are no NPs separating neighboring drops.

3.3.5 Nanoparticle Recovery and Reuse

The magnetic properties of the NPs used to prepare the Pickering emulsions provide an opportunity to recover the NPs from the concentrated crude oil in the membrane concentrate stream, through the application of an external magnetic force. It has been previously demonstrated that Pickering emulsions prepared with micron-sized particles could be easily separated from oil using a strong magnetic force. [22] However, it was also found that NPs adhere strongly to the oil/water interface and do not undergo spontaneous separation like their larger counterparts. [23] We found that the Pickering emulsion can be readily separated from the aqueous phase using a strong magnet (N48 rare earth magnet). Following exposure to air the oil readily seeps out under gravity, leaving the NPs attached to the magnet (Figure 3.6a). However, gravity separation was found to be insufficient for FeNP reuse due to significant amounts of oil remaining in the FeNP slurry (70-80 %), which prevented their effective dispersion in water. Thus, a wicking step was added to the separation and recovery process, where the oil was wicked out of the FeNPs using blotting paper (Figure 3.6b, c). This approach reduced the oil content in the FeNP slurry to 31±6 % of the initial crude oil weight, producing a nearly dry FeNP powder that readily formed new Pickering emulsions (Figure 3.6d). The process of recovery and reuse was repeated three times, with no apparent drop in the FeNP's ability to form new Pickering emulsions. The recovery and reusability of FeNPs allows for the development of a continuous, membrane-based and fouling-free oily water treatment process. Such a process would stabilize oil emulsions with FeNPs, forming Pickering emulsions that would be concentrated with UF, producing oil-free water. The concentrated Pickering emulsions

would then go through a magnetic separation process producing a FeNP slurry that could be reused (*i.e.* form new Pickering emulsions), and a highly concentrated oil stream (Figure 3.6e).

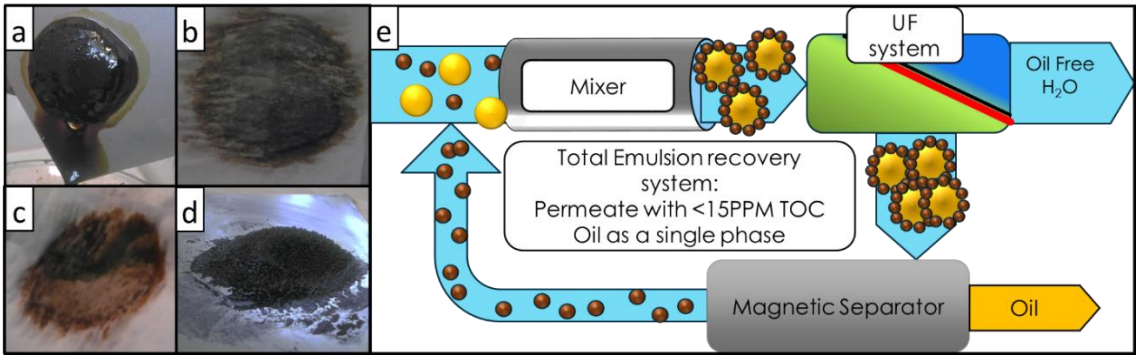

Figure 3.6: Magnetic NP recovery process: (a) after recovering the Pickering emulsion from water and exposing to air, oil readily seeps from the NPs. (b) Blotting paper used to wick oil from the NPs. (c) Oil that was wicked out of FeNPs is shown on the blotting paper. (d) Recovered nano particles are seen in their dry-like state. (e) Complete oil emulsion treatment system - starting from the top left, oily water enters a mixer with FeNPs to form a Pickering emulsion; the Pickering emulsion enters the UF system, where it is concentrated to produce an oil-free permeate stream, and a concentrated stream; the concentrated Pickering emulsion is passed into a magnetic separator, which separates water and FeNPs from oil, producing an oil stream and an FeNP slurry that is reused for the formation of a new Pickering emulsion (brown dots are FeNPs and large yellow dots are oil droplets).

3.4 Conclusions

The coupling of Pickering emulsions to underwater superoleophobic UF membranes allows for a rapid and robust oil/water separation method (up-to 100 LMH) for water contaminated with large quantities of crude oil (up-to 100 ml/L) with minimal fouling. The novel process reported here is insensitive to solution ionic strength (>2 M), temperatures (2-25°C), and produces treated water with a TOC content <15 ppm regardless of oil concentrations in the feed. The 15 ppm threshold is critical, as this is the level

considered acceptable for environmental discharge for treated water. [53] The developed theoretical framework and model explain our experimental results, indicating that fouling inhibition is due to the non-coalescing nature of Pickering emulsions as well as membrane underwater superoleophobicity that prevents oil wetting of the membrane surface. Importantly, our work demonstrates that an underwater superoleophobic membrane alone is insufficient to prevent membrane fouling under realistic conditions. Finally, we have demonstrated that crude oil could be separated from FeNPs using an external magnetic field coupled to a wicking process, which allows for their recovery and reuse.

The process developed here has significant implications for oily water treatment, as it allows for rapid handling of concentrated oil streams, while producing very high quality treated water, without experiencing membrane fouling. The advantage of UF over other oil/water separation techniques is the tight membrane pore size, which guarantees an oil-free permeate that can be easily reused or disposed of. The fact that the system does not foul will prevent excess costs associated with UF cleaning and process interruption. Membrane fouling leads to increased power demands with the expected power usage for non-fouled membranes being less than 0.2 kWh/m^3 or $\$0.013/m^3$ (based on average industrial power cost in the USA in 2014). [54,55] The addition of CNTs to fabricate the underwater superolephobic membranes used in this study incurs a relatively minor additional cost of $\$2.21/m^2$, which amounts to an 11 % increase compared to the cost of the PS35 polysulfone membrane material. Finally, we estimate that the energetic cost of magnetic separation would only be 0.00411 kWh/m^3 (0.000275 $\$/m^3$), amounting to less

than 2 % of total energy consumption (based on MSK-300 magnetic separator (PRAB, Kalamazoo, Michigan)).

3.5 Methods

3.5.1 Materials

FeNPs were purchased from SkySpring Nanomaterials, Inc. (Houston, TX) and had a black appearance and a reported diameter of 20-40 nm. The FePVP particles were purchased from US Research Nanomaterials, Inc. (Houston, TX), had an orange appearance, a reported PVP loading of 1 % and a diameter of 20-40 nm. The γ-FeNP particles were purchased from US Research Nanomaterials, Inc. (Houston, TX), had an orange appearance and reported diameter of 20-40 nm; these NPs were used as-is. Polystyrene sulfonate sodium salt with Mw of 70,000 was purchased from Scientific Polymer Products(Scientific Polymer Products, inc, Ontario, NY). FePSS particles were prepared by mixing 20 grams of γ-FeNP and 15 grams of PSS in 1 L of DI water. The pH of the suspension was adjusted to 4.0 using HCL, and was then sonicated in a sonication bath, while being mixed with an immersion mixer for 30 minutes. The solution was then mixed for additional 18 hrs, after which the FePSS particles were removed from the suspension using vacuum filtration and a polyethersulfone membranes (100 nm) (Membrana, Tokyo, Japan). The particles were then flushed with 3 L of DI water with mixing, and then dried at room temperature for 48 hours before being used. The SPW was made with 1.27 M NaCl, 0.165 M MgCl2, 0.018 M KCl, 0.17 M CaCl, and 0.004 M MgSO4, while SSW was prepared with 0.68 M NaCl, 0.03 M MgCl2, 0.013 M CaCl, and 0.019 M MgSO4 all acquired from Fisher Scientific (Thermo Fisher Scientific Inc,

Waltham, MA); the salts were all ACS grade. The Crude Oil was purchased from Texas Raw Crude (Midland, TX). PS-35, and PAN membranes were acquired from Sepro Membranes (Sepro Membranes Inc., Oceanside, CA) and used as is. The PVA-CNT membranes were synthesized using a method described elsewhere. [34] Briefly, a solution of 1 % 146,000-186,000 MW PVA (Sigma-Aldrich) and multi-wall carbon nanotubes functionalized with carboxylic groups (Cheaptubes Inc., Brattleboro, VT) was prepared in a 3:1 w/w ratio. The mixture was pressure filtered (Millipore; Billerica, MA) onto either a PS35 or PAN support with a final CNT loading of 0.63 g/m^2. The composite membrane was then cross-linked in a heated bath (90°C for 1 hour) containing 1 g/L of 50 wt% Glutaraldehyde and 0.37 g/L hydrochloric acid (Thermo Fisher Scientific Inc, Waltham, MA), followed by a drying step in an oven (90°C for 10 minutes).

3.5.2 Sample Preparation

Crude oil emulsions were prepared by adding crude oil to 1.5 L of water (DI, SPW or SSW) followed by vigorous mixing using a blender (Oster, Sunbeam Products, Inc. USA) set at maximum speed for 10 minutes. The temperature of the solution during the blending was maintained at room temperature using an immersed cooling coil. The prepared emulsion was used as is, unless it was used for the Pickering emulsion preparation. The Pickering emulsion was prepared by adding FeNPs or FePVP particles to the oil emulsion in a 1:1 (vol/w) ratio, followed by mixing with an immersion mixer (built in house) for 1 or 3 hour respectively.

3.5.3 Material Characterization

FeNP and FePVP aggregate size was measured by preparing a 10 mg/L solution in DIW, and measuring the size using a DLS instrument (Brookhaven Instruments; Holtsville, NY) with the detector angle set at 90°. The oil emulsion and Pickering emulsion sizes were measured using optical microscopy images (Thermo Fisher Scientific Inc, Waltham, MA) and image analysis software (ImageJ); a 0.01 mm calibration slide (AmScope, Irvine, CA) was used to ensure accurate size measurements, with at least 150 oil/Pickering emulsion drops measured. The PVA-CNT films were imaged using SEM (SEM; FEI XL30 SEM-FEG; Hillsboro, OR). SEM samples were attached to an aluminum stub using copper tape. Cross sectional SEM images were acquired by freezing membranes at -80°C and then fracturing the surface. Membranes were then sputter coated with Pt/Pd for 30 seconds. The SEM image of the Pickering emulsion was acquired by placing drops of Pickering emulsion solution onto the aluminum stub and allowing the sample to dry at room temperature overnight, the samples were then sputter coated with Pt/Pd for 40 seconds. Crude Oil Contact angle measurements were taken using a contact angle goniometer (Attension; Linthicum Heights, MD) equipped with a polycarbonate inverse cell, where the membrane was attached using Scotch double sided tape (Scotch, Minneapolis, MN), and immersed in DI water for 5 minutes before allowing a 10 μL oil drop to come in contact with the membrane surface. FeNP and FePVP samples for contact angle measurements were prepared using a method modified from Potapova et al. [56–58] In short, 0.1 g/L of FeNP, γ-FeNP, FePSS and FePVP powder were added to 500 ml of DIW and sonicated for 30 min using a horn sonicator (Branson; Danbury, CT). The suspension was then pressure

deposited onto a PS35 support at 50 psi and dried at room temperature overnight. The contact angle of the prepared sample was measured with a 0.6 μL water drop in air (Attension; Linthicum Heights, MD).

3.5.4 Filtration System and Fouling Experiments

The filtration experiments were performed with a fully automated membrane filtration system described in more detail elsewhere. [59] Briefly, a cross flow filtration cell was used, the permeate flow rate (flux) was measured using a scale, and was maintained by adjusting system pressure via an electronically controlled valve. Due to the abrasive nature of the NPs being used, different pumps had to be used as they failed over time, with a diaphragm pump (Hydra-Cell, Wanner Engineering, Inc, Minneapolis, MN) and a progressive cavity pump (Moyno, Springfield, OH) proving themselves as the only viable options for long-term operations. Other pumps used for short periods included a gear pump (Coleparmer; Vernon Hills, IL), and a rotary vane pump (McMaster-Carr, Chicago, IL). For low temperature experiments, an immersion coil attached to a chiller (Thermo Fisher Scientific Inc, Waltham, MA) was inserted into the solution tank, and a custom PID controller (Arduino) with a temperature probe in the solution tank was used to maintain constant feed temperature to ± 0.25°C.

All membranes were compressed with DIW at 100PSI for 12-48 hours until constant flux was achieved before experiments began. During the filtration of the Pickering emulsions, the system was operated continuously for 12 hours at which point a five minute cross-flush cleaning event with the feed water (no pressure) was performed; following the cleaning event, the experiment was resumed. Unless otherwise stated, membrane permeate

was returned to the feed tank to maintain constant feed concentrations. During the concentration experiments, the permeate was not returned to the feed and the concentration of the oil was monitored by measuring the volume of permeate produced.

3.5.5 NP Recovery and Reuse

For the FeNP recovery experiments, the Pickering emulsions were prepared by adding 100 ml/L of crude oil to 30 ml DIW in a 40 ml glass vial followed by sonicating in a bath (Thermo Fisher Scientific Inc, Waltham, MA) for 10 minutes. A 1:1 (v/w) ratio of FeNPs was then added to the vial and vigorously mixed using a vortex mixer (Thermo Fisher Scientific Inc, Waltham, MA) for 1 minute. The solution was then transferred to an aluminum boat (42 ml volume, Fisher Sci.) and placed on top of a cylindrical 1" x 1" N48 neodymium magnet (CMS Magnetics, Garland, TX). The magnet and boat were tipped over perpendicular to the bench, allowing the draining of the water and crude oil, leaving behind a FeNP cake. The FeNP cake was then mixed with a spatula, and Kimwipes (Kimberly-Clark Worldwide, Inc.) were softly pressed against the cake to absorb residual moisture and crude oil, with the wicking process repeated 4-5 times. The alumina boat was then weighted, and a 0.1 g sample was removed and placed on a different aluminum boat, which was then dried at 50 °C for 30 minutes, weighed, and placed on the N52 magnet once again. Crude oil was then extracted from the 0.1 g sample using 3 consecutive washes with 10 ml of Hexane (99% Hexanes, Fisher Sci.). The sample was then allowed to dry at 50°C for 10 minuets and was weighed one last time, the difference between the dried sample weight, and the weight after the hexane wash was used to calculate entrapped oil content in the FeNPs. The reusability of the FeNPs was tested by using the recovered

FeNPs (described previously) to stabilize a fresh oil emulsion solution. The same process was followed as above, however, the volume of oil emulsion was adjusted such that the total oil volume of oil emulsion + oil remaining in the NPs would result in a 1:1 (vol/w) ratio. The same FeNPs were reused for a total of 3 times, and the overall procedure was duplicated with fresh FeNPs. The oil stabilization was tested by measuring the TOC in the recovered water after magnetic separation, and was always bellow 15 ppm, indicating full stabilization.

3.5.6 Atomic Force Microscopy

Samples for AFM probing were prepared by vortex mixing 0.003 ml/L oil emulsion in a glass vial for 5 minuets. A glass slide was then held parallel to the bench surface, and 1 ml of the oil emulsion was deposited (using a pipette) on the underside of the glass slide, with the oil emulsion forming a small water drop on the bottom of the glass slide. The slide was allowed to stabilize for 5 minutes while the oil floats towards the top of the slide and attaches to the glass surface. Then, the slide was carefully inverted and the emulsion solution was replaced with DI water and placed onto the AFM stage (Asylum Research, Santa Barbara, CA). The FeNP stabilized oil droplets were prepared by first coating the slide in oil droplets as described above, and then replacing the DI water with a 0.1 g/L FeNP suspension that had been sonicated with a horn sonicator (Branson; Danbury, CT) for 10 min. The FeNP suspension was allowed to settle onto the oil-coated glass surface for 10 minuets, and was then flushed out with DI water. For the force probing, triangular tipless tips were used (NP-O10, Bruker, Camarillo, CA) with a reported stiffness of 0.12 N/m. For force measurements, the tips were immersed into a 10 g/L dopamine solution for

10 minutes before use. The tips were then calibrated by first acquiring the slope from probing the glass surface, (getting the V/nm sensitivity) and then by performing a thermal tuning step (measured stiffness values being 0.10±0.01 N/m). To probe the oil drop surface, the tip was aligned over the oil drop using an optical microscope, and then manually lowered onto the surface until the tip engaged. A force profile was then taken with a trigger point being set at 35 nN at a rate of 250 nm/s.

3.6 Appendix

3.6.1 Additional Data Figures

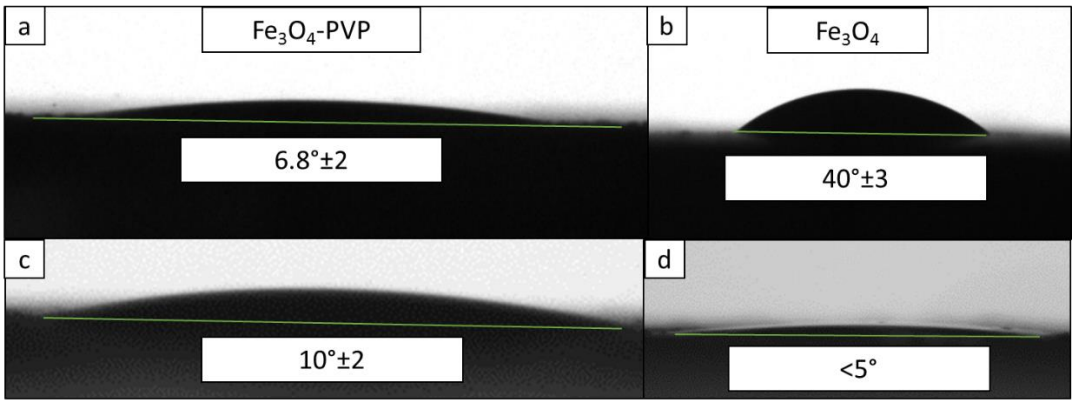

Figure A3.1: Water contact angle images of FePVP (a), FeNP (b), γ-FeNP (c), and FePSS (d).

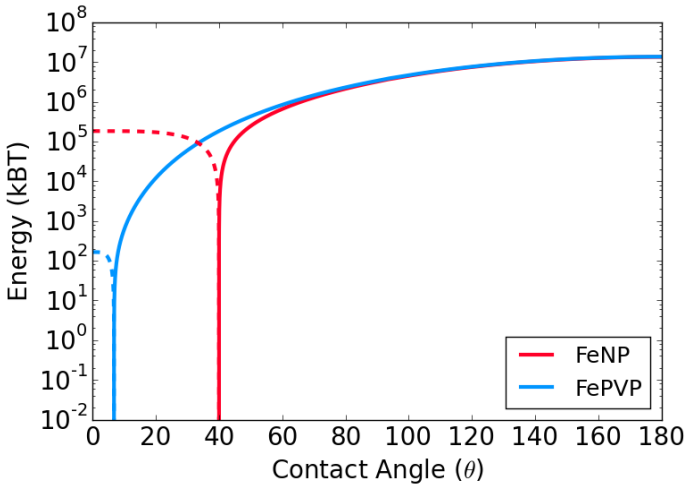

Figure A3.2: Energy wells for FeNP (contact angle of 40°) and FePVP (contact angle of 6.8°) entering (dashed lines) and leaving (solid line) the water/oil interface.

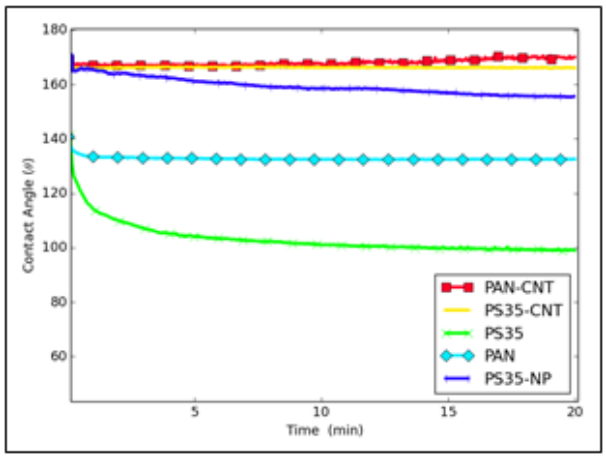

Figure A3.3: Temporal changes of crude oil contact angles with various membranes surfaces.

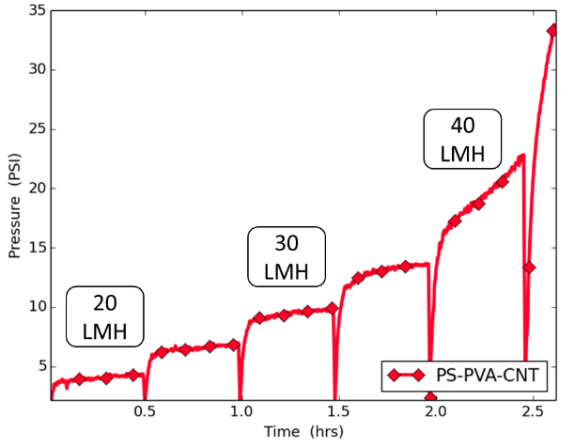

Figure A3.4: Required pressure to maintain a set flux was recorded for a system containing 0.5 ml of crude oil in 1 l of DIW, Starting at 20 LMH and increasing in 5 LMH steps (cross flow 10 cm/s)

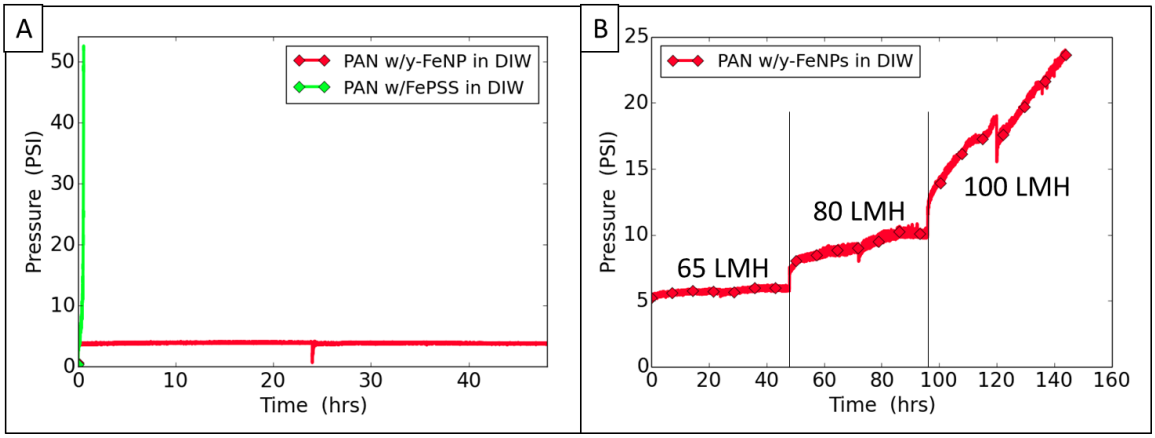

Figure A3.5: Membrane performance while treating with FePSS and γ-FeNP stabilized crude oil at 50 LMH (a) and fouling of γ-FeNP at 65, 80 and 100 LMH (b) with a cross flow velocity of 15cm./s.

3.6.2 AFM Force Curves:

Based on the theoretical framework, the key to fouling inhibition is the prevention of oil drop coalescence and oil drop wetting of the membrane surface. In an attempt to understand the behavior of an FeNP-stabilized oil drop during filtration conditions, which

expose the stabilized drop to forces acting on the oil drop surface, an AFM tip was used to exert a force on the oil drop surface. During the probing of the crude oil drop it was found that the approach and retraction curves were identical, and no significant hysteresis was observed indicating no adhesion of oil to tip surface (Figure A3.6). Probing the crude oil drop in SPW was impossible due to the oil drop adhering and wetting the probe. This drastic difference is explained by the presence of an electrostatic repulsive force that prevents the tip from being wetted in DI water. However, in SPW, the electric double layer around the oil drop and the tip collapse, which allows the tip to come in contact with the oil followed by wetting. The FeNP coated oil droplets revealed significantly different approach and retraction curves (Figure A3.6). The approach force curves of the coated oil droplets reveal jagged-like features, which are not found in non-coated oil droplets. These jagged features are due to the movement and rearrangement of the FeNP coating as the tip approaches the oil drop surface. [60] Unlike the uncoated crude oil droplet that we were not able to probe in SPW, we were able to probe the oil droplets coated with FeNPs, as the tip was physically separated from the oil drop, which prevented wetting. In SPW, the approach curves once again revealed a clear jaggedness, indicating that there is some rearrangement of the FeNPs on the surface of the oil drop.

To study the rearrangement of the NPs at the oil/water interface, the NP-stabilized drops were repeatedly probed (for a total of 16 times). It was observed that the approach profiles for FeNP coating in DI water changed with each probing, with the jaggedness continuously reduced, indicating a more stable packing of the FeNP layer (Figure S7a). The repeated probing of the FeNP coating in SPW water does not exhibit a significant

change in overall jaggedness of the approach curve when compared to DI water results (Figure S7b). This seems to indicate that the FeNPs in SPW water do not readily rearrange, with this lack of rearrangement likely due to strong aggregation of the FeNP particles at the oil/water interface due to the collapse of the electrostatic repulsive forces between the particles; this aggregation then leads to reduced FeNP mobility, which prevents their repacking.

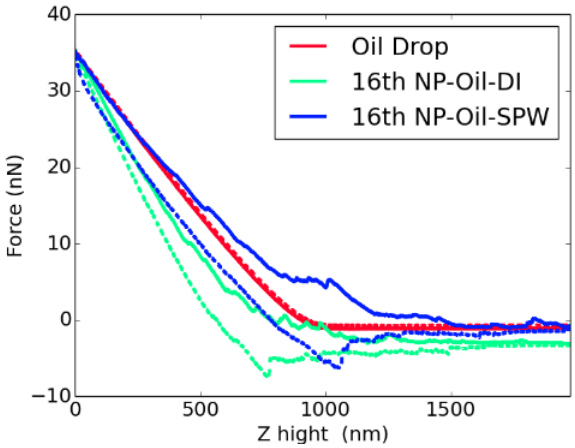

Figure A3.6: Force curves for a crude oil droplet, and final probed curves for FeNP-stabilized oil droplet in DI and SPW waters

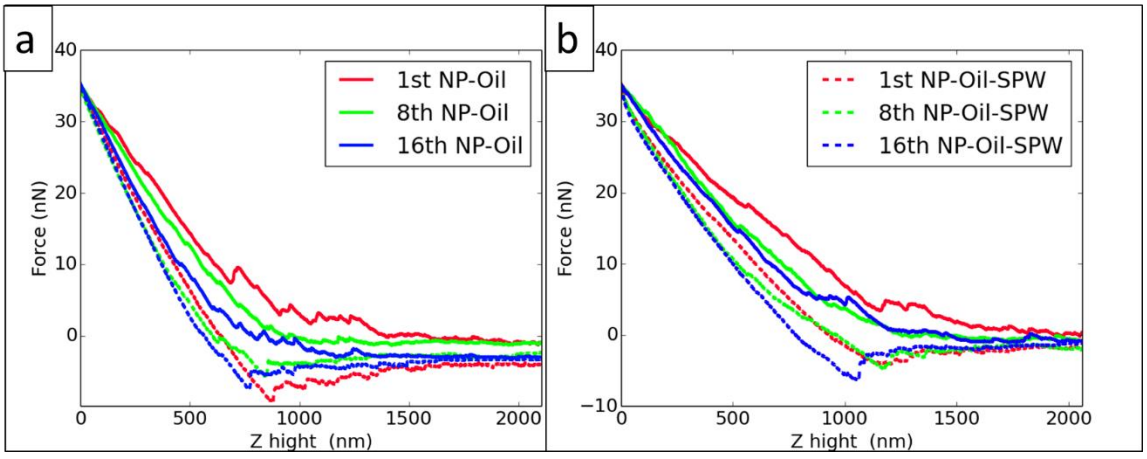

Figure A3.7: Change in force curves with number of probes, showing 1st, 8th and 16th probing in (a) Di water and (b) SPW.

3.6.3 Theoretical Background and Details

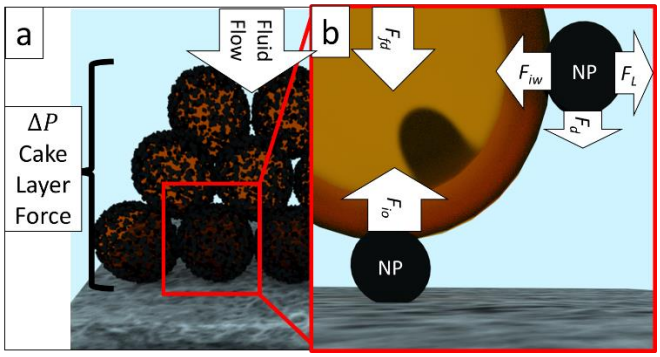

Figure A3.8: Forces in cake layer along membrane surface. (a) In the cake layer, the total drag of fluid through the cake is the total cake layer force acting on the lowest layer of oil droplets. (b) The forces acting on NPs stabilizing an oil drop.

3.6.3.1 Theory overview

During cross-flow filtration, compounds in the water (e.g. Pickering emulsions) that cannot pass through the membrane will accumulate, forming a cake layer on the membrane surface (Figure A3.8a). [61,62] In a cake layer composed of a Pickering emulsion, oil drops are coated with NPs that prevent the oil from coalescing. [22–25] In addition, the NPs also prevent the oil from coming in contact with the membrane surface itself (Figure A3.8b). In an idealized system, a single oil drop has two NPs on its surface, one separating the drop from the membrane surface, and another on the side of the oil drop, which prevents neighboring oil drops from coalescing (Figure A3.8b). As the NP that is on the side of the oil drop is responsible for preventing oil drop coalescence, its removal would result in coalescence, film formation and consequent membrane fouling. Similarly, if enough force is applied to the top of the oil drop, the NP that is separating the oil drop from the membrane surface will be pushed into the drop itself, allowing oil to come into contact with the membrane surface, which could lead to the oil wetting the membrane surface and to

membrane fouling. In this theoretical framework, the forces acting on the NPs and oil drops are calculated, and a force balance approach is used to determine the point at which membrane fouling occurs.

3.6.3.2 Interfacial force

The interfacial force (F_i), which holds the NPs at the oil/water interface, prevents the NP from being pulled out of/pushed into the oil drop. To calculate this force, the interfacial free energy of a particle entering the oil/water interface (f_i) is calculated (A3.1a-d): [45,46]

$$f_i = 2\pi\gamma_{ow}[r^2(1 \pm \cos(\alpha))\cos(\theta_{ow}) - R_{II}^2(1 - \cos(\beta))] \qquad \text{(A3.1a)}$$

$$\alpha = \arcsin\left(\frac{x}{r}\right) \qquad \text{(A3.1b)}$$

$$\beta = \arcsin\left(\frac{x}{R_{II}}\right) \qquad \text{(A3.1c)}$$

$$x = \frac{rR_{II}\sin(\theta)}{\sqrt{r^2+R_{II}^2+2rR_{II}\cos(\theta)}} \qquad \text{(A3.1d)}$$

where γ_{ow} is oil surface tension, θ_{ow} is the particle contact angle with the oil (in radians), r is particle radii (average NP aggregate radius of 325 nm was used Fe_3O_4 nanopowder (FeNPs) and polyvinylpyrrolidone-coated Fe_3O_4 nanopowder (FePVP)), R_{II} is the oil drop radii (3.3μm diameter found from optical microscopy imaging), and the sign in the parenthesis is [–] for $\theta_{ow} < 90°$ and [+] for $\theta_{ow} > 90°$. Using the particle immersion depth (p_d) calculated from Equation A3.4, the interfacial force (F_i) which holds the particle at the oil/water interface can be found using numerical methods by taking the derivative of the interfacial free energy vs. particle immersion depth in the oil phase (A3.2):

$$F_i = \frac{df_i}{dp_d} \qquad \text{(A3.2)}$$

The force needed to push the NP into the water phase (F_{iw}), or into the oil phase (F_{io}) can be found by calculating the difference between the interfacial free energy holding the NP at its preferential partitioning contact angle (preferential NP immersion depth) and the free energy at a contact angle at 0° (complete release of NP from oil surface) or 180° (when the NP is pushed into the oil phase), respectively (A3.3a, b):

$$F_{iw} = F_i(\theta_p) - F_i(0) \qquad \text{(A3.3a)}$$

$$F_{io} = F_i(180) - F_i(\theta_p) \qquad \text{(A3.3b)}$$

3.6.3.3 Shear forces in the cake layer

In the cake layer formed during the filtration of a Pickering emulsion, oil coalescence is prevented by NPs that are placed between neighboring oil drops. Since water is flowing through the cake layer (Figure A3.7a), these NPs will experience a drag force that is pulling them away from the oil/water interface. This force can be used to calculate the torque of drag (T_d) that will try to roll the particles off the oil droplet, while the adhesion torque (T_a) will try to keep the particles at the oil/water interface. [47,48] T_d can be calculated using the following equation (A3.4) [49], where r is the NP radii, and F_d is the force of drag:

$$T_d = 1.4F_d r \quad \text{(A3.4)}$$

The interfacial holding torque (T_a) can be calculated from Equation A3.5 [47]:

$$T_a = (F_{iw} - F_l)I \qquad \text{(A3.5)}$$

where F_{iw} is the interfacial force to the water phase (A3.11a), F_l is the lift force, and I is the NP and oil drop contact area that can be found from the classical Johnson, Kendall, and Roberts theory (Equation A3.6) [49]:

$$I = \sqrt{\frac{1}{\frac{1}{r}+\frac{1}{R_{II}}} * p_d} \qquad \text{(A3.6)}$$

where R_{II} is the oil drop radii, and p_d, the particle immersion depth in oil, can be calculated from the following equation (Equation A7) [45]:

$$p_d = r(1 + \cos(\theta_{ow})) \qquad \text{(A3.7)}$$

where θ_{ow} is the particle contact angle with oil. The lift and drag forces (F_l and F_d, respectively) can be found from equations (A3.8) and (A3.9), respectively [48] :

$$F_l = \frac{81.2\mu r^3 \left(\frac{dv}{dr}\right)^{\frac{3}{2}}}{v^{\frac{1}{2}}} \qquad \text{(A3.8)}$$

$$F_d = 10.205\pi\mu \left(\frac{dv}{dr}\right) r^3 \qquad \text{(A3.9)}$$

where μ is fluid dynamic viscosity, v is kinematic viscosity, and dv/dr is the shear rate, which can be calculated using constricted pore theory (A3.10a-f), where the flow through the cake layer can be represented by constricted pores: [48,50,51]

$$\frac{dv}{dr} = \frac{\frac{Q}{N_{pore}}}{\left(\frac{\pi}{4}\right)d_z^2} \frac{4(\frac{d_z}{2}-r)}{\frac{d_z}{2}} \qquad \text{(A3.10a)}$$

where Q is fluid flow rate through the pore and d_z is the pore diameter at the center of the pore (A3.10b-d):

$$d_z = 2\left(\frac{d_{max}}{2} + \left(4\left(\frac{d_c}{2} - \frac{d_{max}}{2}\right)\right)\right) \qquad \text{(A3.10b)}$$

$$d_{eff} = \frac{d_c}{0.470} \quad \text{(A3.7c)}$$

$$d_{max} = d_c 2.141 \quad \text{(A3.10d)}$$

where d_c and d_{eff} are the constriction diameter, and effective pore diameter, respectively (A3.10c, d). N_{pore} is the number of pores in the cake layer (A10e):

$$N_{pore} = \frac{A\varepsilon}{\left(\frac{\pi}{4}\right) d^2_{effctive}} \quad \text{(A10e)}$$

where A is area of the cake layer, and ε is cake layer porosity (assumed to be 0.26 for a perfectly packed bed of spheres).

3.6.3.4 Fluid drag in the cake layer

The cake layer is supported by the lowest layer of oil droplets in contact with the membrane surface. Thus, this layer has to support the cumulative fluid drag force created by water flowing through the cake layer. Using Darcy's law, and assuming laminar flow conditions, the cumulative fluid drag force is equivalent to a pressure drop created by the cake layer, and can be used to calculate the force acting on single oil drop (F_{fd}). Using equation (A3.11), the pressure drop across the cake layer (ΔP) can be converted to a force acting on a single droplet, where A is the area of the membrane surface, *#drops* is the number of oil drops supporting the cake layer, and F is the force of fluid drag created by the cake layer.

$$F_{fd} = \Delta P * \frac{A}{\#drops} = \frac{F_{fd}}{A} * \frac{A}{\#drops} \quad \text{(A3.11)}$$

In this model, we used the results from our experiments to calculate the cake layer pressure drop, and do not attempt to simulate the cake layer formation process. The idealized linear relationship between the cake layer pressure drop and permeate flux was

calculated from the average operating pressures from which pressure drop due to membrane resistance was subtracted. The average cake layer pressure was found to be 1±0.5 PSI and 3.95±0.2 PSI at 50 and 100 LMH, respectively.

3.6.3.5 Membrane wetting resistance

Finally, the membrane's ability to resist wetting by the oil (F_{rw}) is considered. Due to physical constraints, we assume that the full wetting contact angle of oil drops on a membrane surface is limited to 90°, as smaller angles would result in oil drop overlap and coalescence in the tightly packed cake layer. Thus, this calculation is only valid for conditions where oil droplets are prevented from coalescing, as when a Pickering emulsion is forced onto the membrane surface. The free energy of wetting (f_w), as derived by Schrader et al. (1995) from the Young-Dupre equation, can be found using equation (A3.12a): .[52]

$$f_w = 2\pi r_{dc}^2 \gamma_{ow} \left[\left(\frac{2a}{\sin(\theta)^{\frac{2}{3}}} \right) - a \right] \qquad \text{(A3.12a)}$$

where r_{dc} is the contact radius of the drop with the surface, γ_{ow} is the oil/water surface tension (assumed to be 0.05 Nm^{-1} average surface tensions of alkanes in water [33]), and θ is the contact angle of an oil drop with the membrane surface, which can be calculated using equation (A3.12b):

$$a = \frac{2}{1+\cos(\theta)} - \cos(\theta) \qquad \text{(A3.12b)}$$

where the contact radius can be found from equation (A3.13) where V_d is the drop volume (based on a radius of 3.3μm, found using optical microscopy for NP stabilized oil):

$$r_{dc} = \sin(\theta)\left(\frac{3V_d}{\pi((1-\cos(\theta))^2(2+\cos(\theta))}\right)^{\frac{1}{3}} \qquad \text{(A3.13)}$$

The resistance force to wetting (F_{wr}) can then be found by calculating the difference between the derivative of the free energy function vs. change in contact radius at 90° and the membrane-oil drop contact angle (A3.14):

$$F_{wr} = \frac{df_{wet}(90°)}{dr_{dc}} - \frac{df_{wet}(\theta)}{dr_{dc}} \qquad \text{(A3.14)}$$

3.6.3.6 Theory solution flow.

The theoretical framework can then be solved via a step-wise force comparison, as demonstrated in Figure 5a. The first step in the framework is to input a given permeate flux, membrane contact angle, and NP contact angle (parameters governed by the choice of materials and operating conditions). Once these values are known, it is possible to calculate the torque of drag (T_d) and interface holding torque (T_a); if $T_d > T_a$ then the NPs will be stripped from the oil droplets, exposing them and leading to coalescence. If $T_d < T_a$ then the interfacial force that holds the NP in the oil phase (F_i) must be considered relative to the fluid drag force created by the cake layer (F_{fd}). If $F_{fd} < F_{io}$ then there is no fouling (since the NPs are not pushed into the oil phase), and the oil drop will not come in contact with the membrane surface. However, if $F_{fd} > F_{io}$, then membrane susceptibility to oil wetting must be considered; if $F_{fd} > F_{rw.}$ then the membrane will become wetted by the oil and foul. Otherwise, the membrane will not become wetted by the oil and will not foul (for a given flux).

Table A3.1: Description of symbols used in the model

Symbol	Description
#drops	The number of oil drops supporting the cake layer
μ	Fluid dynamic viscosity
A	Area of the cake layer
d_c	The constriction diameter
d_{eff}	Effective pore diameter
dv/dr	The shear rate
d_z	Pore diameter at the center of the pore
F_d	Force of fluid drag
F_{fd}	Force generated by fluid flow through the cake layer
F_i	Force holding a particle at oil/water interface
f_i	Interfacial free energy of placing NP into oil/water interface
F_{io}	Force required to push NP out of oil/water interface into oil phase
F_{iw}	Force required to push NP out of oil/water interface into water phase
F_l	Lift force
F_{rw}	Force resisting membrane wetting
f_w	Free energy of wetting
I	NP and oil drop contact area
N_{pore}	Number of pores in the cake layer
p_d	Particle immersion depth
Q	Fluid flow rate through a pore
r	Particle radii
r_{dc}	The contact radius of the drop with the surface
R_{II}	Oil drop radii
T_a	Adhesion torque resulting from interfacial force
T_d	Torque of drag due to shear flow
V_d	Drop volume
γ_{ow}	Oil surface tension
ΔP	Pressure drop across the cake layer
ε	Cake layer porosity
θ	The contact angle of an oil drop with the membrane surface
θ_{ow}	Particle contact angle with the oil (in radians)
ν	Kinematic viscosity

3.7 References

1. Mohr, S. H., Wang, J., Ellem, G., Ward, J. & Giurco, D. Projection of world fossil fuels by country. *Fuel* **141,** 120–135 (2015).

2. Benes, J. *et al.* The future of oil: Geology versus technology. *Int. J. Forecast.* **31,** 207–221 (2015).

3. King, G. M., Kostka, J. E., Hazen, T. C. & Sobecky, P. A. Microbial Responses to the *Deepwater Horizon* Oil Spill: From Coastal Wetlands to the Deep Sea. *Annu. Rev. Mar. Sci.* **7,** 377–401 (2015).

4. *Produced Water*. (Springer New York, 2011).

5. Neff, J. M., Johnsen, S., Frost, T. K., Røe Utvik, T. I. & Durell, G. S. Oil well produced water discharges to the North Sea. Part II: Comparison of deployed mussels (Mytilus edulis) and the DREAM model to predict ecological risk. *Mar. Environ. Res.* **62,** 224–246 (2006).

6. Ekins, P., Vanner, R. & Firebrace, J. Zero emissions of oil in water from offshore oil and gas installations: economic and environmental implications. *J. Clean. Prod.* **15,** 1302–1315 (2007).

7. Zhang, F. *et al.* Nanowire-Haired Inorganic Membranes with Superhydrophilicity and Underwater Ultralow Adhesive Superoleophobicity for High-Efficiency Oil/Water Separation. *Adv. Mater.* **25,** 4192–4198 (2013).

8. Zhang, W. *et al.* Salt-Induced Fabrication of Superhydrophilic and Underwater Superoleophobic PAA-g-PVDF Membranes for Effective Separation of Oil-in-Water Emulsions. *Angew. Chem. Int. Ed.* **53,** 856–860 (2014).

9. Ju, J., Wang, T. & Wang, Q. Superhydrophilic and underwater superoleophobic PVDF membranes via plasma-induced surface PEGDA for effective separation of oil-in-water emulsions. *Colloids Surf. Physicochem. Eng. Asp.* **481,** 151–157 (2015).

10. Ejaz Ahmed, F., Lalia, B. S., Hilal, N. & Hashaikeh, R. Underwater superoleophobic cellulose/electrospun PVDF–HFP membranes for efficient oil/water separation. *Desalination* **344,** 48–54 (2014).

11. Zhang, L., Zhong, Y., Cha, D. & Wang, P. A self-cleaning underwater superoleophobic mesh for oil-water separation. *Sci. Rep.* **3,** (2013).

12. Xue, Z. *et al.* A Novel Superhydrophilic and Underwater Superoleophobic Hydrogel-Coated Mesh for Oil/Water Separation. *Adv. Mater.* **23,** 4270–4273 (2011).

13. Liu, N. *et al.* Straightforward Oxidation of a Copper Substrate Produces an Underwater Superoleophobic Mesh for Oil/Water Separation. *ChemPhysChem* **14,** 3489–3494 (2013).

14. Dong, X. *et al.* Superhydrophobic and superoleophilic hybrid foam of graphene and carbon nanotube for selective removal of oils or organic solvents from the surface of water. *Chem. Commun.* **48,** 10660 (2012).

15. Gui, X. *et al.* Carbon Nanotube Sponges. *Adv. Mater.* **22,** 617–621 (2010).

16. Zou, J. *et al.* Ultralight Multiwalled Carbon Nanotube Aerogel. *ACS Nano* **4,** 7293–7302 (2010).

17. Livraghi, S. *et al.* Nitrogen-Doped Titanium Dioxide Active in Photocatalytic Reactions with Visible Light: A Multi-Technique Characterization of Differently Prepared Materials. *J. Phys. Chem. C* **112,** 17244–17252 (2008).

18. Sun, H., Xu, Z. & Gao, C. Multifunctional, Ultra-Flyweight, Synergistically Assembled Carbon Aerogels. *Adv. Mater.* **25,** 2554–2560 (2013).

19. Mecklenburg, M. *et al.* Aerographite: Ultra Lightweight, Flexible Nanowall, Carbon Microtube Material with Outstanding Mechanical Performance. *Adv. Mater.* **24,** 3486–3490 (2012).

20. Chakrabarty, B., Ghoshal, A. K. & Purkait, M. K. Ultrafiltration of stable oil-in-water emulsion by polysulfone membrane. *J. Membr. Sci.* **325,** 427–437 (2008).

21. Benito, J. M., Ebel, S., Gutierrez, B., Pazos, C. & Coca, J. Ultrafiltration of a waste emulsified cutting oil using organic membranes. *Water. Air. Soil Pollut.* **128,** 181–195 (2001).

22. Melle, S., Lask, M. & Fuller, G. G. Pickering Emulsions with Controllable Stability. *Langmuir* **21,** 2158–2162 (2005).

23. Kaiser, A., Liu, T., Richtering, W. & Schmidt, A. M. Magnetic Capsules and Pickering Emulsions Stabilized by Core−Shell Particles. *Langmuir* **25,** 7335–7341 (2009).

24. Sacanna, S., Kegel, W. K. & Philipse, A. P. Thermodynamically Stable Pickering Emulsions. *Phys. Rev. Lett.* **98,** (2007).

25. Wang, H. *et al.* Removal of oil droplets from contaminated water using magnetic carbon nanotubes. *Water Res.* **47,** 4198–4205 (2013).

26. Srijaroonrat, P., Julien, E. & Aurelle, Y. Unstable secondary oil/water emulsion treatment using ultrafiltration: fouling control by backflushing. *J. Membr. Sci.* **159,** 11–20 (1999).

27. Nabi, N., Aimar, P. & Meireles, M. Ultrafiltration of an olive oil emulsion stabilized by an anionic surfactant. *J. Membr. Sci.* **166,** 177–188 (2000).

28. Zhou, J. *et al.* Magnetic Pickering Emulsions Stabilized by Fe $_3$ O $_4$ Nanoparticles. *Langmuir* **27,** 3308–3316 (2011).

29. He, Y. *et al.* Factors that Affect Pickering Emulsions Stabilized by Graphene Oxide. *ACS Appl. Mater. Interfaces* **5,** 4843–4855 (2013).

30. Ramsden, W. Separation of Solids in the Surface-Layers of Solutions and 'Suspensions' (Observations on Surface-Membranes, Bubbles, Emulsions, and Mechanical Coagulation). -- Preliminary Account. *Proc. R. Soc. London* **72,** 156–164 (1903).

31. Pickering, S. U. Cxcvi.—emulsions. *J. Chem. Soc. Trans.* **91,** 2001–2021 (1907).

32. Vignati, E., Piazza, R. & Lockhart, T. P. Pickering Emulsions: Interfacial Tension, Colloidal Layer Morphology, and Trapped-Particle Motion. *Langmuir* **19,** 6650–6656 (2003).

33. Demond, A. H. & Lindner, A. S. Estimation of interfacial tension between organic liquids and water. *Environ. Sci. Technol.* **27,** 2318–2331 (1993).

34. Dudchenko, A. V., Rolf, J., Russell, K., Duan, W. & Jassby, D. Organic fouling inhibition on electrically conducting carbon nanotube–polyvinyl alcohol composite ultrafiltration membranes. *J. Membr. Sci.* **468,** 1–10 (2014).

35. van den Brink, P., Zwijnenburg, A., Smith, G., Temmink, H. & van Loosdrecht, M. Effect of free calcium concentration and ionic strength on alginate fouling in cross-flow membrane filtration. *J. Membr. Sci.* **345,** 207–216 (2009).

36. Ye, Y., Clech, P. L., Chen, V. & Fane, A. G. Evolution of fouling during crossflow filtration of model EPS solutions. *J. Membr. Sci.* **264,** 190–199 (2005).

37. Defrance, L. & Jaffrin, M. Y. Comparison between filtrations at fixed transmembrane pressure and fixed permeate flux: application to a membrane bioreactor used for wastewater treatment. *J. Membr. Sci.* **152,** 203–210 (1999).

38. Munz, M. & Mills, T. Size Dependence of Shape and Stiffness of Single Sessile Oil Nanodroplets As Measured by Atomic Force Microscopy. *Langmuir* **30,** 4243–4252 (2014).

39. Singh, G. & Song, L. Experimental correlations of pH and ionic strength effects on the colloidal fouling potential of silica nanoparticles in crossflow ultrafiltration. *J. Membr. Sci.* **303,** 112–118 (2007).

40. Lohwacharin, J. & Takizawa, S. Effects of nanoparticles on the ultrafiltration of surface water. *J. Membr. Sci.* **326,** 354–362 (2009).

41. Springer, F., Laborie, S. & Guigui, C. Removal of SiO2 nanoparticles from industry wastewaters and subsurface waters by ultrafiltration: Investigation of process efficiency, deposit properties and fouling mechanism. *Sep. Purif. Technol.* **108,** 6–14 (2013).

42. Lin, S., Cheng, Y., Liu, J. & Wiesner, M. R. Polymeric Coatings on Silver Nanoparticles Hinder Autoaggregation but Enhance Attachment to Uncoated Surfaces. *Langmuir* **28,** 4178–4186 (2012).

43. Wan, L.-S., Xu, Z.-K. & Wang, Z.-G. Leaching of PVP from polyacrylonitrile/PVP blending membranes: A comparative study of asymmetric and dense membranes. *J. Polym. Sci. Part B Polym. Phys.* **44,** 1490–1498 (2006).

44. Jung, B., Yoon, J. K., Kim, B. & Rhee, H.-W. Effect of molecular weight of polymeric additives on formation, permeation properties and hypochlorite treatment of asymmetric polyacrylonitrile membranes. *J. Membr. Sci.* **243,** 45–57 (2004).

45. Aveyard, R., Binks, B. P. & Clint, J. H. Emulsions stabilised solely by colloidal particles. *Adv. Colloid Interface Sci.* **100,** 503–546 (2003).

46. Aveyard, R., Clint, J. H. & Horozov, T. S. Aspects of the stabilisation of emulsions by solid particles: Effects of line tension and monolayer curvature energy. *Phys. Chem. Chem. Phys.* **5,** 2398 (2003).

47. Torkzaban, S., Bradford, S. A. & Walker, S. L. Resolving the Coupled Effects of Hydrodynamics and DLVO Forces on Colloid Attachment in Porous Media. *Langmuir* **23,** 9652–9660 (2007).

48. Bergendahl, J. & Grasso, D. Prediction of colloid detachment in a model porous media: hydrodynamics. *Chem. Eng. Sci.* **55,** 1523–1532 (2000).

49. Johnson, K., Kendall, K. & Roberts, A. Surface energy and the contact of elestic solids. *Proc. R. Soc. London* **324,** 301–313 (1971).

50. Bai, R. & Tien, C. Particle Detachment in Deep Bed Filtration. *J. Colloid Interface Sci.* **186,** 307–317 (1997).

51. Chan, S. K. & Ng, K. M. Geometrical characteristics of the pore space in a random packing of equal spheres. *Powder Technol.* **54,** 147–155 (1988).

52. Schrader, M. E. Young-dupre revisited. *Langmuir* **11,** 3585–3589 (1995).

53. Office, U. G. P. 33 CFR 155.350-370 - Oily mixture (bilge slops) discharges on oceangoing ships, excluding ships that carry ballast water in their fuel oil tanks. 350–370 (2010).

54. Chew, C. M., Aroua, M. K., Hussain, M. A. & Ismail, W. M. Z. W. Practical performance analysis of an industrial-scale ultrafiltration membrane water treatment plant. *J. Taiwan Inst. Chem. Eng.* **46,** 132–139 (2015).

55. Pearce, G. K. UF/MF pre-treatment to RO in seawater and wastewater reuse applications: a comparison of energy costs. *Desalination* **222,** 66–73 (2008).

56. Potapova, E. *et al.* Interfacial properties of natural magnetite particles compared with their synthetic analogue. *Miner. Eng.* **36–38,** 187–194 (2012).

57. Potapova, E. *et al.* The effect of calcium ions, sodium silicate and surfactant on charge and wettability of magnetite. *Colloids Surf. Physicochem. Eng. Asp.* **386,** 79–86 (2011).

58. Potapova, E., Grahn, M., Holmgren, A. & Hedlund, J. The effect of polymer adsorption on the wetting properties of partially hydrophobized magnetite. *J. Colloid Interface Sci.* **367,** 478–484 (2012).

59. Dudchenko, A. V., Rolf, J., Russell, K., Duan, W. & Jassby, D. Organic fouling inhibition on electrically conducting carbon nanotube–polyvinyl alcohol composite ultrafiltration membranes. *J. Membr. Sci.* **468,** 1–10 (2014).

60. Drelich, J. *et al.* AFM colloidal forces measured between microscopic probes and flat substrates in nanoparticle suspensions. *J. Colloid Interface Sci.* **301,** 511–522 (2006).

61. Jönsson, A.-S. & Trägårdh, G. Fundamental principles of ultrafiltration. *Chem. Eng. Process. Process Intensif.* **27,** 67–81 (1990).

62. Bowen, W. R., Jones, M. G. & Yousef, H. N. Prediction of the rate of crossflow membrane ultrafiltration of colloids: A neural network approach. *Chem. Eng. Sci.* **53,** 3793–3802 (1998).

Chapter 4 Frequency Dependent Stability of CNT Joule Heaters in Ionizable Environments: Implications for Desalination

4.1 Summary

Water shortages and brine waste management are an increasing challenge for coastal and inland regions, with high salinity brines (such as produced water or reverse osmosis waste brines) presenting a particularly challenging problem. These high-salinity waters require the use of thermally driven treatment processes, such as membrane distillation (MD), which suffer from high complexity and cost. Herein, we demonstrate how controlling the frequency of an applied alternating current at high potentials (20 Vpp) to a porous thin-film carbon nanotube (CNT)/polymer composite Joule heating element can prevent CNT degradation in ionizable environments such as high-salinity brines. Using electrical impedance spectroscopy, we show that electrooxidation of CNTs is a strong function of the applied frequency and ion concentrations in the CNT's immediate environment. Application of high frequencies (>100 Hz) results in electrons preferentially charging the electrical double layer (EDL), while at low frequencies electrons in the fully charged EDL can participate in CNT-degrading electrochemical reactions. By operating at sufficiently high frequencies, these porous thin-films can be directly immersed in highly-ionizable environments and used as flow-through heating elements. Finally, we demonstrate that porous CNT/polymer composites can be used as a self-heating membranes for desalination. These self-heating membranes are used to directly heat high salinity brines at the water/vapor interface of the MD element, making it possible to achieve exceptionally high single-pass recoveries that approach 100%, far exceeding the classical MD theoretical limit of 6.5%.

4.2 Introduction

Coastal and inland regions are struggling to address water shortages caused by population growth, urbanization, and climate change. [1] Although reverse osmosis (RO) is the de facto standard technology for desalination, RO is not capable of treating fluids with high osmotic pressures, such as produced water, and RO-generated waste brines. [2,3] Thermal desalination processes, such as membrane distillation (MD), are the treatment method of choice for these brines, due to their relative insensitivity to salinity (Fig. 4.1a). [4] In the MD process, a temperature gradient across a hydrophobic membrane (hot brine and cold distillate) drives the transport of water vapor across the membrane, while liquid water and dissolved salts are prevented from passing through. [5] Unfortunately, these hot, high-salinity brines are highly corrosive, which makes heat management (i.e. heat exchangers) in these systems prohibitively expensive due to the need for corrosion-resistant metals, such as Nickel alloys.[6] Providing the thermal energy needed for water evaporation directly at the membrane/brine interface could significantly reduce the energy intensity and simplify material choice and system design of MD-based desalination processes. A thin, porous and electrically conducting carbon nanotube (CNT) film deposited on the membrane surface, in direct contact with the brine, could be used as a Joule heater to drive the MD desalination process (Fig. 4.1b, c). While CNT-based Joule heaters have been previously demonstrated, they were always used in non-ionizable environments, e.g. embedded in a shielding medium (polymer or glass) or used in air.[7–12] In these past demonstrations, direct current (DC) was used to provide the energy to the CNT surface. However, the large electrical potentials needed to generate the power necessary for heating

can lead to the rapid electrochemical degradation of CNT films in an ionizable medium, which has limited their use. Thus, a porous thin-film Joule heating element able to function in a highly corrosive and ionizable environment without impeding the performance of the membrane material itself could transform thermally-driven separation and catalytic processes such as MD-based desalination, pervaporation, and hydrocarbon hydrogenation.[13–18]

The Joule heating effect occurs when the resistance of a conductor to electron flow leads to the conversion of the electron's kinetic energy to thermal energy. Previously reported thin-film Joule heaters used materials such as indium tin oxide, CNTs, and metal nanowires.[11] These films were demonstrated in various applications, such as window defrosting and thermochromic displays.[7,19] The relative low cost and the ability to form conductive and porous films makes CNTs an ideal material for use as a Joule heating element in thermally driven separation processes.[20–22] However, to the best of our knowledge, all reported CNT Joule heaters have been demonstrated in low-ionizable conditions, where the application of the high voltages (10 – 20 Vpp) required to power the element did not ionize the surrounding media, which ensured the CNTs maintained their stability and heat-transfer properties.[7,8,12] However, in ionizable mediums, such as high salinity brines, the application of even low anodic potentials (<2 VDC) to the CNT film can lead to surface charging, water splitting, and rapid degradation.[23–25] Although polymer coatings could be used to shield the CNTs from the environment, these coatings block the porous structure of the film and form an additional thermal barrier between the heated CNT network and the fluid. Thus, a method that prevents CNT degradation while maintaining

the CNT porous structure and maximizing thermal transport between the heating element and the fluid would be highly desirable.

In this study, we report on the fabrication of porous thin-film CNT Joule heaters, and their stable operation in highly ionizable environments. By using alternating currents (AC), where the polarity of the applied potential is rapidly switched, we provide power to the porous CNT film and demonstrate that CNT joule heaters can operate for extended periods of time in high salinity environments with no degradation. Utilizing electrical impedance spectroscopy (EIS) we study the stability of the CNT structure under the application of AC potentials at different frequencies and use this data to develop an equivalent circuit that captures the electron pathways through the CNT structure and surrounding saline water as a function of the applied frequency. Finally, we demonstrate that high frequency AC can be used to heat the CNT films, generating the needed thermal driving force at the water/vapor interface in an MD process for desalinating high salinity brines.

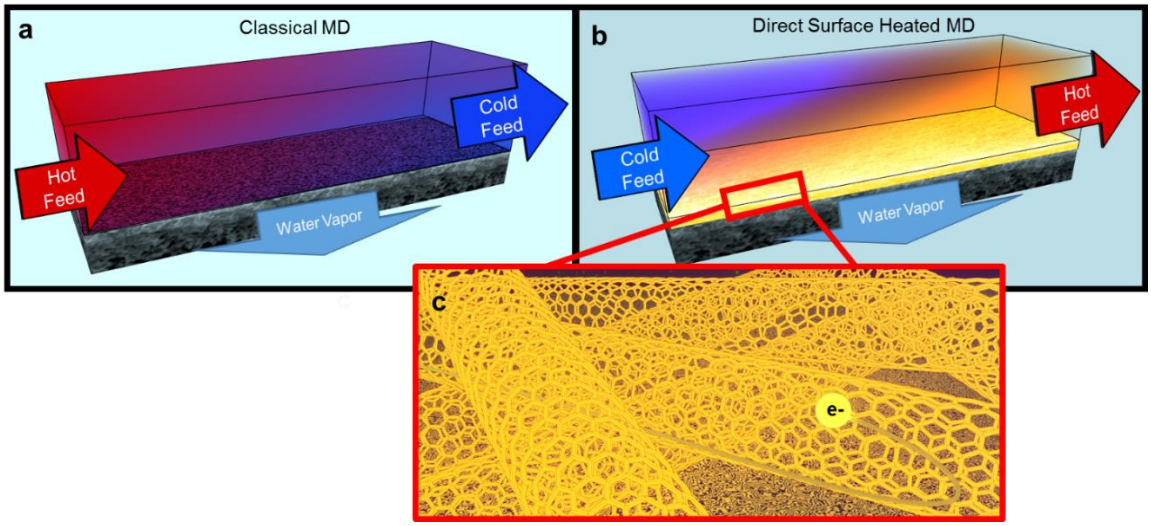

Figure 4.1 | Comparison of classical and directly heated membrane distillation. a, Diagram of a classical MD process where a hot feed (brine) flows over one side of a hydrophobic membrane and a cold distillate stream flows over the other side, leading to a vapor pressure gradient across the membrane that drives water vapor from the hot, salty feed to the cold distillate. b, Direct surface heating of a composite MD membrane composed of a porous CNT-based Joule heater and a hydrophobic porous support. The cold feed (brine) is heated on the membrane surface, which drives water vapor transport across the hydrophobic support into the distillate stream, leaving dissolved ions behind. c, Zoomed-in rendition of the thin-film CNT joule heater structure on an MD membrane surface showing electron flow and heating.

4.3 Results and Discussion

4.3.1 Self-heating and stable CNT/polymer composite MD membranes

We developed a method that uses layer-by-layer spray coating of carboxylated CNTs and polyvinyl alcohol (PVA) to construct a highly conductive, hydrophilic, and porous thin film deposited on a hydrophobic porous membrane support (Fig. 4.2a-d). The spray coating process aerosolizes a CNT suspension and prevents the CNTs from entering the support membrane's pore structure during deposition; this preserves the support membrane's separation properties (porosity, hydrophobicity, pore size). The CNT layer is immobilized by cross-linking the CNT's carboxyl and hydroxyl surface groups with PVA, forming a hydrophilic and robust conductive thin film.[21] Using this approach, we deposit

CNT-PVA films onto large (450 cm^2) hydrophobic 0.2 μm polytetrafluoroethylene (PTFE) membranes, with a CNT film thickness of 15±2 μm, electrical conductivity (in water) of 1700±200 S/m, and a highly hydrophilic surface (air contact angle of 160±4°) (Fig. 4.2b-f). While MD processes require a hydrophobic membrane that prevents liquid water (and dissolved ions) from passing through, the distinct dual-layer structure of these composite hydrophilic/hydrophobic membranes allows them to function as standard MD membranes, where the vapor formation occurs at PTFE/CNT interface, achieving salt rejection in excess of 99%.

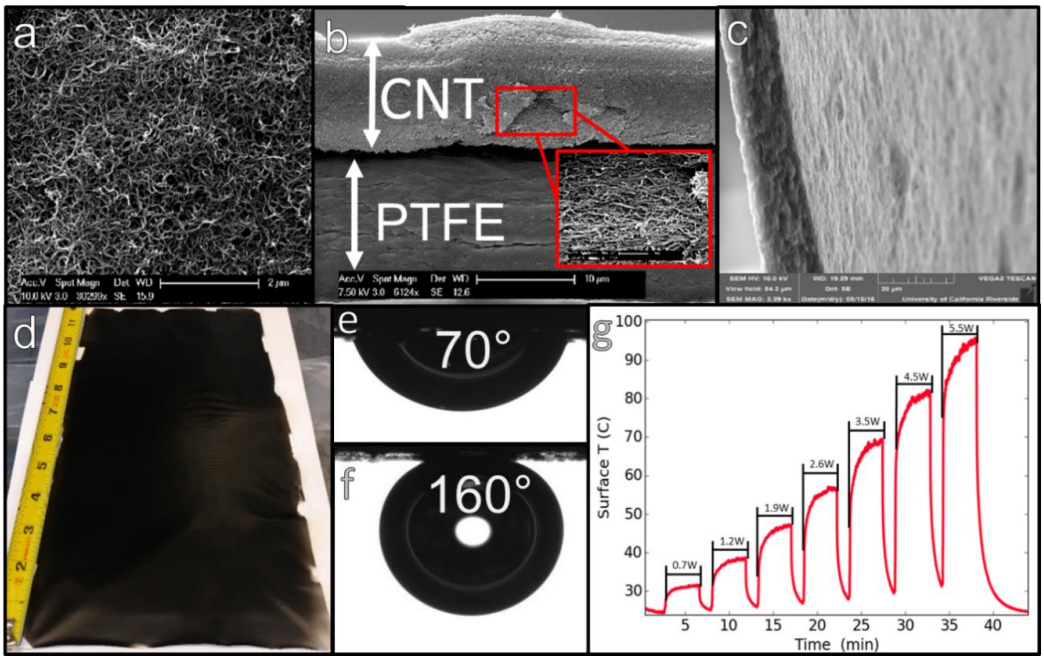

Figure 4.2 | Spray coated CNT/PVA porous self-heating films on PTFE supports. a, Scanning electron microscope (SEM) image of CNT/PVA film surface. b, SEM image of CNT/PVA cross section on PTFE support, with inset showing zoomed-in structure of CNT cross section (scale bar 2 μm). c, SEM image of free standing CNT/PVA film cross-section. d, Image of a large spray coated membrane (size 30 by 15 cm, scale is in inches) e, contact angle of air with PTFE surface (angle of 70°). f, Contact angle of air with CNT/PVA coated PTFE membrane (angle of 160°) g, Direct heating of the CNT structure under convective air flow with the application of electrical power.

The application of a DC potential across a membrane coupon (4 cm^2) under convective air cooling resulted in immediate surface heating, with an increase in applied power leading to higher surface temperatures (Fig. 4.2g). In air, the surface temperature reached 95°C when 5.5 W were applied to the membrane surface (1.375 W/cm^2). However, the application of a DC potential also leads to the formation of a potential gradient across the membrane with anodic and cathodic regions (Fig. 4.3a).[26] When the CNT film is immersed in a difficult-to-ionize medium (e.g. air), the electrons will only flow through the CNT film, leading to heating. However, if the CNT film is immersed in an ionizable solution (e.g. salt water) the electrons can flow through two pathways - through the CNT structure, where the majority of the energy is dissipated as heat, or through the ionized solution, leading to surface charging and electrochemical reactions commonly observed in electrochemical cells (Fig. 4.3b). In CNT-based anodes, it has been observed that the application of anodic potentials (>1.2 V) in ionizable solutions leads to rapid electrooxidation of the CNT network.[23,24] However, to achieve high surface temperatures, high electrical potentials (>10 V) must be applied across the CNT network, making DC potentials not appropriate for operation in ionizable environments.

In a typical electrochemical cell, the application of an electrical potential forces electrons to flow from the cathode to the anode, with the electrons flowing through the path of least resistance.[27] This is a multi-step process, where first the electrons form an electrical double layer (EDL) (surface charging), followed by electrons participating in electrochemical reactions. For EDL formation, the electrons only have to overcome the resistance of the electrode material, which is typically orders-of-magnitude lower than that

of the media, leading to charge accumulation on the electrode surface (negative on cathode and positive on anode).[28] Once the EDL is fully formed (i.e. the charge is balanced by counter ions in the solution), and if sufficient potential is applied, electrons/holes can participate in electrochemical reactions, including electrooxidation of the CNT network on the anodic side of the cell.[23,24] Thus, if the EDL layer can be prevented from fully forming, it would be possible to prevent electrooxidaiton of CNTs.

EDL formation can be controlled through rapid switching of the applied polarity (i.e. AC potential) that leads to swift charging and discharging of the EDL layer. [29] The overall charge of the EDL decreases with increasing frequency, which potentially prevents electrochemical reactions. Measuring the phase shift between the applied potential and the current (using EIS), allows for the determination of the real and imaginary impedance of the system.[30] The real impedance describes the resistance of the system to electron flow (i.e. resistive behavior), while the imaginary part describes the resistance to change in electron flow (i.e. inductive or capacitive behavior). Spray-coated CNT/PVA films were immersed into NaCl solutions (10 – 100 g/l), and an AC potential (20 Vpp) was applied at different frequencies (0.3 – 10,000 Hz). The Nyquist plot generated under different solution concentrations revealed a classic semi-circle shape with negative imaginary impedances attributed to capacitive charging. (Fig. 4.3c) The increase in the size of the semi-circle and the negative imaginary impedance with salt concentration is indicative of increasing capacitance. (Fig. 4.3c) These results are in line with standard EDL formation theory that predicts increasing capacitance in the presence of increasing electrolyte concentrations.[31] A bode plot of EIS data demonstrates that decreasing operating frequencies led to an

increase in the absolute impedance of the system (|Z|), indicating that electrons have to flow through a path of higher resistance as the frequency decreases (Fig. 4.3d). This increase in absolute impedance is the result of the EDL formation at low frequencies (indicated by increasing phase shift, i.e. capacitive charging), which forces electrons to participate in redox reactions. (Fig. 4.3d) Thus, the formation of the fully charged EDL can be prevented through the application of sufficiently high AC frequencies, with the onset of EDL formation being dependent on the solution ionic strength (higher salt concentrations leads to onset at higher frequencies). By eliminating the formation of the EDL, CNT-degrading electrochemical reactions can be prevented, which is reflected by the minimized |Z| values at sufficiently high frequencies (Fig. 4.3d).

The oxidation of the CNTs can be understood by following the electron pathway through the CNT network immersed in a saline solution, which we described using an equivalent circuit (Fig. 4.3e). The circuit is composed of two parallel sub-circuits in series with a dry CNT contact resistance RCT (resistor). The first sub-circuit describes the electron pathway through the immersed CNT network, where RM (resistor) describes the dry CNT resistance in series with a constant phase element (CPE-Q_m, non-ideal capacitor) that describes pseudo capacitance of the CNT network, in parallel with the wet CNT resistance (RMS, resistor), which is the result of CNT hydration and disruption of the percolating network. The second sub-circuit (Fig. 4.3e, surrounded by dashed red line) describes the electron pathway through the solution, where RS (a resistor) describes the solution resistance, which is in series with a constant phase element (CPE-EDL, non-ideal capacitor) describing EDL formation in parallel with a polarization element (RP, a resistor)

that describes the resistance to charge transfer (i.e. electrochemical reactions) (Fig. 4.3e). The developed circuit was fitted to the acquired EIS data and the fits are presented with solid lines on the Nyquist and Bode plots, where the goodness of the fit was judged by the R^2 value acquired from fitting of real and imaginary impedance data, with $R^2 > 0.92$ for all fits. (Appendix Section 4.5.1)

In the proposed circuit, electrons can charge the surface (i.e. lead to EDL formation (CPE-EDL)) or transfer from the CNT network to the solution and participate in oxidation/reduction reactions (i.e. pass through the RP circuit element), similar to a Randle's circuit (Fig. 4.3e). [32] Thus, for each frequency tested, the ratio between the current flowing to the polarization element and the current flowing to the EDL can be used to gauge the CNT degradation rate, with higher ratios (i.e. more electrons participating in redox reactions) corresponding to increased CNT degradation rates and lower ratios corresponding to more effective surface heating. Using the values acquired from the equivalent circuit, we calculated the current transfer ratio between the RP element and EDL element. (Appendix Sec. 4.5.2) The current transfer ratio is a strong function of operating frequencies and a moderate function of salt content, where an increase in frequency leads to a rapid reduction in the current ratio, while increase in salt content raises the ratio (Fig. 3f). For example, the ratio at the low frequency of 0.1 Hz (10 g/l) is 4/1 implying that for every electron used to charge the EDL layer, four electrons passed through the polarization element, potentially participating in an electrochemical reaction. In contrast, at 1 kHz, the ratio reduces to 1/10,000 (Fig. 4.3f). Thus, through use of AC potentials with moderate

frequencies to power the CNT joule heating elements it is possible to significantly reduce, or even prevent the degradation of the CNT network.

Time studies were performed to confirm the results of the EIS analysis, where an increase in real impedance over time was used as an indicator of CNT degradation. The application of an AC potential with a frequency of 10 kHz and 20 Vpp to a CNT network immersed in 100 g/l of NaCl showed no degradation after 125 hours of continuous operation (Fig. 4.3g). At 1 kHz and 100 Hz no increase in real impedance was observed, although a phase shift of -0.7° and -4.4° was measured, respectively. At these frequencies, partial surface charging resulted in current transfer rations of 3/200 and 3/2000, respectively (Fig. 4.3f). Importantly, these long-term studies demonstrated that at these current ratios, redox reactions are either insignificant or reversible due to the constantly switching polarity (oxidation $\leftrightarrow$ reduction). When the frequency was further reduced to 10 Hz the phase shift increased to -11°, indicating large EDL formation and the charge transfer ratio increased beyond 1/10 (Fig. 4.3g). Under these conditions the real impedance (i.e. the electrical resistance of the CNT network) increased by 50% after 24 hours due to severe CNT network degradation. Operating at 1 Hz lead to nearly complete CNT network failure in less than an hour (Fig. 4.3g). These results are in agreement with EIS measurements which predicted large EDL formation and high current transfer ratios at low operating frequencies (<10 Hz) leading to rapid CNT degradation. Furthermore, the EIS measurements showed that EDL formation and current transfer ratios can be significantly reduced when operating above 100 Hz where no CNT degradation was observed during the time studies. These results demonstrate that CNT films can be directly heated in highly

ionizable environments using moderate frequency AC and remain stable for long periods of time.

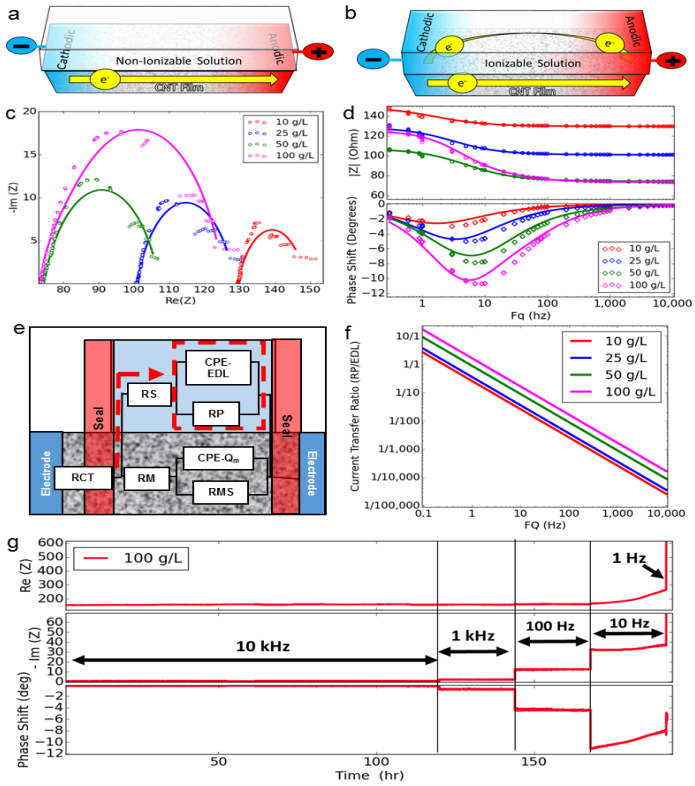

Figure 4.3 | Stability of CNT films under different electrical conditions. a, Electron flow through a CNT network under DC conditions in a non-ionizable environment. b, Electron flow through a CNT network under DC conditions in an ionizable environment. c, Nyquist plot of real and imaginary impedance showing an increase in capacitive charging with increased salt content (markers are measured values, solid lines show the fitted equivalent circuit); the applied frequency increased from right (0.3 Hz) to left (10 kHz). d, Bode plot of absolute impedance (|Z|) and phase shift vs. the applied frequency for immersed CNT networks in different salt solutions (markers are measured values, while solid lines show the fitted equivalent circuit). e, Equivalent circuit describing electron flow through CNT films and surrounding ionizable media during the application of AC current. The red dashed lines designate the electron path describing the degradation pathway of the CNT structure, with the red dashed box showing the circuit that was used to calculate the current transfer ratio between RP and EDL. f, Charge transfer ratios between polarization resistance and EDL calculated from fitted values at different salt concentrations. g, Time dependent degradation of CNT/PVA films under different applied frequencies at 100 g/l of NaCl; an increase in real and imaginary impedance (the units for both are ohms) indicates degradation, while phase shift indicates surface charging.

4.3.2 Porous CNT Joule Heating in Membrane Distillation

Direct heating of the feed stream in MD systems can be accomplished through the application of an electrical potential across the feed channel, where the conductive saline solution *or* the CNT network can be used as the Joule heating element (Fig. 4.4a,b). Although saline water could be used as the heating element for direct feed heating, the application of a potential to the electrodes lead to their rapid corrosion, making this method unsuitable for long-term operations (Appendix Sec. 4.5.3). Furthermore, using saline water as a heating element does not allow for the direct delivery of thermal energy to the water/membrane interface, resulting in energy losses to the bulk feed. [33,34] Using a custom-built MD cell, we directly heated the feed stream inside the module using either titanium electrodes, or CNT/PVA membranes. The application of electrical power (50 W) to the cell resulted in a rapid increase in permeate flux and an increase in feed outflow temperatures when treating a high concentration brine (100 g/l) (Fig. 4.4c,d, Appendix Sec. 4.5.4); salt rejection in these experiment exceeded 99%. Cross-flow velocity had a strong impact on single pass recovery rates, with the system achieving a recovery rate of 14%, 4.8%, and 1.6% at 1.5 mm/s, 3.3 mm/s and 6.6 mm/s, respectively (Fig. 4.4c). Importantly, these recoveries were achieved over a path-length of 10 cm. Thus, in longer path-lengths typically used in real-world applications (1 m), extremely high single–pass recoveries could be achieved. When the velocity was set to zero, 100% theoretical recovery could be achieved. By decoupling heat delivery from the flow rates, single pass recoveries using self-heating membranes far exceed the theoretical maximum single-pass recovery (6.5%)

in classic MD systems. [33,3433] Direct heating with the CNT structure resulted in higher permeate fluxes at moderate cross flow velocities of 3.3 and 6.6 mm/s demonstrating 20±5% and 35±5% improvement over the bulk feed heating using Ti plates alone (Fig. 4.4c). The higher permeate flux achieved with the CNT/PVA structure is the result of direct surface heating, which reduced the thermal losses to the bulk feed and maintained a higher quanta of thermal energy for vapor formation resulting in lower feed out-flow temperatures (Fig. 4.4c,d). Simulations of the heat generation and transfer process within the MD cell, done using a finite element method (FEM), agreed with experimental results, demonstrating that direct surface heating using the porous CNT/PVA structure resulted in higher permeate fluxes, membrane surface temperatures, and lower out-flow temperatures (Fig 4.4e,f). The results from MD experiments and FEM simulations demonstrate that a CNT/PVA joule heating element coupled to a hydrophobic MD membrane allows for direct heating of water at the membrane surface even in highly saline solutions, achieving high single pass recoveries, and maintaining thermal energy at the vapor forming interface.

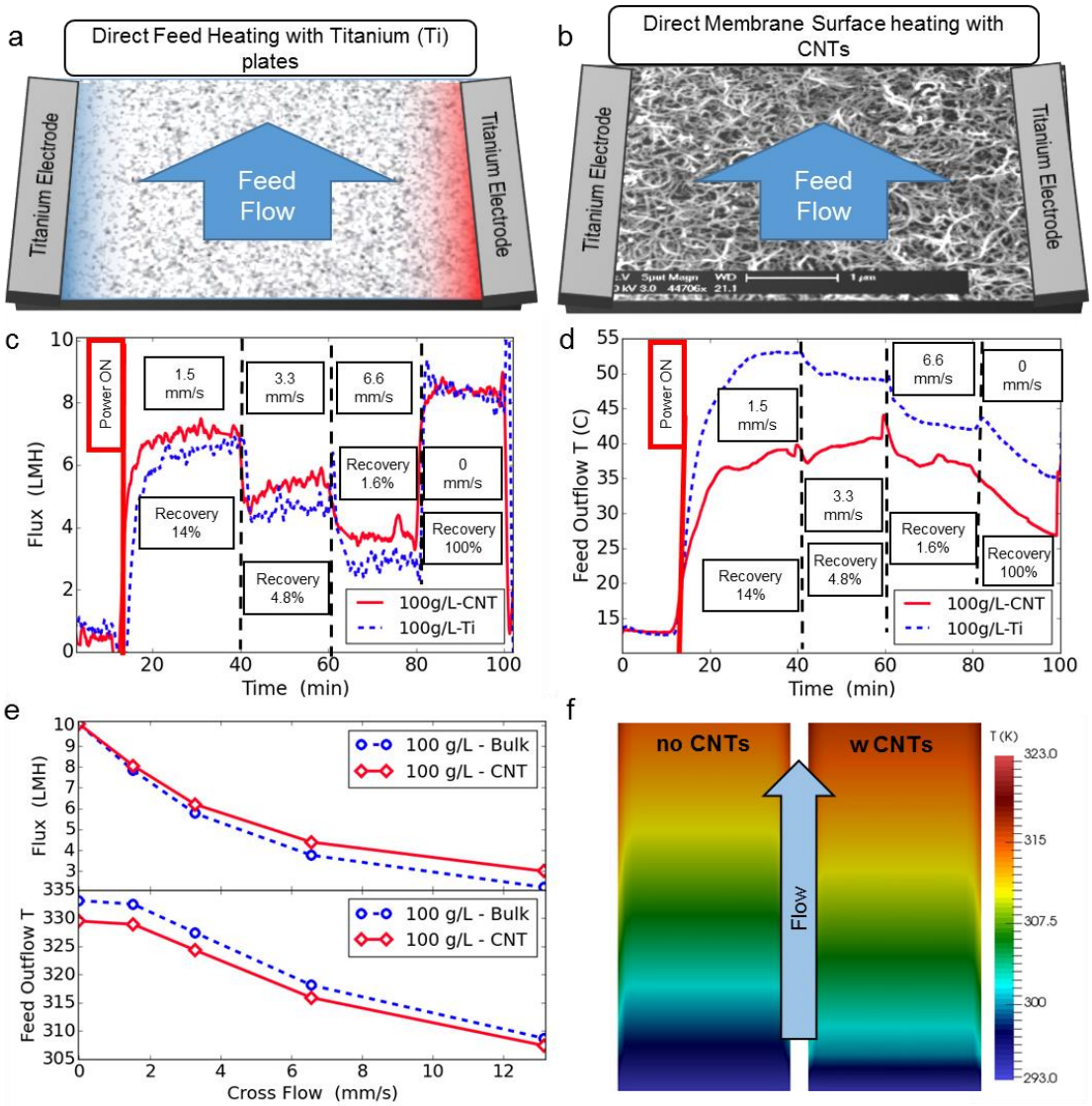

Figure 4.4 | Demonstration of direct surface heating for brine desalination using MD. a, Direct heating of feed solution using titanium electrodes, with the brine acting as a heating element. b, Heating of CNT/PVA porous network deposited on hydrophobic MD membrane using AC power (here both CNT and Ti plates are immersed in brine). c-d, Permeate flux and feed outflow temperature data for different cross flow velocities with brine concentration of 100 g/l NaCl. e, FEM simulation results showing the difference in permeate flux and outflow temperatures (units in K) vs. increasing cross-flow velocity of direct (CNT/PVA) heating (red line) and solution heating (blue line). f, FEM simulation showing the difference between membrane surface temperatures for a direct solution heated system (left) and a system heated using the CNT/PVA porous network (right) at a cross flow velocity of 6.6 mm/s and 100 g/L of NaCl

4.3.3 Conclusions

We have fabricated porous CNT/PVA Joule heaters and demonstrated that they can be directly heated in highly corrosive and ionizable environments, while showing no degradation in performance even when exposed to very high potentials (20 Vpp). The CNT/PVA Joule heater was then used to desalinate high-salinity brines using an MD process. The stability of the CNT/PVA network was studied using EIS, which revealed that the formation of a fully-charged EDL can lead to electrochemical reactions and CNT degradation. The EIS results demonstrated that EDL formation and overall system impedance is a strong function of the AC frequency, where operation at frequencies >100 Hz (at NaCl concentrations of 100 g/l) will limit the charging of the EDL and mitigate CNT electrooxidation. EIS data was used to develop an equivalent circuit for current flow through a CNT network immersed in a saline solution, from which the current transfer ratio between electrochemical reactions and EDL charging was determined. The ratios were predicted to be greater than 1/10 at frequencies below 10 Hz, and rapidly decreased below 1/100 when frequencies exceeded 100 Hz, indicating that an insignificant number of electrons were utilized for electrochemical reactions at elevated operating frequencies. Extended time studies agreed with the EIS measurements and the predicted current transfer ratios, demonstrating that no CNT degradation occurred after 125 hours of continuous operation at 10 kHz and 24 hours at 100 Hz. However, rapid CNT degradation was observed when frequencies dropped below 10 Hz, when current transfer ratios approached unity. Finally, the developed CNT/PVA joule heaters were used in an MD-based desalination process, demonstrating direct feed heating at the membrane surface and

achieving exceptionally high single-pass recovery of up-to 100%, which exceeds the 6.5% theoretical maximum predicted for standard MD processes. The developed porous CNT/PVA joule heaters have demonstrated great potential for the treatment of highly saline brines, potentially leading to simpler MD system designs, and allowing for significant improvement of most thermally driven processes in reactive, ionizable environments by eliminating the need for bulk feed heating.

4.4 Methods

CNT films were prepared via sequential spray deposition of CNT and PVA solutions onto a porous polymeric membrane surface. The CNT suspension was prepared by suspending 1 g/L of multi-wall CNTs functionalized with carboxylic groups (Cheaptubes Inc., Brattleboro, VT) and 10 g/L of Dodecylbenzenesulfonic acid (DDBS) (Fisher Sci, Hampton, NH) in deionized (DI) water. The suspension was sonicated with a horn sonicator (Branson; Danbury, CT) for 30 minutes in an ice bath and then centrifuged at 11,000 RCF for 10 minutes, after which the supernatant was collected and used as is. The PVA solution was prepared by first dissolving 1 wt% PVA (Fisher Sci, Hampton, NH) in DI water at 95 C˚, followed by dilution to 0.1 wt% with DI water before spray deposition.

Spray coating was accomplished using an in-house built spray coater with two axis of movement: a roll stage that moved the substrate (a 0.2 μm PTFE microfiltration membrane (Sterlitech, Kent, WA)) at a rate of ~1 mm/s, and a spray-head stage equipped with two spray nozzles that moved across the membrane at rate of 400 mm/s, and was elevated 10 cm above the membrane surface. The spray nozzles (Harbor Freight,

Calabasas, CA) were air driven using house air at 20 PSI. The injection of CNT or PVA solution into the air stream was controlled with an injection needle. The CNT and PVA solution were delivered to the nozzles from graduated cylinders using centrifugal pumps, allowing for precise monitoring of the volume utilized during the spray coating. The substrate surface was heated to 60 C˚ using an air heater to facilitate solvent (water) evaporation. The 0.2 μm PTFE membrane substrate were sprayed with 2.9 ml/cm^2 and 0.015 ml/cm^2 of CNT and PVA solution, respectively. The membrane was then rinsed with DI water for an hour removing excess DDBS. The CNT-PVA network was crosslinked in 0.5 vol% glutaraldehyde (Fisher Sci.) and 1 vol% of hydrochloric acid (Fisher Sci.) solution, and heated to 70 C˚ for 1 hour. Finally, the membrane was dried at 90 C˚ for 15 minutes and used as is.

The membrane surface was imaged using an SEM (Tescan USA, Inc., Warrendale, PA and (FEI, Hillsboro,OR), and air bubble contact angles were measured using a goniometer with an inverse cell (Ramé-hart Instrument Co., Succasunna, NJ). Wet membrane conductivity was measured by first soaking the membrane in DI water and then measuring conductivity with a four-point conductivity probe (Veeco; Plainview, NY). The EIS experiments were performed by placing the membranes into an in-house built electrochemical cell. Titanium electrodes were placed at the ends of a 2 X 1 cm membrane coupon, and were sealed with vacuum grease and plastic covers. The resulting cell had an active area of 100 mm^2 and was immersed into the salt solution. The power to the cell was supplied using a Rigol DG1022 waveform generator, while the voltage and current were measured using Rigol DS1054z oscilloscope (RIGOL Technologies Inc. Beaverton, OR).

The waveform generator as well as the oscilloscope were controlled using custom software that could perform standard EIS measurements, acquiring waveforms with 300k data points during EIS measurements and 30k data points during time studies. In all experiments, 10 oscillation periods were recorded and a 20 Vpp AC sine wave was used. The fitting of the developed circuit was accomplished using non-linear least square regression (Details in Appendix Section. 4.5.1)

The MD experiments were performed using a fully instrumented and automated system operating in vacuum-assisted air-gap mode. A modified MD cell with a classical layout for feed (10 cm L, 4.5 cm W, 1.0 mm H) and distillate channels (10 cm L, 4.5 cm W, 4 mm H) were used. Feed was pumped through the system using a peristatic pump (Greylor Company, Cape Coral, FL), while the air (on the distillate side) was pumped at a rate of 30 L/min with applying a vacuum pressure of less than 0.5 inHg using a vacuum pump (Cole-Parmer, Vernon Hills, IL). Salt rejection was measured using a conductivity meter (Thermo Fisher Scientific Inc, Chino, CA). Power to the feed channel was delivered through two titanium shim electrodes (0.005-inch-thick) placed in parallel with the fluid flow, and were sealed with a gasket protruding 0.1 mm into the feed. The power to the electrodes was delivered using an in-house built power source that used a digital DC power supply (Shenzhen Korad Technology Co, Shenzhen, China), an in-house built H-Bridge, and a DG1022 waveform generator. The H-Bridge was built with IRF640 and IRF9630 MOSFETs, and was switched using DG1022 waveform generator with a square wave at 10 kHz. The power delivery to the cell was controlled through custom-written software that monitored voltage and current delivery to the cell using the DS1054z oscilloscope.

The software adjusted the voltage supplied by the DC power supply to the H-bridge, maintaining constant power delivery regardless of operating conditions. The surface temperature of a CNT coated membrane was measured with an IR thermometer (Testo Inc, Sparta, NJ), the membrane was placed 10 cm away from a fan flowing air at 125 cubic feet per minute (Thermo Cool Corp, San Jose, CA) with power being supplied by same set up as discussed above

FEM simulations were carried out using the FENICS project software package. [35] The calculations simulated conditions inside the feed channel with dimensions identical to the experimental flow cell. The mesh used for calculations was made up of 24,453 vertices and 121,860 cells. The simulation was split into three calculation steps: 1) A solution for electrical potential distribution in the cell using Eq. 4.1, where V is the voltage and σ is the electrical conductivity of the media.[36] 2) Following the solution to the potential distribution, the classical incompressible Navier-Stokes equation (Eq. 4.2) was solved, where ρ is density of the fluid, u is velocity of the fluid, μ is fluid viscosity and p is the pressure.[37] 3) Once the potential distribution and velocity profiles were known, a conductive and convective heat transfer equation (Eq.4.3) with a Joule heating source was solved.[36] Here, the k is the conductive heat transfer coefficient, T is the surface temperature, C_p is the heat capacity of fluid, and $\sigma^*|\nabla V^2|$ is the Joule heating term.

$$\nabla(\sigma * \nabla V) = 0 \; Eq.4.1$$

$$\rho * u\nabla u \; - \mu\Delta u + \nabla p = 0 \;\; Eq.4.2$$

$$k\nabla^2 T + C_p * \rho * u * \nabla T = \sigma * |\nabla V^2| \; Eq.4.3$$

The simulations assumed that the CNT film was a solid structure, which had the same thermal properties as water and uniform electrical conductivity of 1700 S/m^2. This assumption is valid since a large fraction of the volume of the CNT/PVA structure is occupied by water.[23] The Navier-Stokes calculations assumed that the distillate flux would have negligible impact on the velocity profile and thus, no slip conditions were used on all channel walls, except at the inflow and outflow. The heat transfer calculations assumed that the thermal conductivity of the membrane did not change and had a value of 0.03 W/(m K˚), vapor permeability of 0.3 LMH/ΔC, and thickness of 150 μm. It was further observed during experiments that the distillate channel temperature did not significantly change and thus, a constant temperature of 293 K˚ was used. The thermal conductivity, heat capacity, and enthalpy of vaporization correlations were acquired from Sharqawy et. al (2010), and accounted for impact of salinity and temperature. [38]

4.5 Appendix

4.5.1 Fitting of Values to EIS Data calculation:

EIS data was fitted to the proposed equivalent circuit using nonlinear least square regression.[30] The fitting was constrained by measuring RM, RCT and RMS before the EIS measurements and limiting their variation to ±10 % during the fitting process. The RM, RCT and RMS were found by measuring total resistance of the CNT membrane in air, which allowed for the calculation of RCT (resistance under electrode covers) and RM (resistance of membrane in the channel) (i.e. the electrode covered length was typically 10 mm while the length of the channel was 13 mm, thus, if the total dry resistance is 100 ohms,

then $RCT = \frac{10}{10+23} * 100\ ohms = 43\ ohms$, and in the same manner RM would be 57 ohms). The RMS value was found by immersing the cell in deionized water and measuring the new cell resistance, after which it was assumed that any increase in resistance was a result of CNT hydration, which breaks the CNT network percolation resulting in an increased resistance (i.e. increase from 100 ohms in air to 130 ohms in DI water meant that RMS was 30 ohms). The CPE element was solved for by using equation A4.1, where *Q* is the pseudo-capacitance, *j* is an imaginary number, *w* is frequency, and *n* is the correction value (and has a value between 0 and 100); the fitted values are shown in table A4.1. [30,39]

$$Z_{CPE} = \frac{1}{Q * (j * w)^{n/100}}\ eq.A4.1$$

Table A4.1 | Values acquired from the fitting of EIS data to the equivalent circuit

	Membrane Properties					Solution Properties			
Salt (g/L)	RM (Ω)	RCT (Ω)	RMS (Ω)	CPE-Q_m (μF)	n_m	RS (Ω)	RP (Ω)	CPE-EDL (μF)	n_s
10.00	66.00	47.00	39.15	0.02	0.00	381.56	3163.37	457.47	72.26
25.00	54.50	40.06	37.53	23.44	20.00	179.37	2253.48	454.99	75.78
50.00	51.89	28.33	34.19	199.99	21.74	100.43	893.21	514.59	74.61
100.00	81.00	33.00	37.00	254.93	85.29	80.64	350.78	591.40	81.09

4.5.2 Current transfer ratio calculation:

The current transfer ratio between EDL and RP were calculated for the circuit consisting of an EDL (ideal capacitor) and RP (resistor) elements in parallel. First, a sinusoidal voltage *V(t)* was generated at a given frequency using equation A4.2, where V_p is peak to peak voltage, *w* is frequency in radians/s, and *t* is time. The current through the RP element at a given time was then found from equation A4.3, where $I_{RP}(t)$ is current flowing through a resistor at time *t*, and *V(t)* is voltage across the resistor at time *t*, with R_p

being the resistance of the RP element. The current through the EDL was calculated using equation A4.4, where $I_{EDL}(t)$ is the current flowing through the capacitor at time *t*, $V(t)$ is voltage across the capacitor, and *C* is the capacitance of the EDL layer. The capacitance for the EDL layer was calculated using equation A4.5, where *Q* is the charge of a non-ideal CPE element, w_{max} is frequency (rad/s) at which the imaginary impedance maxed out, and *n* is the non-ideal correction value. Finally, the current transfer ratio is found from equation A4.6, where integration is performed over a single voltage oscillation period. The values used for the calculations are shown in table A4.2.

$$V(t) = V_p \sin(w * t) \;\; eq.A4.2$$

$$I_{RP}(t) = \frac{V(t)}{R_p} \;\; eq.A4.3$$

$$I_{EDL}(t) = \frac{w * V_p * C_{EDL} * \cos(w * t) * V(t)}{V_p * \sin(w * t)} \; eq.A4.4$$

$$C = Q(w_{max})^{n-1} \; eq.A4.5$$

$$\frac{RP}{EDL} = \frac{\int_0^t I_{RP}(t)\, dt}{\int_0^t I_{EDL}(t) dt} \; eq.A4.6$$

Table A4.2 | Values used for current transfer ratio calculations (FQ_{max} (Hz) is equivalent to w_{max} (rad/s))

Salt (g/L)	R_P (Ω)	FQ_{max} (Hz)	C_{EDL} (μF)
10.00	3163.4	3.5	194.1
25.00	2253.5	5.0	197.4
50.00	893.2	6.5	200.6
100.00	350.8	9.0	275.8

4.5.3 Titanium Electrode degradation and additional MD data:

Titanium (Ti) electrodes were used in the MD cell to deliver the power to the CNT coated membrane (membrane heating) or directly to the saline solution (solution heating). It was observed that even when operating at 10 kHz the Ti electrodes started to degrade as there was no short circuit available to prevent surface charging. When the Ti electrodes delivered power to the CNT network, no degradation was observed. SEM images revealed that Ti plates operating with CNT structure showed no pitting, which is a clear indication of surface oxidation. (Fig A4.1) However, when no CNT structure was present, the Ti plates showed heavy pitting. Analysis of the pitted Ti surfaces using energy dispersive X-ray spectroscopy found elevated oxygen content, reduced Ti content, and the presence of Cl, all indicating formation of Titanium Oxides and Titanium Chlorides. (Fig. A4.2a,b)

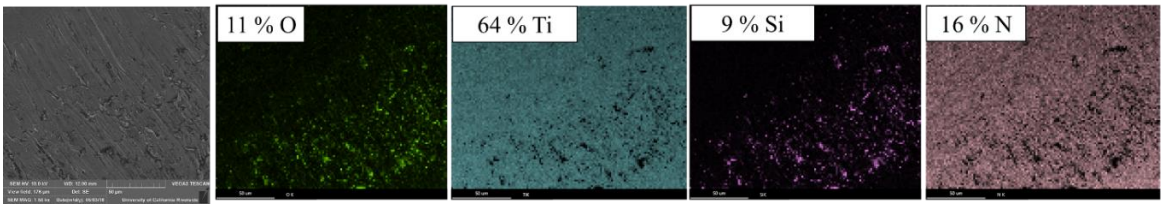

Figure A4.1 | Edge section of the Ti plate that was operated with CNT coated membrane showing no pitting or degradation, and average content of oxygen Ti, Silicon and Nitrogen.

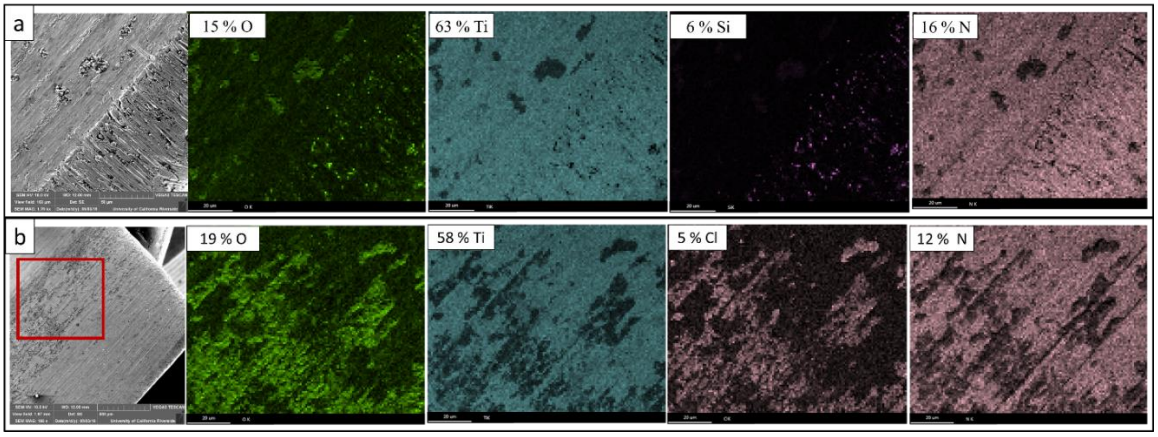

Figure A4.2 | Titanium plates that were operated without CNT coated membrane. a, The SEM and EDS images of the titanium electrode edge showing pitting marks and elevated oxygen content of the pitted areas b, The SEM image of the titanium plate surface with the EDS of inner part of the electrode (Red box shows area on which EDS was performed) showing clear signs of surface pitting, elevated oxygen content, reduction in Ti content and presence of Cl.

4.5.4 Additional MD data:

Membrane distillation experiments were performed at 25 g/L and 100 g/L (100 g/L data in main text). Under both conditions, the application of power to the membrane resulted in a rapid increase in permeate flux and outflow temperatures (Fig. A4.3). Operation with the CNT/PVA heated membranes at 25 g/L resulted in higher permeate fluxes compared to the operation with Ti plates alone, or operating at 100 g/L (Fig. S3). The lower salt concentrations also resulted in higher water recovery rates of 16%, 5.2% and 1.7% at 1.5, 3.3 and 6.6 mm/s cross flows, respectively (Fig. A4.3a). The improved recoveries were due to lower impact of salt on permeate flux (e.g. lower salt concentration resulted in higher water vapor pressures). Similar to results at 100 g/L, the CNT/PVA heated membranes also experienced lower outflow temperatures, compared to Ti heated

system, further indicating that CNT/PVA films are able to deliver more thermal energy to the membrane/vapor forming interface compared to bulk heating with Ti plates (Fig. A4.3b).

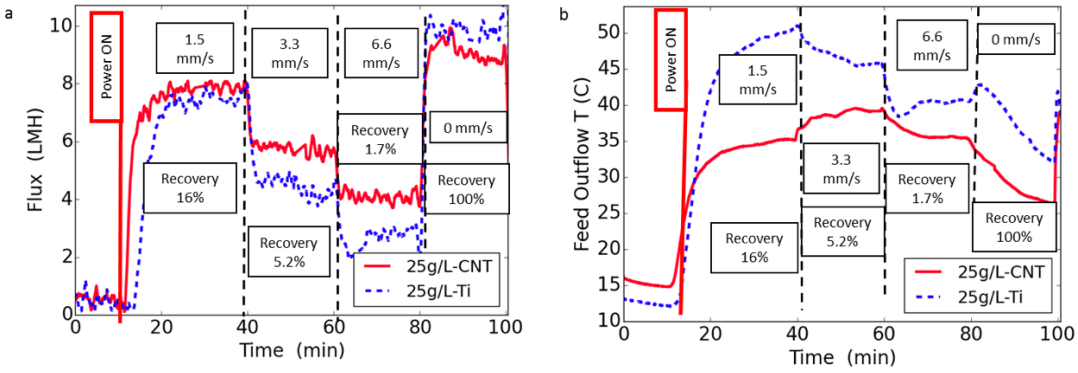

Figure A4.3 | Flux and temperature data for different cross flows operating with feed of 25 g/L NaCl. a, Permeate flux data and single pass recoveries. b, Outflow temperature data.

4.6 References

1. Shannon, M. A. *et al.* Science and technology for water purification in the coming decades. *Nature* **452,** 301–310 (2008).

2. Elimelech, M. & Phillip, W. A. The future of seawater desalination: energy, technology, and the environment. *science* **333,** 712–717 (2011).

3. Fritzmann, C., Löwenberg, J., Wintgens, T. & Melin, T. State-of-the-art of reverse osmosis desalination. *Desalination* **216,** 1–76 (2007).

4. Eykens, L. *et al.* Influence of membrane thickness and process conditions on direct contact membrane distillation at different salinities. *J. Membr. Sci.* **498,** 353–364 (2016).

5. Alkhudhiri, A., Darwish, N. & Hilal, N. Membrane distillation: A comprehensive review. *Desalination* **287,** 2–18 (2012).

6. Mundhenk, N., Huttenloch, P., Kohl, T., Steger, H. & Zorn, R. Metal corrosion in geothermal brine environments of the Upper Rhine graben – Laboratory and on-site studies. *Geothermics* **46,** 14–21 (2013).

7. Jang, H.-S., Jeon, S. K. & Nahm, S. H. The manufacture of a transparent film heater by spinning multi-walled carbon nanotubes. *Carbon* **49,** 111–116 (2011).

8. Janas, D. & Koziol, K. K. Rapid electrothermal response of high-temperature carbon nanotube film heaters. *Carbon* **59,** 457–463 (2013).

9. Wu, Z. P. & Wang, J. N. Preparation of large-area double-walled carbon nanotube films and application as film heater. *Phys. E Low-Dimens. Syst. Nanostructures* **42,** 77–81 (2009).

10. Jung, D., Kim, D., Lee, K. H., Overzet, L. J. & Lee, G. S. Transparent film heaters using multi-walled carbon nanotube sheets. *Sens. Actuators Phys.* **199,** 176–180 (2013).

11. Gupta, R., Rao, K. D. M., Kiruthika, S. & Kulkarni, G. U. Visibly Transparent Heaters. *ACS Appl. Mater. Interfaces* **8,** 12559–12575 (2016).

12. Kang, T. J., Kim, T., Seo, S. M., Park, Y. J. & Kim, Y. H. Thickness-dependent thermal resistance of a transparent glass heater with a single-walled carbon nanotube coating. *Carbon* **49,** 1087–1093 (2011).

13. Jyoti, G., Keshav, A. & Anandkumar, J. Review on Pervaporation: Theory, Membrane Performance, and Application to Intensification of Esterification Reaction. *J. Eng.* **2015,** 1–24 (2015).

14. Ong, Y. K. *et al.* Recent membrane development for pervaporation processes. *Prog. Polym. Sci.* **57,** 1–31 (2016).

15. Saeidi, S., Amin, N. A. S. & Rahimpour, M. R. Hydrogenation of CO2 to value-added products—A review and potential future developments. *J. CO2 Util.* **5,** 66–81 (2014).

16. Jadhav, S. G., Vaidya, P. D., Bhanage, B. M. & Joshi, J. B. Catalytic carbon dioxide hydrogenation to methanol: A review of recent studies. *Chem. Eng. Res. Des.* **92,** 2557–2567 (2014).

17. Honig, R. E. Ionization Potentials of Some Hydrocarbon Series. *J. Chem. Phys.* **16,** 105 (1948).

18. Parker, V. D. Energetics of electrode reactions. II. The relationship between redox potentials, ionization potentials, electron affinities, and solvation energies of aromatic hydrocarbons. *J. Am. Chem. Soc.* **98,** 98–103 (1976).

19. Liu, P., Liu, L., Jiang, K. & Fan, S. Carbon-Nanotube-Film Microheater on a Polyethylene Terephthalate Substrate and Its Application in Thermochromic Displays. *Small* **7,** 732–736 (2011).

20. Zhang, Q., Huang, J.-Q., Qian, W.-Z., Zhang, Y.-Y. & Wei, F. The Road for Nanomaterials Industry: A Review of Carbon Nanotube Production, Post-Treatment, and Bulk Applications for Composites and Energy Storage. *Small* **9,** 1237–1265 (2013).

21. Dudchenko, A. V., Rolf, J., Russell, K., Duan, W. & Jassby, D. Organic fouling inhibition on electrically conducting carbon nanotube–polyvinyl alcohol composite ultrafiltration membranes. *J. Membr. Sci.* **468,** 1–10 (2014).

22. de Lannoy, C., Jassby, D., Davis, D. D. & Wiesner, M. R. A highly electrically conductive polymer–multiwalled carbon nanotube nanocomposite membrane. *J. Membr. Sci.* **415–416,** 718–724 (2012).

23. Duan, W., Ronen, A., Walker, S. & Jassby, D. Polyaniline-Coated Carbon Nanotube Ultrafiltration Membranes: Enhanced Anodic Stability for *In Situ* Cleaning and Electro-Oxidation Processes. *ACS Appl. Mater. Interfaces* (2016). doi:10.1021/acsami.6b07196

24. Liu, H., Vajpayee, A. & Vecitis, C. D. Bismuth-Doped Tin Oxide-Coated Carbon Nanotube Network: Improved Anode Stability and Efficiency for Flow-Through Organic Electrooxidation. *ACS Appl. Mater. Interfaces* **5,** 10054–10066 (2013).

25. Janas, D., Kreft, S. K., Boncel, S. & Koziol, K. K. K. Durability and surface chemistry of horizontally aligned CNT films as electrodes upon electrolysis of acidic aqueous solution. *J. Mater. Sci.* **49,** 7231–7243 (2014).

26. Bagotsky, V. S. *Fundamentals of Electrochemistry*. (John Wiley & Sons, 2005).

27. Weber, B. *et al.* Ohm's Law Survives to the Atomic Scale. *Science* **335,** 64–67 (2012).

28. Verwey, E. & Overbeek, T. *Theory of stabilty of lyophobic colloids*. (Elsievier Publishing Company, 1948).

29. Kilic, M. S., Bazant, M. Z. & Ajdari, A. Steric effects in the dynamics of electrolytes at large applied voltages. II. Modified Poisson-Nernst-Planck equations. *Phys. Rev. E* **75,** (2007).

30. Impedance spectroscopy: theory, experiment, and applications. (Wiley-Interscience, 2005).

31. Ayliffe, H. E., Frazier, A. B. & Rabbitt, R. D. Electric impedance spectroscopy using microchannels with integrated metal electrodes. *J. Microelectromechanical Syst.* **8,** 50–57 (1999).

32. Randles, J. E. B. Kinetics of rapid electrode reactions. *Discuss. Faraday Soc.* **1,** 11–19 (1947).

33. Lin, S., Yip, N. Y. & Elimelech, M. Direct contact membrane distillation with heat recovery: Thermodynamic insights from module scale modeling. *J. Membr. Sci.* **453,** 498–515 (2014).

34. He, F., Gilron, J. & Sirkar, K. K. High water recovery in direct contact membrane distillation using a series of cascades. *Desalination* **323,** 48–54 (2013).

35. Automated Solution of Differential Equations by the Finite Element Method. **84,** (Springer Berlin Heidelberg, 2012).

36. Lackovic, I., Magjarevic, R. & Miklavcic, D. Three-dimensional finite-element analysis of joule heating in electrochemotherapy and in vivo gene electrotransfer. *IEEE Trans. Dielectr. Electr. Insul.* **16,** 1338–1347 (2009).

37. Girault, V. & Raviart, P.-A. Finite element methods for Navier-Stokes equations: theory and algorithms. (Springer, 1986).

38. Sharqawy, M. H., Lienhard, J. H. & Zubair, S. M. Thermophysical properties of seawater: a review of existing correlations and data. *Desalination Water Treat.* **16,** 354–380 (2010).

39. Kochowski, S. & Nitsch, K. Description of the frequency behaviour of metal–SiO2–GaAs structure characteristics by electrical equivalent circuit with constant phase element. *Thin Solid Films* **415,** 133–137 (2002).

Chapter 5 Conclusions

5.1 Summary

The dissertation has presented application of carbon nanotube and nano-magnetite based thin films for improvement of membrane filtration processes. The CNT-PVA thin films were synthesized on variety of membranes including PS, PAN and PTFE. The synthesized CNT-PVA thin films have demonstrated high electrical conductivity, hydrophilicity and underwater super-oleophobic properties which were used to enhance membrane filtration processes. We demonstrated how application of electrical potentials to the membrane surface can generate strong electrostatic forces repulsing charged organic molecules and significantly reducing fouling rates. We then demonstrated that coating of oil droplets with nano-magnetite thin films (i.e. forming Pickering emulsions) made it possible to prevent oil coalescence and membrane fouling. Finally, it was demonstrated that through application of AC potentials across CNT-PVA films deposited on membrane surface it was possible to use them as Joule heaters and drive the MD process.

Herein we revisit the conclusions of the presented work and discuss some of the broader impacts.

5.2 Conclusions

The primary objectives of the presented dissertation were to explore synthesis of nanomaterial based thin films and their applications in membrane filtration processes. The application of CNT-PVA thin films for generation of strong electrostatic forces has been presented, showing improved membrane fouling resistance. It was demonstrating that the nano-magnetite thin films that coated oil-drops formed a physical barrier that prevented oil

coalesces and membrane fouling. Furthermore, it was demonstrated that the CNT-PVA films could be used as joule heaters, generating a thermal driving force in MD process and treating high salinity brines. Following are the primary conclusions that were deduced from experimental and theoretical work presented in each chapter:

Chapter 2 demonstrated that the CNT-PVA thin films could be used to generate strong electrostatic repulsive forces preventing fouling in UF with charged organic molecules. The CNT-PVA thin films were synthesized using the pressure deposition process followed by crosslinking with GA. The crosslinking between PVA and the CNTs was confirmed through ATR-FTIR, which showed reduction in absorption of the COOH and OH peaks indicating formation of covalent bonds. The prepared CNT-PVA films exhibited high electrical conductivity of 2500 S/m in air but immersion in water resulted in conductivity reduction to 1700 S/m. The conductivity reduction was caused by hydration and swelling of the PVA which partially broke the percolating CNT network reducing number of electron pathways through it. The membranes coated with the CNT-PVA films were then used to treat uncharged PEO and charged AA under application of different electrical potentials. The application of potentials reduced fouling rates when treating the charged AA, but had no impact on fouling with uncharged PEO. These results demonstrated that the application of electrical potentials lead to repulsion of charged organic molecules and prevented their interaction with the membrane surface which reduced fouling rates. The observed results were further supported by the solution of MPB equation which showed that strong electrostatic repulsive forces extend close to 5 nm away from the membrane surface and the extension increased with the magnitude of the applied

potentials, qualitatively explaining experimental results. However, both experimental results and solution of MPB equation have demonstrated that the addition of salt reduces the electrostatic forces and their impact on fouling prevention, which can make this process unsuitable of fouling control in high salinity environments.

In Chapter 3 we demonstrated that nano-magnetite could be used to form thin films on the surface of oil droplets (i.e. forming Pickering emulsions) preventing membrane fouling in a highly saline environment, where the electrostatic forces are significantly compromised. The nano-magnetite films were shown to act as physical barriers that prevented the oil drops from interacting with the membrane surface as well as other oil droplets. The prevention of these interactions effectively stopped oil coalescence and membrane oil wetting, which are the two primary oil fouling mechanisms. The experimental results further demonstrated that the membrane and nanoparticle properties played an important role in fouling prevention. The magnetite nanoparticles that had moderate hydrophilicity showed best Pickering emulsions stability, while the CNT-PVA coated membranes which exhibited under water super-oleophobicity demonstrated exceptional antifouling performance. However, the nanoparticles that were very hydrophilic and the membranes that were hydrophobic showed poor fouling resistance. These observations were qualitatively explained by the developed theoretical framework that explored the impact of nanoparticle and membrane hydrophilicity on the critical flux. The theoretical framework showed that nanoparticles that were too hydrophilic did not sufficiently stabilize oil droplets and could be readily removed from the oil surface allowing for coalescence, while hydrophobic membranes were shown to get readily wetted

once the nanoparticle barrier failed. The results from experimental and theoretical frame work demonstrated that Pickering emulsions that were prepared with nano-magnetite could be an effective method at preventing oil coalescence and oil interaction with the membrane surface preventing membrane fouling.

Chapter 4 presented application of the CNT-PVA thin films as Joule heating elements which could be used to drive the MD process. Although the CNT films have previously been used as Joule heaters they have never been demonstrated to function in ionizable environments (e.g. salt water) due to rapid degradation of the CNTs under DC potentials. The EIS studies demonstrated that degradation of the CNT-PVA films could be prevented through frequency control of applied AC potentials. The EIS studies revealed that the CNT degradation rate was a strong function of applied frequency, and a moderate function of salinity. The CNT degradation rate was found to be driven by formation of the EDL layer which forced electron flow through the ionizable solution leading to electrochemical reactions. Application of moderate AC frequencies prevented the formation of the EDL layer and consequently prevented the electrochemical reactions which degraded the CNT structure, with long term studies confirming these findings. This chapter also presented the spray deposition method of preparing the CNT-PVA films on hydrophobic membranes used in MD. The spray deposition method prevented the CNT or PVA penetration into the membrane pores producing a binary membrane structure, where the MD support retained its hydrophobicity while the CNT-PVA exhibited high hydrophilicity. The water/vapor formation occurred at the CNT/membrane interphase allowing these membranes to achieve high salt rejections. Finally, it was demonstrated that

the CNT-PVA films can be directly heated using the Joule heating effect and drive the MD process. The experimental results clearly demonstrated that direct surface heating prevented thermal energy loss to the bulk feed achieving higher permeate fluxes compared to the bulk feed heating. The results further demonstrated that the direct surface heating could be used to achieve high single pass recoveries approaching 100% and far exceeding the theoretical limit of 6.5%.

The work presented in here demonstrated the application of nanomaterial based thin films and their application in enhancement of the membrane filtration processes. The primary focus of the dissertation was on fouling prevention, arguably the biggest challenge in membrane filtration. The presented work clearly demonstrated that by taking advantage of the nanomaterial properties it is possible to effectively and efficiently prevent fouling. The electrical conductivity of CNT-PVA films made it possible to generate very strong artificial electrostatic forces that cannot be achieved with standard membrane modification techniques (such as blending or polymer grafting of charged groups). The generation of the electrostatic forces then allowed us to prevent organic fouling even when operating in waters with high organic loadings. We further took advantage of the nanoparticles with semi hydrophilic/hydrophobic properties which forced them to enter the oil/water interface coating the oil droplets. The nanoparticle coating created a physical barrier that prevented oil coalescence and membrane wetting during filtration. Finally, we presented how the conductive properties of CNT-PVA thin films could be used to generate thermal energy through the Joule heating effect. The CNT degradation was prevented through application of AC potentials with moderate frequencies which prevented surface charging of the CNT

network and limited the number of electrons that could participate in electrochemical reactions. Furthermore, it was demonstrated that direct heating of the CNT-PVA films resulted in lower thermal losses to the bulk fluid which lead to higher permeate fluxes and exceptionally high single pass recoveries. The presented findings have thus demonstrated that nanomaterial based thin films possess unique properties that can be used to drastically improve the membrane filtration processes.

5.3 Broader Impacts

The presented work addressed key challenges facing membrane filtration today and has the potential of greatly increasing the applicability and efficiency of filtration processes. The fouling mitigation that was achieved with electrostatic forces presented in Chapter 2 have great range of application from waste water treatment to drinking water purification. Wastewater recycling is being looked as one of the most promising methods for regions to increase their local water supply. In most wastewater recycling plans secondary or tertiary wastewater is treated by MF or UF and then finally purified by NF or RO coupled to advanced oxidation process producing high purity water. The UF and MF take the brunt of the fouling and the treatment as wastewaters contain large quantities of organics, NOM, EPS, and bacteria which rapidly foul the membranes. The application of electrostatic forces generated on the CNT-PVA films could significantly improve the filtration process reducing the amount of time lost to cleaning and reducing energetic costs by reducing operating pressures. Water recycling is probably one of the most important steps that must be taken to achieve water sustainability as old water sources such as

aquifers, surface water, and ground water are being depleted and are not replenished due dropping precipitation levels caused by global warming. Furthermore, reducing the cost of water treatment must be one of the key aspects of newly developed techniques, as water must be affordable and readily available to all.

The presented application of the nano-magnetite which encapsulated the oil drops and stopped oil fouling during membrane filtration can have large implications for oil spill management, and treatment of produced and flow backwaters. Current oil spill management techniques rely on sorption or dispersion which stop working in cold environments such as the arctic, where large number of drilling operation have begun. We have demonstrated that the nano-magnetite stabilization process still works in 2 ˚C water, which means this process could work in the Arctic. Furthermore, the fact that UF can be used directly with this process could allow for construction of small and compact systems with high throughput allowing direct installation on ships. Since the UF permeate has been shown to contain less than 15 PPM of oil it can be directly returned to the environment allowing for the ships to operate for extended periods of time during clean-up operations. Similarly, the compact size of the proposed oil treatment system would allow for it to be installed on a trailer rigs and be readily moved around oil drill sites, treating produced and flow back waters directly as they leave the well. The treatment onsite would remove the need to store and transport the waste water from the drilling site, and thus remove the key risks associated with oil production making these processes significantly cleaner and safer.

Thermally driven processes are extremely common and are used in processes ranging from simple household water heating to the separation and purification of fuels via

distillation. These processes in general suffer from high energetic costs and complex designs which attempt to optimize energy management to reduce operating costs but lead to high capital costs. The developed CNT Joule heating processes could be used to simplify allot of different thermally driven processes, as they can operate in ionizable environments (e.g. water, hydrocarbons, and air) without degradation. Furthermore, large quantities of thermal energy can be delivered directly to the solution or interface where heating is required such as the surface of MD membranes, chemical reactors, and water heating units (e.g. flow through heating of water). These processes can lead to significant simplification of many thermally driven process making it possible to reduce their operational and capital costs. Furthermore, since this process uses electrical energy it can easily interface with renewable energy sources which produce electrical energy rather than hydrocarbons which are typically burned to generate thermal energy.